



SAPIENZA
UNIVERSITÀ DI ROMA

Wave impact in sloshing flows: hydroelasticity in shallow water condition

Dottorato di Ricerca in Meccanica Teorica ed Applicata – XXVIII Ciclo

Candidate

Andrea Bardazzi
ID number 795187

Thesis Advisor

Prof. Giorgio Graziani

Co-Advisor

Dr. Claudio Lugni

A thesis submitted in partial fulfillment of the requirements
for the degree of Doctor of Philosophy in Engineering

September 26th 2017

Thesis defended on 26 September 2017
in front of a Board of Examiners composed by:
Prof. F. Marulo (chairman)
Prof. A. Mazzino
Prof. A. Crivellini

Wave impact in sloshing flows: hydroelasticity in shallow water condition
Ph.D. thesis. Sapienza – University of Rome

This thesis has been typeset by \LaTeX and the Sapthesis class.

Author's email: andrea.bardazzi@insean.cnr.it

*Dedicated to
Donald Knuth*

Ringraziamenti

Vorrei ringraziare il Dott. Claudio Lugni ed il Prof. Giorgio Graziani che mi hanno supportato (e sopportato) durante tutto questo avvincente percorso.

Contents

1	Introduction	1
1.1	Objective and outline of the thesis	4
2	Experimental Investigation	5
2.1	Experimental Set-Up	6
2.1.1	Scaling of the problem	7
2.1.2	Dynamic characterization of the structure	9
2.2	Wave scenarios	13
2.2.1	Case A) Flip-through	14
2.2.2	Case B) Gas cavity	17
2.3	Discussion of the results	20
2.3.1	Flip-through impact	20
2.3.2	Impact with gas cavity	24
3	Mathematical Model	37
3.1	Physical assumptions for the hydroelastic problem	38
3.2	Mathematical Model for the sloshing stage	40
3.3	Mathematical model for the hydroelastic stage	44
3.3.1	“Lumped” model for the gas-cavity	46
3.3.2	Structural sub-problem	46
3.4	Hybrid hydroelastic model	48
3.4.1	Gas cavity analytical model	53
3.4.2	Gas cavity hydroelastic model	64
4	Numerical Model	77
4.1	Sloshing Stage	78
4.1.1	Potential flow solver	78
4.1.2	Time integration procedure	82
4.1.3	Test cases	83
4.2	Fully hydroelastic model	91
4.2.1	semiAnalytic Flip-Through	92
5	Conclusions	99
5.1	Suggestions for future activities	100
	Appendix A Generalized HPC method for the Poisson equation	103

List of Figures

2.1	View of the sloshing tank. The red ellipse highlights the stainless steel wall holding the deformable plate, indicated by the white arrow.	6
2.2	Top right: Snapshot of the Mark III tank. Top left: Schematic drawing representing the tank components. Bottom: View in vertical section of a single panel.	8
2.3	Top panel: comparison of the temporal evolution of acceleration during hammer test. The blue line and the dashed red line represent the acceleration measured by strain gauges and accelerometer respectively. Bottom panel: Comparison of acceleration FFT in term of amplitude and phase.	11
2.4	Comparison of the beam lowest natural frequency in wet hammer test as function of the filling depth. The green markers show the behaviour of the first natural bending frequency of the structure while the continuous line correspond to the values predicted by the hydroelastic model.	12
2.5	Behaviour of the dimensionless values of the structural experimental damping coefficient relative to the lowest structural mode (symbols). The solid line represents the cubic functions which fits the symbols. The dashed line reports the values of the structural damping in dry conditions.	12
2.6	Interaction of a nearly breaking wave with a vertical wall. The dash lines show the wave temporal evolution in the absence of the wall, while the continuous lines represent the evolution of the same wave interacting with the wall.	13
2.7	Numerical temporal evolution of the wave profile in case of flip-through impact (see [30]).	14
2.8	Each panel shows the time history of the pressure transducer along the rigid vertical wall. Their vertical position ($y=0$ corresponds to the tank bottom) is indicated on the panel. The red line represents the mean value calculated with 5 repetitions of the same run, the error bar identifies the relative standard deviation. The black line shows the pressure value measured during a single test, fig. (2.9), where the frames shown refer to time instants labelled A, B, C, D, and E.	16
2.9	Evolution of the flip-through impact at five different times. The green diamonds indicate the pressure transducers position. The red line represents the interpolation of the pressure data recorded (red circles).	17

2.10	In the five snapshots the kinematic evolution and the hydrodynamic pressure profile along the vertical wall are reported. The red dots show the instantaneous values of the pressure recorded during the experiment by the pressure transducers highlighted by the green diamonds. In the plot the pressure time histories are shown. The blue and the red lines represent the signals of sensors 5 and 2, respectively. The five dashed black vertical lines identify the snapshots time instants.	19
2.11	Dynamic temporal evolution of the flip-through impact against an elastic structure. The three upper panels show the dimensionless stresses recorded by the three central gauges. In the lower panel the hydrodynamic pressure measured close the tank bottom is shown. The black arrows in the upper panel identify the <i>stages</i> of hydroelastic impact.	21
2.12	Top panel: Time history of the dimensionless stress measured in the middle of the beam and the first three IMF estimated with the EMD. Bottom panel: Time history of the instantaneous frequencies, which characterize the three IMF reported. The dashed and continuous black line show the theoretical variation of the first two wet natural frequencies of the beam, respectively.	22
2.13	<i>Large</i> size Cavity. The six snapshots shows the wave front configuration just before the impact against the elastic vertical wall for different ullage pressures. In each snapshot, the time evolution of the recorded structural stress is reported. The circle before the first peak show the snapshot position in the stress time history.	27
2.14	<i>Medium</i> size Cavity. The six snapshots shows the wave front configuration just before the impact against the elastic vertical wall for different ullage pressures. In each snapshot, the time evolution of the recorded structural stress is reported. The circle before the first peak show the snapshot position in the stress time history.	28
2.15	<i>Small</i> size Cavity. The six snapshots shows the wave front configuration just before the impact against the elastic vertical wall for different ullage pressures. In each snapshot, the time evolution of the recorded structural stress is reported. The circle before the first peak show the snapshot position in the stress time history.	29
2.16	<i>Large</i> size Cavity. Time evolution of the mean normalized stress measured in the middle of the structure.	30
2.17	<i>Medium</i> size Cavity. Time evolution of the mean normalized stress measured in the middle of the structure.	31
2.18	<i>Small</i> size Cavity. Time evolution of the mean normalized stress measured in the middle of the structure.	32
2.19	Lowest natural frequency of the gas cavity as function of the ullage pressure for rigid (blue line) and elastic test (red line) for the three different cavity sizes.	33
2.20	Damping ratio (top plot) and exponential decay (bottom plot) for the different cavity size impact as function of the ullage pressure.	34
2.21	Comparison between the original signal (blue dashed line) and the de-trended one (red continuous line), which has been used for the estimation of the exponential decay.	35
2.22	Exponential fitting and damping stages for the elastic case.	35

2.23 (Left column): Values of the minimum pressure recorded during the experimental test for the three cavities as function of the cavitation number (log scale), ullage pressure from 50 to 1000 mbar. (Right column): Maximum values of the structural stress (top) and hydrodynamic pressure (bottom) as function of the cavitation number.	36
3.1 Tank model	41
3.2 Variation of the first (blue) and second (green) wet natural frequency as function of the filling depth. Symbols are obtained from the HOBEM, while lines come from the Fourier Transform method.	50
3.3 Elastic test. Comparison between the numerical prediction (purple line) and experiment (black line). If present the dashed green line shows the instantaneous wave elevation at wall. In the top-left panel, no damping term is used in the model. In the bottom-left panel a constant structural damping is added to the model. On the top-right panel, a time varying damping coefficient is used. In the bottom-right panel, the time history of the wave height has been restricted until to 0.22 cm.	52
3.4 Sketch of the proposed mathematical model for the gas cavity problem. \overline{AA}_∞ free surface, \overline{AD} tank vertical wall, \overline{DD}_∞ tank bottom, \overline{BC} cavity size. The boundary conditions and the governing equation are also reported. . .	54
3.5 In the half plane $\eta > 0$ we have the transformed boundary conditions for the free oscillation problem. For $\eta < 0$ we find the boundary conditions for the forced problem.	55
3.6 Non dimensional natural frequencies of the cavity as function of the initial cavity radius at different position of the cavity center(y_b).	57
3.7 Comparison of the velocity potential along the vertical wall calculated with the proposed analytical model and with the Topliss model. The center of the cavity is at $y_b/h = 0.5455$	58
3.8 Non dimensional natural frequencies (blue dots) compared with the ones from Topliss analytical model (black circles).	60
3.9 <i>Medium</i> cavity size at 1000 mbar, $r_0=.0052$ m, $d=.1729$ m, $h=.1910$ m, Non-Linear model 320 Hz, Linear model 319.61 Hz, Topliss model 366.89 Hz, experimental ≈ 320 Hz.	61
3.10 <i>Medium</i> cavity size at 400 mbar, $r_0=.0051$ m, $d=.1719$ m, $h=.1873$ m, Non-Linear model 200 Hz, Linear model 213.56 Hz, Topliss model 246.40 Hz, experimental ≈ 185 Hz.	61
3.11 <i>Medium</i> cavity size at 100 mbar, $r_0=.0045$ m, $d=.1709$ m, $h=.1887$ m, Non-Linear model 100 Hz, Linear model 114.32 Hz, Topliss model 130.63 Hz, experimental ≈ 90 Hz.	62
3.12 <i>Small</i> cavity size at 1000 mbar, $r_0=.0073$ m, $d=.1694$ m, $h=.1899$ m, Non-Linear model 240 Hz, Linear model 239.2 Hz, Topliss model 276.95 Hz, experimental ≈ 233 Hz.	62
3.13 <i>Small</i> cavity size at 400 mbar, $r_0=.0103$ m, $d=.1722$ m, $h=.1918$ m, Non-Linear model 118 Hz, Linear model 120.14 Hz, Topliss model 141.72 Hz, experimental ≈ 120 Hz.	63

- 3.14 *Small* cavity size at 100 mbar, $r_0=.012$ m, $d=.1679$ m, $h=.1890$ m, Non-Linear model 50 Hz, Linear model 52.9 Hz, Topliss model 62.68 Hz, experimental $\approx 50/55$ Hz. 63
- 3.15 Top sketch: representation of the physical problem with boundary conditions and governing equation. \overline{AA}_∞ free surface, \overline{EE}_∞ tank bottom, \overline{AE} tank vertical wall, \overline{BC} gas cavity and D lower extrema of the elastic beam. Bottom sketch: geometry and the boundary conditions are reported in the transformed plane (ξ, η) 64
- 3.16 First wet natural frequency as function of the filling depth. Comparison of the results obtained by solving the fluid problem with a HOBEM method (blue markers) and using the vortex distribution along the vertical wall. . . . 66
- 3.17 Behaviour of the eigenvalues of the linearized dynamic system as function of the cavity radius (red and blue dots). The circle show the eigenvalues trends in the case of uncoupled problem. 67
- 3.18 Comparison between the experiment and the analytical model in terms of impact scenario with gas-cavity. The colored lines of the model are explained in the main text. 68
- 3.19 Comparison between experiments and analytical model of impact with gas cavity: *Medium* size cavity - 1000 mbar. Top plot: structural stresses evaluated in the middle of the structure. Center plot: Fast Fourier Transform of stress signals. Bottom plot: hydrodynamic pressure for the two pressure transducers located close to the tank bottom. Parameters used in the analytical model: $h = 0.19765$ m, $y_{r0} = .17215$ m, $r_0 = .00463$ m, $\Omega_0=3.36E-5$ m², $V_{max} = 2$ m/s, $T_a=3.0E-4$ s, $\mu = 200$ 69
- 3.20 Comparison between experiments and analytical model of impact with gas cavity: *Medium* size cavity - 400 mbar. Top plot: structural stresses evaluated in the middle of the structure. Center plot: Fast Fourier Transform of stress signals. Bottom plot: hydrodynamic pressure for the two pressure transducers located close to the tank bottom. Parameters used in the analytical model: $h = .19507$ m, $y_{r0} = .17086$ m, $r_0 = .00376$ m, $\Omega_0=2.207-5$ m², $V_{max} = 2$ m/s, $T_a=4.6E-4$ s, $\mu = 100$ 70
- 3.21 Comparison between experiments and analytical model of impact with gas cavity: *Medium* size cavity - 100 mbar. Top plot: structural stresses evaluated in the middle of the structure. Center plot: Fast Fourier Transform of stress signals. Bottom plot: hydrodynamic pressure for the two pressure transducers located close to the tank bottom. Parameters used in the analytical model: $h = .19559$ m, $y_{r0} = .17260$ m, $r_0 = .00495$ m, $\Omega_0=3.30E-5$ m², $V_{max} = 2$ m/s, $T_a=6.2E-4$ s, $\mu = 60$ 71
- 3.22 Comparison between experiments and analytical model of impact with gas cavity: *Large* size cavity - 1000 mbar. Top plot: structural stresses evaluated in the middle of the structure. Center plot: Fast Fourier Transform of stress signals. Bottom plot: hydrodynamic pressure for the two pressure transducers located close to the tank bottom. Parameters used in the analytical model: $h = .19610$ m, $y_{r0} = .17240$ m, $r_0 = .00734$ m, $\Omega_0=8.46E-5$ m², $V_{max} = 2$ m/s, $T_a=8.0E-4$ s, $\mu = 60$ 72

- 3.23 Comparison between experiments and analytical model of impact with gas cavity: *Large* size cavity - 400 mbar. Top plot: structural stresses evaluated in the middle of the structure. Center plot: Fast Fourier Transform of stress signals. Bottom plot: hydrodynamic pressure for the two pressure transducers located close to the tank bottom. Parameters used in the analytical model: $h = .19765$ m, $y_{r0} = .16306$ m, $r_0 = .00867$ m, $\Omega_0 = 1.18E-4$ m², $V_{max} = 2$ m/s, $T_a = 9.0E-4$ s, $\mu = 60$ 73
- 3.24 Comparison between experiments and analytical model of impact with gas cavity: *Large* size cavity - 100 mbar. Top plot: structural stresses evaluated in the middle of the structure. Center plot: Fast Fourier Transform of stress signals. Bottom plot: hydrodynamic pressure for the two pressure transducers located close to the tank bottom. Parameters used in the analytical model: $h = .19817$ m, $y_{r0} = .16573$ m, $r_0 = .00695$ m, $\Omega_0 = 7.59E-5$ m², $V_{max} = 2$ m/s, $T_a = 1.3E-3$ s, $\mu = 60$ 74
- 3.25 Comparison between the exponential decay as function of ullage pressure, for rigid and elastic test, marked with dashed and continuous lines respectively. The different colors refer to the three different cavity sizes: blue for large, red for medium and green for small cavity. 75
- 4.1 Domain discretization. 78
- 4.2 Double overlapping meshes. The blue one is the fixed background mesh, while the magenta is a moving mesh, anchored to the free-surface (red dots). 81
- 4.3 Details of the grid overlapping. The black normal vector to the free-surface shows how the moving grid (magenta) has been built. The red dots identify the free-surface nodes, while the black and green circles, named a and b , are an example of connection nodes for the background and free-surface grid, respectively. 82
- 4.4 Boundary value problem for a linear wave solved in a rectangular domain. Convergence analysis of the error in norm L_2 in logarithmic scale. The continuous lines show the error behaviour for two waves with different kh . The dot-dashed line represents the theoretical trend dx^4 84
- 4.5 Boundary value problem for a linear wave solved within a stencil. L_2 error behaviour for velocity potential and derivatives as function of stretching parameter α (right column). Stencil spatial configuration with different parameter α (left column). 85
- 4.6 Initial boundary value problem for a periodic Fenton wave. Left plot: ratio between the L_2 norm error for velocity potential (dashed line) and free surface elevation (continuous line) for two different discretizations with different time steps. Right plot: temporal evolution for the mass of the system. 86
- 4.7 Initial boundary value problem for a periodic Fenton wave. Left plot: ratio between the L_2 norm error for velocity potential (dashed line) and free surface elevation (continuous line) for two different discretizations with different time steps. Right plot: temporal evolution for the mass of the system. 87

4.8	Wave-maker problem. Wave elevation comparisons for different wave probes between experiment (black marker), BEM (blue line) and HPC (dashed red line).	89
4.9	Wave-maker problem. Magnification of the plunging breaker formation area. The free-surface grid (magenta) and the background grid (blue) configurations are shown. The vectors represent the free-surface nodes velocities.	90
4.10	Comparison of deflection for a beam under hydrostatic pressure. The blue line represents the dynamic solution using the Euler beam model. For the green one always the Euler beam model has been used but a ramp function on gravitational acceleration g to avoid the impulsive start of the problem. The black line represents the solution for the static problem. The magenta line represents the solution for the fully-hydroelastic problem.	93
4.11	Vertical distributions of the impact horizontal velocity in the three considered cases. The values are made dimensionless with the maximum horizontal velocity. The beam is located between 0.125 m to 0.215 m. In the bottom left black box an enlarged view of the velocity profiles is reported.	94
4.12	Comparison of the strain gauges evaluated in the middle of the structure. The colours identify the different vertical velocity profile. (blue - constant, red - triangular, green - parabolic, dashed black line experiment)	95
4.13	Left axis: temporal evolution for the water depth. Right axis: temporal evolution for impact acceleration.	96
4.14	Comparison of hydrodynamic pressure for a probe located at 0.025 m from the tank bottom. Blue line s_1 constant spatial velocity profile, red line s_2 triangular spatial velocity profile, green line s_3 parabolic spatial velocity profile and dashed black line experimental results.	97

List of Tables

- 2.1 Comparison of the first two natural bending frequencies from experiments and from analytical and numerical analyses. 10
- 3.1 Comparison of the natural oscillation frequency of a gas cavity during a wave impact. In the first two columns the distance of the cavity center from the bottom of the tank and from the free surface are indicated respectively, in the third column the cavity radius is indicated while in the last three columns the natural frequency estimated from the experiment, from the Topliss analytical model and from the proposed model are reported. 59
- 4.1 Two-dimensional harmonic polynomials with corresponding order n 79

Chapter 1

Introduction

The impact of waves against marine structures is a common phenomenon in many engineering problems and its consequences must be carefully taken into account for a safe and reliable design of the structure. Offshore structures, as wind farms and oil/gas platforms, or advancing ship, in rough sea are the typical exterior hydrodynamic problems where the structure is exposed to violent interaction with incident wave; other practical examples are coastal structures used to protect the coastline and port when they are reached by steep waves. However, impact phenomena are of concerns also for some interior hydrodynamic problems as the sloshing flows in on-board tanks of the ship carriers for liquefied natural gas (LNG) transportation. This application is expected to expand in the near future, as a consequence of the growing request of *green* energy and for the greater demand of natural gas from the emerging nations, e.g. the People's Republic of China.

According to the latest estimation of the International Energy Agency, a gas consumption growth of 1.6% per year will lead the natural gas to become the second largest source of energy by 2040, after oil and before coal. The increasing number of importing and exporting nation along with the fact that the former are often far from the production area, makes the transportation a crucial point.

The possible ways to distribute natural gas all around the world are through pipelines and carrier ships. Although pipelines will remain the more diffused modality, and with the lowest capital investment, to supply large volume of gas over short to medium distance the LNG ship transportation is the most promising for the future. The trading flexibility, the ability to reach countries far from the extraction area and the reduced risk connected with geopolitical tensions (the recent crisis between Ukraine and Russia is an example of scenario which may undermine the pipeline supply option) are only some motivations to prefer the LNG ship transportation over pipelines.

The ship carriage had a quick development in the last decades, and this brought to modify the volume and the shape of the tank installed on the ship. The Moss type, characterized by a spherical shape, was largely employed up to the end of 1990s. Currently, the Membrane-type tank, with a prismatic shape and larger volume, is the most used. At the end of 2014 the existing fleet of containment system was composed for a 75% of Membrane-type and a 25% of Moss-type tank. The main advantage of a spherical tank is the easier assembly procedure between hull and tank as well as the minimization of the sloshing loads. However, the wastefulness of hull space usage, which implies higher tonnage canal fee, and the ship height, which may cause some restrictions in the route of the ship (e.g. to pass under a

bridge) are only some motivations to prefer prismatic tanks.

The shape of the tank is an important parameter which influences the fluid motion in sloshing phenomena and the related local and global loads on the structure. The resonant nature of sloshing flows implies violent response of the fluid when the tank motion is forced with a period close to the highest sloshing natural period of the tank. In such a condition, violent interface flow phenomena, as overturning waves, slamming, gas cushioning and turbulent wake may occur inside the tank, possibly causing large local and global loads. A spherical tank is the most suitable to reduce sloshing loads on the structure. Because of the tank geometry, the energy associated to the external acceleration is converted in a rotational motion of the fluid. Conversely, in a wall sided rectangular prismatic tank, the risk for large hydrodynamic loads strongly increases.

To prevent as much as possible extreme impact loads on the tank vertical walls, filling depths between the 10% and 70% of tank height are barred during transit. At these two limits, shallow and deep water sloshing phenomena characterize the fluid flow inside the Membrane-type LNG tank. The tank breath B_t is an important parameter in the excitation of the sloshing flow by the sway, roll and yaw motions of the ship, and a qualitative evaluation of the possible scenarios which may occur can be done considering a model scaled sloshing problem in a rectangular tank where B_t is replaced by the tank length L .

In case of intermediate and high filling depth ($h/L > 0.25$), the sloshing phenomena are mainly characterized by a more or less non linear standing wave system, where the maximum wave height is recorded at the tank wall and the resulting wave impacts occur at the roof. As described in [11], for a rectangular tank, three are the different scenarios which may happen in these conditions. When the free-surface is characterized by an elevated curvature near the wall, a thin fast jet arises close to the vertical wall hitting the roof, with the result of a hydrodynamic load extremely concentrated in time and space. When the free-surface curvature is small, a flat impact occurs and an high local pressure is recorded always on the roof. The last case, which produces an impact with the entrainment of a gas cavity and an oscillatory pressure load, is when the free-surface curves down towards the side wall just before hitting the tank roof.

In case of low filling depth ($h/L < 0.15$), the scenario which characterizes the sloshing flow is more complex and marked out by a strong non-linear behaviour. A typical phenomenon which appears inside a tank when excited by a load close to its natural frequency is the hydraulic jump or travelling bore. The jump on the free surface travels inside the tank with a high speed and the impact against the structure is characterized by high pressure load. Verhagen and van Wijngaarden [35] studied the presence of a hydraulic jump when the tank is subjected to roll motion in shallow water condition. They modified the “shallow-water theory”, which fails when the excitation frequency approaches to a resonance frequency ($\omega \rightarrow \omega_r$), to capture the appearance of the hydraulic jump as observed experimentally when $\omega \approx \omega_r$. They conclude that a jump exists only for frequencies in the parabolic range of $(\omega - \omega_r)^2 < 24g\delta/B$ where δ is the oscillation amplitude and B the tank breadth. When the forcing frequency is far from the resonance frequency different scenarios may happen. Olsen & Johnsen in their technical report [28] studied the validity of nonlinear sloshing theories for both shallow and nonshallow water conditions under sway and roll motions. The behaviour of wave elevation, hydrodynamic lateral forces and moments were investigated as function of amplitude and frequencies of the excitation signals. For a given roll motion they highlighted five possible wave scenarios which can be found in a sloshing tank for shallow water condition, classified following an increasing excitation frequency.

Starting from a standing wave system, which occurs for a frequency lower and far from the first natural frequency, the scenario moves towards a set of travelling waves, continuing to a bore which travels, initially, from the tank mid section and subsequently, from one side of the tank to the opposite. Increasing further the frequency, the bore becomes a solitary wave as also in [35]. Bouscasse *et al.* [5] performed a similar study where only the sway motion has been considered. The results of their experimental and numerical activities retrace the classification proposed by Olsen with the addition of a newer wave system ($\omega/\omega_r = 2.31$) characterized by two wave system, which develop inside the tank with a strong nonlinear mutual interaction, which makes the resulting wave system asymmetric. With the exception of the first wave system, characterized by standing wave, in the other ones, breaking waves in the middle of the tank, moving towards the lateral walls with the possible entrainment of gas cavities or even incipient breaking waves hitting the side walls, may occur. All incipient breaking waves hitting the side walls, can be source of stresses for the tank structures as the pumping tower or the single corrugated panels of which is made up. The most dangerous impacts loads are those characterized by a high pressure with a short duration on a limited structural area.

A first issue related to sloshing is a global effect: large hydrodynamic loads may compromise the stability of the vessel and increase the bending moment and shear forces acting on the hull as well as the fatigue loads as described by Zhao *et al.* in [36], which report an increase of the bending moment between 30% and 150% for large LNG carriers. Moreover, the bow slamming is found to be the most important in head seas at high speed, while the stern slamming becomes more significant in following seas at low speed. Graczyk in his PhD thesis [13] investigates the loads and the resulting effects due to sloshing in LNG membrane tanks. He focuses on ship motion in waves, demonstrating that the sea environment influences the long-term sloshing response increasing its severity (harshness). The fluid motion and pressure induced in a tank as well as the structural response and the assessment of the structural capacity have been also investigated, highlighting as a three-parameter Weibull model is adequate method to describe the magnitude of sloshing pressure. With regard to the structural response, both modal analysis and time-domain direct integration scheme have been employed, concluding that the complexity of the structure, which will be detailed in Chap. 2, as the hydrodynamic forcing term makes a simplified method of analysis not suitable for an accurate description of the problem. In the static case, the structural response is composed mainly by a form governed by the steel plate deflection together with the insulation and by a vertical compression of the foam. In the dynamic case, the response is characterized by a multi-modal composition, including the modes representing the both form. The difference in the oscillation frequency and in the phase between the modes of steel plate and plywood increases the complexity of the structural analysis. The influence of hull elasticity and nonlinear effects is crucial for the real assessment of structural stresses. Such effects may increase the bending moment up to 60%, the hogging moment up to a 20% and the vertical acceleration of a 20%.

Kim and Lee [17] reported a strong influence of the service route on the fatigue life of structural elements. Lindemark *et al.* in [20] highlighted the inner knuckles as the most critical areas with respect to fatigue stress, as consequence of high loads concentration.

Additional issues are the local effects concerning the component of the membrane tank. In [7] experiments on drop test in cryogenic conditions and “low cycle” fatigue tests are conducted. In [18] a numerical and experimental study on the strength of a containment system is presented. In [29] a wide range of tests is presented: ultimate static capacity

and “low cycle” fatigue for Mark III, while shear, bending, buckling and indentation for the No.96 plywood plates. The aim of all the tests is the identification of possible failure mechanisms, whose knowledge is fundamental, for assessing the strength of a structure and formulate failure criteria. In [19] the ultimate strength under static and dynamic loading is studied experimentally by dry drop test, measuring the local acceleration of the structure and the impact forces. Fatigue cracks above the bottom plywood near the mastic support strips have been highlighted, together with mastic failures by the mastic softening, separations between the bottom plywood and the PUF and also the separations between the PUF on the triplex.

An additional aspect, in the context of the local effects, which is associated to pressure loads confined both in space and time on small scales, is the possible hydroelastic interaction, which can further increase the structural stresses [22]. These effects may be triggered when the characteristic time scales of the pressure load, as the rise time (for the first pressure peak) or the typical oscillation frequency when a gas cavity is involved in the impact, are comparable with the a natural period of the structure (typically the highest one).

1.1 Objective and outline of the thesis

A complete and accurate analysis of the structural response of a LNG membrane tank, for the assessment of the structural stresses, is a challenge both from the experimental and numerical point of view. The huge dimensions of the tank and the cryogenic liquid contained make a full scale experiment impossible to be realized. At the same time, the installation of measuring instruments in the tank during its operative service is still complicated and not all of the desired measurements can be done. Also the scaling of the prototype model is not free from difficulties. Satisfying simultaneously the fluid dynamics and structural similarities, especially when gas cavities are present, leads to solutions which are hard to realize or manage. The numerical approach does not present minor difficulties. A complete analysis, that takes into account also the hydroelastic effects requires coupling of the hydrodynamic and the structural problems. The computational cost can be extremely high and the goodness of the results has not to be taken for granted. The study of an idealized problem, including only few aspects of the real problem, can be a useful step forward to understand the physical behaviour and for identifying a suitable simplified model.

The main objective of this work is to analyze the effects of wave impact on a deformable structure, emphasizing the possible role of the hydroelastic interaction, with consequence on the structural stresses. Experiments, (semi)analytical and numerical models are used to get a deeper knowledge of the physical effects governing the hydroelasticity induced by slamming events. The additional knowledges will give new insights for the design of both LNG tanks and of similar structures exposed to such phenomena.

Chapter 2 reports the experimental set-up and the results of the physical investigation. Chapter 3 describes the global mathematical problem, composed by sloshing and hydroelastic stages. In particular, for the hydroelastic stage, two analytical models have been developed for the two wave impact typologies considered (i.e. with and without air-cavity entrainment) considered, and compared with the experimental results. In chapter 4, a hydroelastic numerical model is described: a numerical potential flow solver and a multi-grid approach for the free-surface treatment is proposed for the sloshing stage, validated and coupled with a simplified beam model for the structure. Conclusions and suggestions for

future activities are given in Chapter 5.

Chapter 2

Experimental Investigation

The experimental activity, performed at the CNR-INSEAN Sloshing laboratory, is the last of a series of physical investigations [23], [24], [25] about the kinematic and dynamic evolution of several modalities of wave impact in a rectangular sloshing tank with a filling depth ($h/L \approx 0.12$) corresponding to the upper limit of shallow water condition. The dimensions of the tank were chosen so to reproduce two-dimensional (2D) flow conditions. In the previous activities, wave impacts against rigid wall were considered; hydrodynamic pressure distribution along it has been measured as indicator of the local load during impact phenomena. Because of the random behavior which characterizes the local flow of a blunt wave impact, any attempt to identify a limiting maximum pressure correlated with the inflow wave condition was unsuccessful. With the aim to identify a critical load to be used at the design stage, here the focus is given on the hydroelastic response of the structure during the interaction with a breaking wave. It is still used a rectangular tank with 2D flow conditions.

This paves the way to new research goals aiming at reaching the physical comprehension of the main phenomena involved during the wave-wall hydroelastic interaction as well as on the identification of possible scaling laws governing the maximum local hydroelastic load.

The chapter is divided as follow: the experimental set-up is, first, accurately described, showing the sloshing tank characteristics, the scaling procedure applied and the dynamic features of the elastic structure. Next, the physical discussion of the different typologies of wave impacts follows: their kinematic and dynamic evolution for impact against rigid wall, and against deformable wall is investigated highlighting the main differences observed between the rigid and elastic case. For the impact with the entrainment of a gas cavity, the influence of the ullage pressure (i.e. ambient pressure inside the tank) is also systematically examined.

2.1 Experimental Set-Up

In order to reproduce a two-dimensional flow, a narrow tank is employed. It is almost the same tank used in [24] [25] for the experiments on the wave impact against rigid wall. The main dimensions, length, height and width are respectively, $L = 1\text{ m}$, $H = 1\text{ m}$ and $W = 0.1\text{ m}$. It is made of thick plexiglass plates (thickness = 50 mm), reinforced with aluminium and steel structure, which prevents the deformation of the tank during the depressurized tests (fig. 2.1).

Compared to the experimental tests with rigid side walls [24] [25], the plexiglass left lateral wall has been replaced with a stainless steel plate, with a thickness of 40 mm to ensure a rigid structure, suitably milled to hold a deformable aluminium plate. The last one is constrained to the rigid steel wall with an ad-hoc mechanical system, designed to ensure clamped conditions at the top and bottom ends of the plate (hereafter indicated as vertical ends), and keeping free to move the lateral boundaries. In this way, the plate per unit width behaves as a vertical beam. The total length of the plate is 110 mm but two bulges, each one 10 mm long located at the vertical ends, are used for the clamping system. So the real length l of the structure is 90 mm. Along the vertical centre line of the flexible plate, five strain gauges HBM XY11 - 3/350 have been installed. They are located at 12, 28, 45, 62, 78 mm from the lowest end of the plate. Only the bending displacement of the plate along its vertical centre line is measured, as a consequence of the assumption that the plate behaves as a beam. This is consistent with the hydrodynamic assumption of a 2D sloshing flow and with the constraint system considered in the present study.



Figure 2.1. View of the sloshing tank. The red ellipse highlights the stainless steel wall holding the deformable plate, indicated by the white arrow.

The previous experiments on rigid wall [24] [25] showed that the impact phenomena occur at a height of 170-180 mm from the bottom of the tank. Then the instrumented plate is placed with the lower end at 130 mm from the tank bottom, in order to reproduce the same impact event realized in [24] [25] at the middle of the plate. The filling depth h is such that $h/L = 0.125$.

With the aim of evaluating either the hydroelastic loads induced by different impact scenarios and the difference with respect to the rigid wall case, a thicker plate with the same dimensions of the deformable one has been designed. Its thickness of 20 mm ensures a rigid behavior. In this case, five pressure transducers have been installed in the same position of the strain gauges.

Two additional pressure transducers have been placed on the steel wall respectively at 35 and 50 mm from the bottom of the tank. These were useful for the comparison of the hydrodynamic pressure between the deformable and the rigid case. An absolute pressure transducer located on the roof of the tank measured the ullage pressure.

The sloshing tank is mounted above an hexapod which provides the motion. The high accuracy of the system ensures a good repeatability of the forced motion. However, an accelerometer and a wired-potentiometer were used to cross-check the motion parameters. For all the wave impact scenarios considered, a pure sinusoidal sway motion was used: amplitude and period of the motion define the impact modality.

To observe the local kinematic evolution of the wave impact, a high speed camera with a frame rate of 5000 fps and a resolution of 1024×1024 pixels was employed. It provides an accurate description of the flow features both in time and space (7.8 pixels/mm). The global view of the sloshing flow was recorded by two digital cameras, with a frame rate of 100 fps. A trigger signal was used to synchronize the measurements of the transducers with the images of the flow.

2.1.1 Scaling of the problem

A typical approach for scaling sloshing flows is based on the Froude similarity ($Fr = U/\sqrt{gL}$), with U and L , respectively the characteristic speed and length of the problem and g the gravity acceleration, which implies a geometrical scaling between the model and the prototype. In this work, the Froude similarity has been applied also for the scaling of the elastic properties of the structure:

$$\sigma_m = \sigma_p(\Lambda_L)^{1/2} \quad (2.1)$$

where σ is the frequency, the subscripts m and p indicate, respectively, the model and the prototype scale and $\Lambda_L = L_p/L_m$ is the geometrical scale factor.

The top right image of fig. 2.2 shows the interior volume of a Mark III containment system, whose typical dimensions are $L = 43$ m, a breadth of 37 m and a height of 27 m. The top left sketch illustrates the composition of the tank. A single panel, with typical dimensions of 3300 x 840 x 270 mm (L x W x H) (bottom sketch) is composed by several layers in order to guarantee the adequate mechanical and thermal insulation properties. The inner layer is a corrugated stainless steel membrane which is fixed to a primary polyurethane membrane through a thin plywood sheet, while a secondary one is setted between the hull and the inner layer. Between the two polyurethane membranes is inserted a layer, called Triplex, composed by a membrane of fiberglass fabric and aluminium foil. The containment

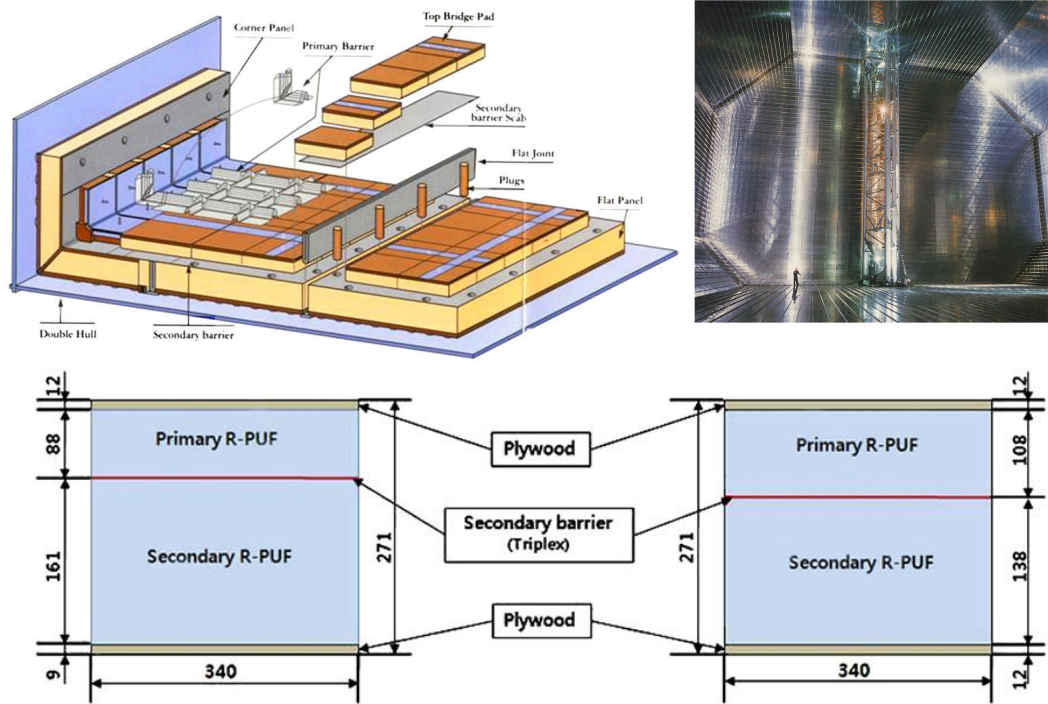


Figure 2.2. Top right: Snapshot of the Mark III tank. Top left: Schematic drawing representing the tank components. Bottom: View in vertical section of a single panel.

system is anchored to the hull with mastic ropes. Between the hull and the containment system, an insulation space is kept inert with nitrogen to permit monitoring the presence of natural gas or water as well as the hull deformation.

According to Faltinsen and Timokha [11], the most relevant natural frequencies of the structure must be scaled. In his numerical study, Graczyk [13] showed as in a single panel of a Mark III several natural modes, with natural frequencies varying in a range between 100-500 Hz, have an important role for the dynamic response of the structure and then for the correct estimation of the maximum structural stresses. He shows that the lower modes, with natural frequencies around 100 Hz, are dominated by the steel response while for the higher ones, starting from 350 Hz, the plywood and foam contributions at the structural response are more apparent. In this work, the prototype structural panel is replaced by a single aluminium plate and only the first natural frequency is properly Froude scaled. For a LNG tank, with a typical length of about 30-40 m and a dimension of the single structural panel of 3 m, the first natural frequency, in fully wet condition, is around 110 Hz. Because the length of the sloshing tank model is 1 m, a geometrical scale factor $\Lambda_L = 30$ is assumed. Then, the length of the panel model is 90 mm and using eq. (2.1), the fully wet natural frequency is about $\sigma_m = 610$ Hz. The length and the natural frequency obtained can be associated to an aluminium beam with the thickness of 2.5 mm by considering the simplified analytical model (eq. 3.32), which will be detailed in the section (3.4).

The Froude scaling of the natural frequencies here used is definitely the simplest way to scale the structural problem. A more accurate procedure should consider also the scaling of the elastic properties associated with the stiffness of the structure. The non-dimensional

natural frequency has to be the same atn the model and the prototype scale. For a beam in a liquid with density ρ_l this non-dimensional frequency associated with the elastic vibration due to bending stiffness EI is $\sigma_n \sqrt{\rho_l L^5 / EI}$ and then:

$$\sigma_m = \sigma_p \sqrt{\frac{\rho_p (EI)_m}{\rho_m (EI)_p}} \Lambda_L^5 \quad (2.2)$$

To satisfy both eqs. (2.1) and (2.2), it is required that $(EI)_m \rho_p = (EI)_p \rho_m$ and $M_B / (\rho_l L)$ must be the same in model and prototype scale. Here ρ is the liquid density, E is the Young modulus of the material, I the bending moment of inertia and L , M_B the length and the mass of the structure, respectively. The simultaneous fulfillment of the above conditions brings to solutions which are difficult to realize with the typical model scale used in a small lab, such as unrealistic small cross-sectional dimension of the beam or liquid and material difficult to manage. We can state that a correct scaling of a hydroelastic problem is still an open problem.

Additional considerations on the model scaling procedure must be taken in account when wave impact with entrainment of gas cavity are reproduced in experimental test. In particular, the hydrodynamic pressure loads in model scale will be larger in the prototype scale if only the Froude scaling is employed. To reproduce the same effects between different scales, also the Euler number must be considered, $E_u = \frac{p_{atm} - p_0}{2\rho U^2}$, where p_{atm} is the atmospheric pressure, p_0 the ullage pressure, ρ is the liquid density and U is a characteristic velocity of the phenomenon, which, in this case, is the horizontal velocity of the wave front approaching the wall. In Faltinsen [11], from a linear analysis of the gas cavity problem the full scale pressure results $(L_p / L_m)^{1/2}$ times the pressure in model scale if both Froude and Euler number are satisfied, while if only the Froude number is considered the pressure ratio between full and model scale pressures is L_p / L_m . This is consistent with the conclusion assessed in Greco et al., 2003, where the authors showed as the nonlinear effects in full scale are overestimated when only the Froude scaling is assumed. On the other hand, the simultaneous fulfillment of both Euler and Froude similarity implies, in model scale, a lower ullage pressure in the tank with respect to the atmospheric one.

While the Euler number is important whenever a gas cavity is present during the impact, the Cavitation number ($C_v = \frac{p_0 - p_v(T)}{2\rho U^2}$, where p_v is the vapour pressure of water at temperature T) matters only when the difference between ullage pressure and liquid vapour pressure is small, inducing cavitation phenomena during the bubble expansion cycles as consequence of the decrease of the inner bubble pressure below the vapour pressure of the surrounding liquid.

In the experimental test the ullage pressure p_0 is changed from the atmospheric value to 25 *mbar* which is very close to the water vapour pressure at a temperature of 20 °C.

2.1.2 Dynamic characterization of the structure

Impulsive tests with a calibrated hammer have been performed to check the dynamic characteristics of the elastic structure as well as the strain gauges dynamics. The hammer test consists in hitting the structure with an impulsive load which excites a wide frequency spectrum. To validate the correct behaviour of the strain gauges, especially in terms of dynamic response, an accelerometer has been mounted as close as possible to the central strain gauge (installed in the centre of the plate). The results of the hammer test have been

compared both in terms of signals time history and spectrum amplitude. They confirm the reliability of the strain gauges measurement, at least until 2.0 kHz (fig. 2.3).

Because of the upper limit in the dynamic response, each observation about the effects of the higher modes with a frequency larger than 2.0 kHz should be regarded as purely qualitative.

Natural frequencies

Concerning the dynamic characterization of the structure, in terms of lowest natural frequency and damping, several hammer tests have been performed by using different filling depths of the tank. In first instance, the dry vibration frequencies have been measured and compared with the corresponding values predicted by the beam theory and by a FEM model applied to the plate. The first two bending frequencies have been compared in table (2.1) showing a good agreement between the experimental results and the theoretical predictions.

Bending mode	Beam theory	FEM analysis	Experiment	Beam theory mass correction
1	1575 Hz	1653 Hz	1486 Hz	1499 Hz
2	4343 Hz	4564 Hz	4318 Hz	xxxx Hz

Table 2.1. Comparison of the first two natural bending frequencies from experiments and from analytical and numerical analyses.

However, the experimental results show a lower values of natural frequencies, especially for the first mode, than those predicted with analytical and numerical tools. The differences can be ascribed to the additional mass induced by either the wire and the strain gauges. This quantity, estimated in 5-7 g is compatible with the difference of the first bending frequency measured and predicted through the beam theory. If in the beam model the mass is increased by 7 g the relative natural frequency decreases to 1499 Hz, which is very close to the measured value (last column of tab. (2.1)). In figure (2.4) is shown the comparison between the calculated wet natural frequency associated to the first mode of the beam and the corresponding value measured during the hammer test as function of the tank filling depth. The comparison highlights the good approximation given by the beam theory (in partially/fully wet condition, eq. (3.32) in section (3.4)).

Damping

If we look at the possible damping terms which characterize the phenomenon, two are the contributions which can play an active role: the hydrodynamic damping due to the boundary layer flow and the structural one. The first one is considered negligible in sloshing flows. Studying the oscillations of an air pocket entrapped by a standing wave at the roof of a sloshing tank, Abrahamsen [1] found that the boundary layer effects in the water domain influence the decay of the pressure signal when the natural frequency of the gas cavity is much larger than the lowest sloshing flow natural frequency. In spite of the high oscillation frequency of the elastic plate, in the damping analysis the structural contribution has been considered as the main term which governs the decay of the measured strain. As for the natural frequency, the hammer tests with different filling depths have been used to estimate the structural damping. In particular, the decay of the stress free-vibration response has been

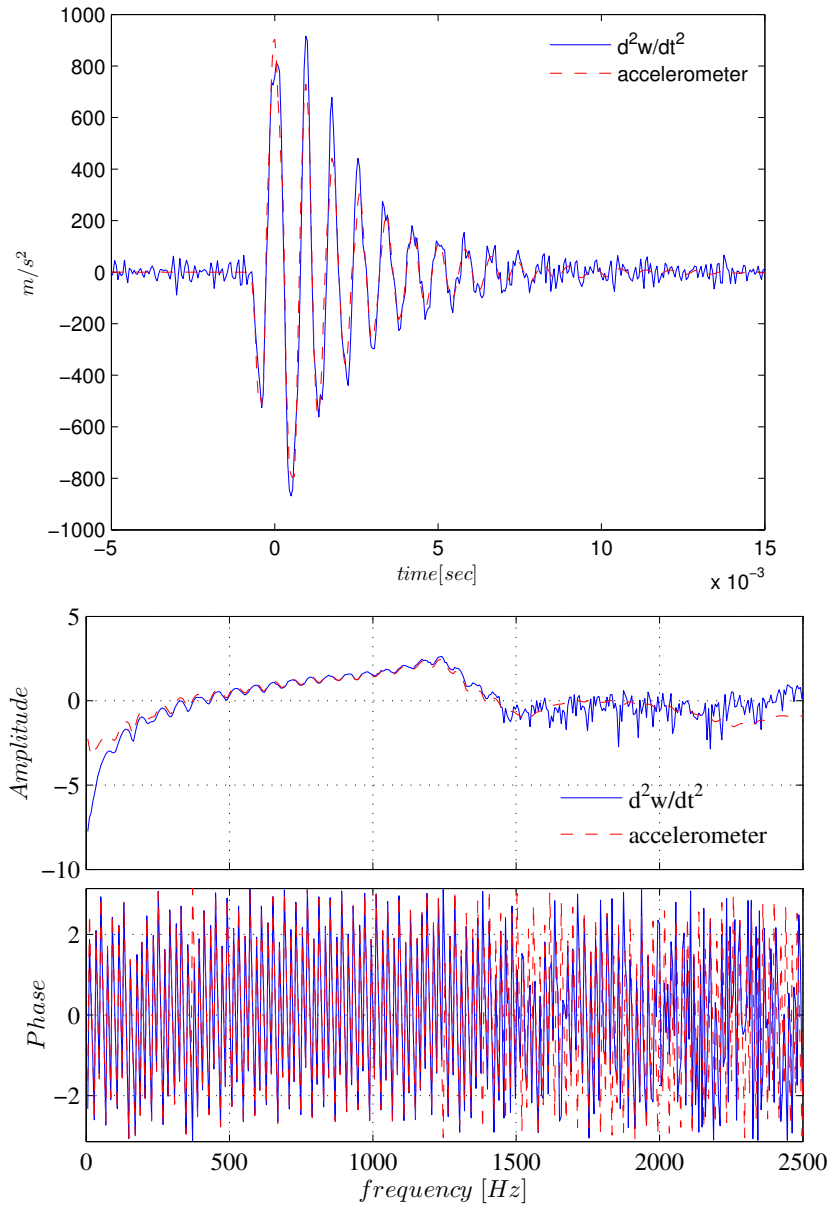


Figure 2.3. Top panel: comparison of the temporal evolution of acceleration during hammer test. The blue line and the dashed red line represent the acceleration measured by strain gauges and accelerometer respectively. Bottom panel: Comparison of acceleration FFT in term of amplitude and phase.

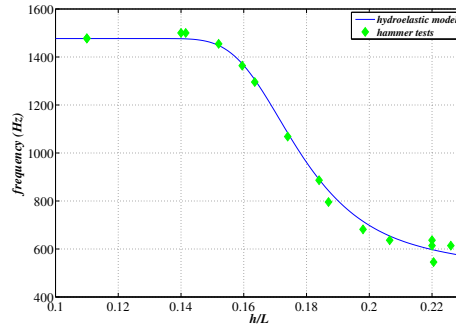


Figure 2.4. Comparison of the beam lowest natural frequency in wet hammer test as function of the filling depth. The green markers show the behaviour of the first natural bending frequency of the structure while the continuous line correspond to the values predicted by the hydroelastic model.

evaluated by assuming as solution of the problem of a damped mass-spring linear system:

$$q(t) = Q_0 \exp((- \xi \omega_n + i \omega_n)t) \quad (2.3)$$

where ξ is dimensionless damping term, ω_n the natural frequency and Q_0 a constant which depends on the initial conditions. Note that only the first mode has been considered for each filling depth and a suitable constant damping coefficient has been identified. In figure 2.5 the behaviour of the structural damping coefficient for several filling depths in calm water condition is reported. The values of the coefficient ξ (blue dots in figure) have been estimated through the hammer test. Their behaviour, as function of the wetted length of the structure, is well fitted by a cubic function (red line). The dashed black line represents the pure structural damping in a fully dry condition. The figure highlights how the presence of calm water increases the damping of the structure when stressed with an impulsive load.

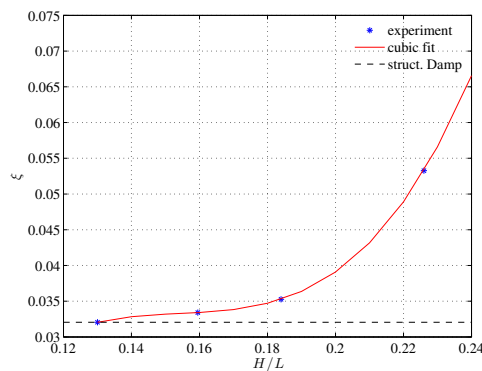


Figure 2.5. Behaviour of the dimensionless values of the structural experimental damping coefficient relative to the lowest structural mode (symbols). The solid line represents the cubic functions which fits the symbols. The dashed line reports the values of the structural damping in dry conditions.

2.2 Wave scenarios

Depending on the wave typology, its impact against a wall can be more or less characterized by high hydrodynamic loads. Its shape, at the moment of the collision, is influenced by several parameters as the seabed topography, the water depth at the wall, three dimensional effects and also the structure of the wall. For a non steep wave, the linear theory is sufficient for a good description of the wave impact evolution and for the estimation of the hydrodynamic loads, which are of the order of $\rho g(h + H)$, if the shallow-water framework is considered, where ρ is the liquid density, g the gravity, H the crest wave elevation and h the water depth [30].

The most relevant cases of wave impacts are those concerning nearly breaking or breaking waves. In this case, the interaction of the wall with the wave (fig. 2.6) can lead to different scenarios but for all of them the occurrence of extremely localized impulsive loads is concrete.

For a nearly breaking wave, the interaction with the wall can lead to water velocities many times greater than $[g(h + H)]^{1/2}$. Otherwise, when a forward jet is developed from the wave crest the entrapment of a gas cavity may happen, or if the wave is fully broken, a turbulent front composed by a mixture of air and water hits the wall.

A classification of the different scenarios which may occur is the following:

1. “Flip-through”, the wave impacts without air entrapment.
2. Plunging breaker with small amounts of air entrapped.
3. Plunging breaker with a large air pocket.
4. Turbulent bore.

Bagnold [3], in his experimental activities, observed that the maximum pressure is associated to the impact for which a small amount of air is entrapped. Recent study asserts that the maximum pressure is due to a plunging breaker with large air pocket and occurs at the still water level (SWL) [16]. Also Chan and Melville [6] in their study, observed that the maximum pressure is reached when a wave plunging is developed before the impact and the

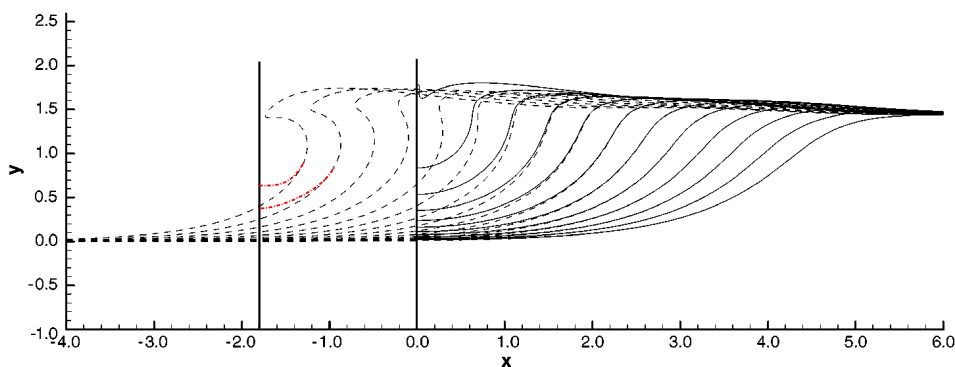


Figure 2.6. Interaction of a nearly breaking wave with a vertical wall. The dash lines show the wave temporal evolution in the absence of the wall, while the continuous lines represent the evolution of the same wave interacting with the wall.

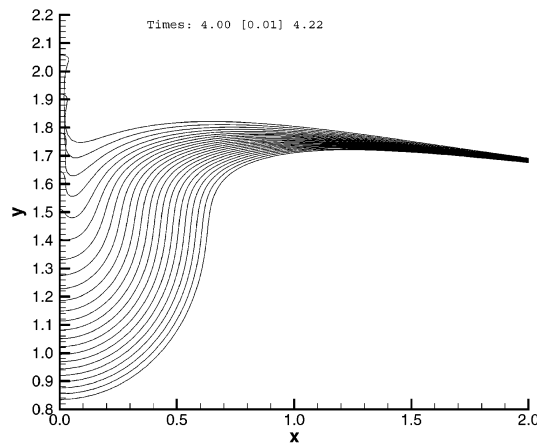


Figure 2.7. Numerical temporal evolution of the wave profile in case of flip-through impact (see [30]).

direction of crest incidence is approximately horizontal. In this case a significant amount of air is entrapped during the impact.

The poor repeatability of the maximum pressure, measured during the impact, is a constant in several experimental studies [3], [23], [6], this is due to the high sensitivity of the wave front to small changes of the environmental conditions, such as small surface waves or the roughness of the vertical wall.

In the case of wave impact against deformable walls, such as those of a tank, the estimation of the maximum pressure, as an indicator of the real stress acting on it, is not a suitable choice. Because of the impulsive and localized behaviour of the hydrodynamic load, also hydroelastic effects may appear during the impact evolution, increasing the loads on the structure. The direct measurement of the structure deformation is a better indicator for the structural stress particularly in the presence of hydroelasticity.

In the present hydroelastic study, two classes of wave impacts have been examined. They are presented in the next sub-sections and will be detailed both of them from the kinematic and the dynamic point of view, considering the impacts occurring against a rigid wall.

2.2.1 Case A) Flip-through

When a steep wave approaches a vertical wall a flip-through impact may happen, (producing elevated local hydrodynamics loads). As described in [24], three different stages are identified during the final evolution of this impact scenario: (i) *wave advancement* where the wave front, moving towards the vertical wall, forces the wave trough to rise up along it; (ii) *wave focusing*, during this stage the wave trough and the front approach each other on a point at the wall triggering the (iii) *flip-through* stage. During the latter, a sudden turning of the flow is generated, close to the focusing point, producing an energetic vertical jet. A detailed description of the time evolution of the wave profile is shown in fig. (2.7) where it is possible to recognise the three different stages, which characterize the impact evolution.

Figure (2.8) shows the pressure time evolution recorded by the pressure transducers during the flip-through impact against the rigid panel. The red line refers to the mean value of the pressure on five repeated tests, while the black one refers to a single test where the kinematic evolution is shown in fig. 2.9. For the latter, in each panel is plotted the vertical

distribution of the pressure along the wall (red marker). The dashed red line shows the interpolation of the pressure signals, whose positions, along the wall, are marked with the green diamonds.

In the *wave advancement* stage ($t \leq -10$ ms), from fig. 2.8 it is observed an almost linear trend of the pressure signals for the transducers below the instantaneous free surface. The trend of hydrodynamic load is due to the slow rise up of the wave trough the wall. The small vertical velocity is such that, during this stage, the hydrostatic pressure prevails over the dynamic one, $\frac{Dy}{Dt} \ll -\mathbf{g}$ and the problem is dominated by the quasi-static term. A consequence is that the spatial pressure distribution is quite uniform and decreases with the distance from the bottom of the tank to reach the ullage pressure on the free-surface. In figure 2.8, this behaviour is highlighted by a black dashed line in the panel of probes P_1, P_2 . For each probe, the lines represents the hydrostatic pressure $\rho gh(t)$, where the vertical distance of the probe from the instantaneous free-surface $h(t)$ has been measured from the fast-cam images recorded during the experiment. The slope represents the wave trough vertical velocity which is almost constant.

Moving forward in time, the vertical acceleration of the wave trough increases pushed by the approaching of the wave front to the wall, (from panel A to B in fig. 2.9) this is highlighted by the nonlinear variation of the pressure in time. The effect on the spatial pressure distribution is an increase of its value near the free surface for the action of the fluid acceleration.

Around $t = 0$ ms, we have the *focusing stage*, where the rapid increase of the vertical velocity makes the inertial term $\frac{Dy}{Dt}$ dominant with respect to the gravitational one, characterizing both the spatial and temporal evolution of the hydrodynamic load. In figure (2.9) it is possible to note, at the instant labeled C in special way for the pressure transducer 5, the sudden increase of the pressure, which reaches a maximum value (approximately equal to 10 times the undisturbed hydrostatic pressure). To show the real predominance of inertial effects over the gravitational one, a rough estimation of the vertical pressure gradient can be calculated by taking the derivative between two subsequent pressure transducers, $\frac{1}{\rho} \frac{\partial p}{\partial y} \approx \frac{1}{\rho} \frac{\Delta p}{\Delta y} \approx 520 \text{ m/s}^2$, this means that the inertial acceleration is approximately 54 times \mathbf{g} .

It is possible to observe how all the pressure transducers located below the probe 5 record the local maximum value of the pressure at the same time and how such values decrease with the distance from the focusing area. This highlights the localized behavior in space of the hydrodynamic load for this kind of wave impact (see also vertical pressure distribution on panels C-D in figure 2.9). For the probes located above the free surface during the *focusing stage*, the maximum values are reached with a small time delay, consequence of the steadiness of the phenomenon in a reference system moving with the maximum pressure peak, which moves, approximately, with the same vertical velocity of the wave trough. A large scattering of the pressure signals is observed during the focusing stage, as a consequence of the highly local behaviour of the pressure distribution at the impact time. Conversely, a good repeatability is observed during the other stages of the evolution. The spatial pressure distribution shows the location of the focusing area around the probe 5.

In the last stage, *flip-through*, as consequence of the large pressure gradient just below the free surface, a vertical jet flow is triggered at the wall (panels C, D and E in fig. 2.9). Because the probes P_6 and P_7 are dry during the previous stages, the pressure signals, recorded by these two probes, grow nearly instantaneously up to their maximum value when wetted by the vertical jet. The recorded values are lower than the maximum pressure

recorded in the focusing area. For the other probes a sudden decrease of the pressure signals is observed.

Subsequently, the vertical flow, developed during the *flip-through* stage, continues until all its kinetic energy is converted in potential energy. Later, the gravitational effects will drive the problem, accelerating downward the flow.

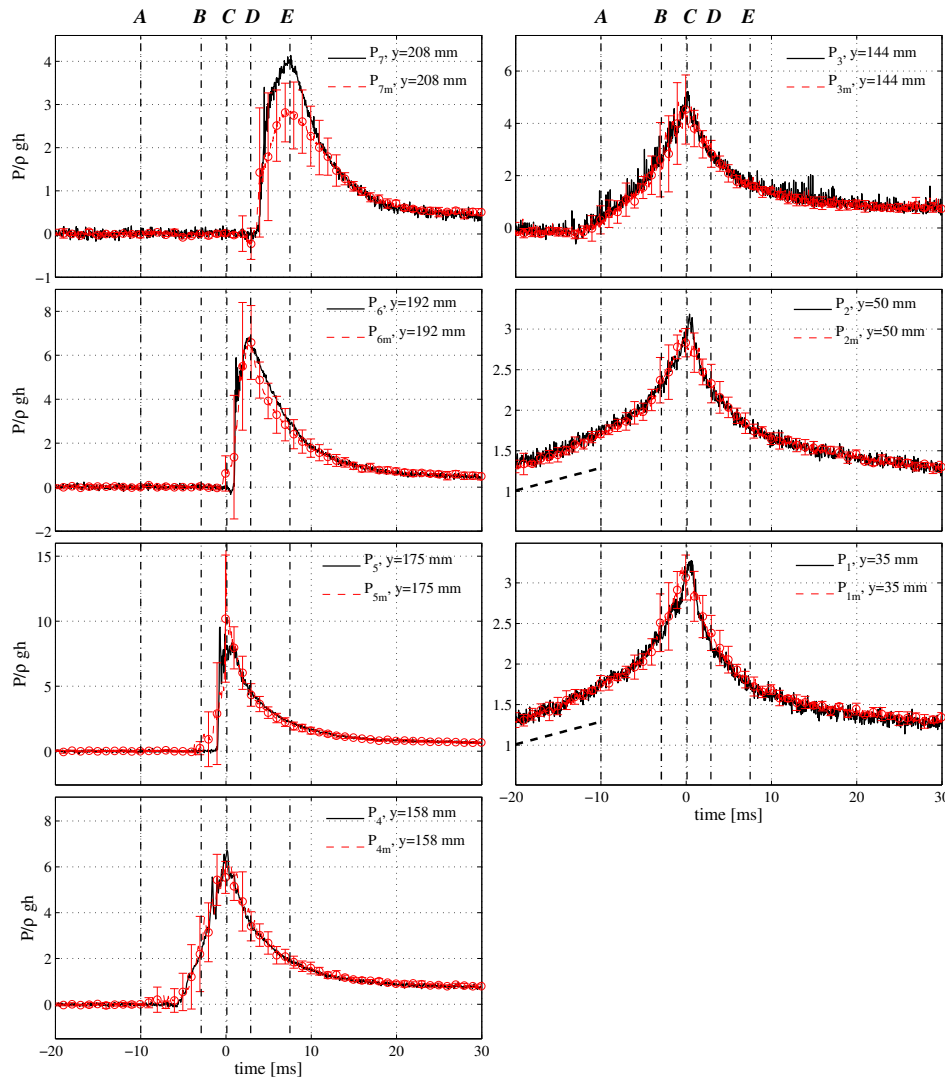


Figure 2.8. Each panel shows the time history of the pressure transducer along the rigid vertical wall. Their vertical position ($y=0$ corresponds to the tank bottom) is indicated on the panel. The red line represents the mean value calculated with 5 repetitions of the same run, the error bar identifies the relative standard deviation. The black line shows the pressure value measured during a single test, fig. (2.9), where the frames shown refer to time instants labelled A, B, C, D, and E.

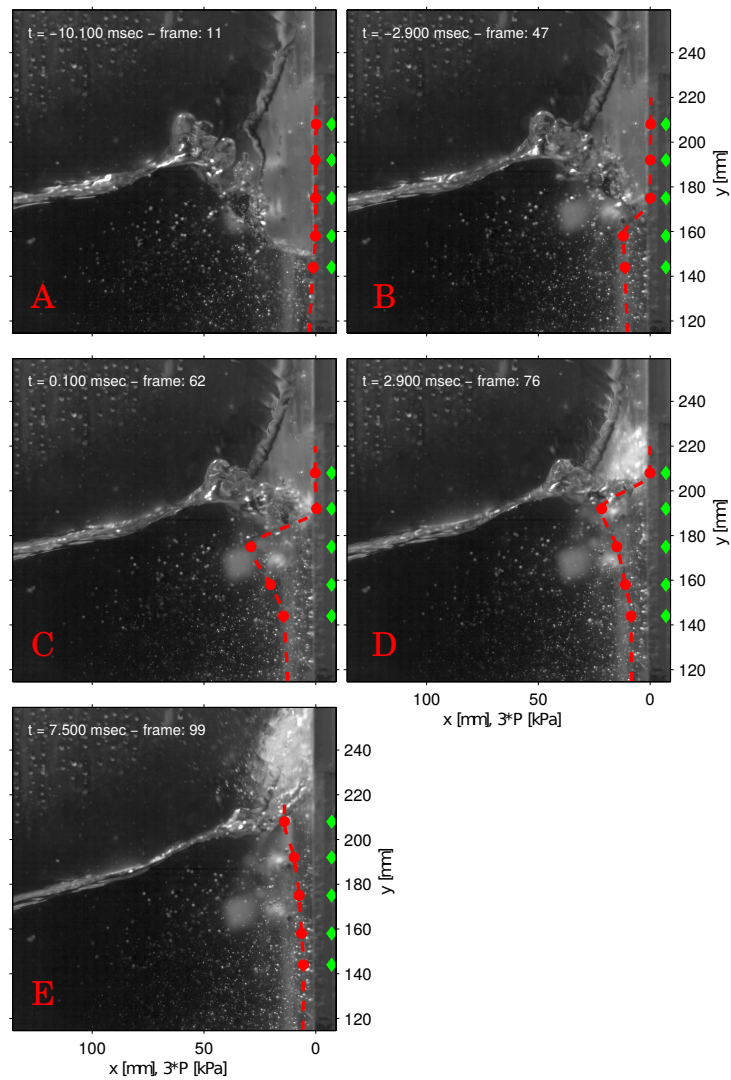


Figure 2.9. Evolution of the flip-through impact at five different times. The green diamonds indicate the pressure transducers position. The red line represents the interpolation of the pressure data recorded (red circles).

2.2.2 Case B) Gas cavity

The entrainment of a single gas cavity, during an impact phenomenon, occurs when a breaking wave approaches a vertical wall. As for the flip-through, also for this impact typology it is possible to characterize its kinematic evolution in different stages [24]

In figure (2.10) the fast cam snapshots of the wave configuration in different stages are reported, the green markers show the pressure transducers position, the dashed red line shows the hydrodynamic pressure distribution along the vertical wall. As for the flip-through it has been obtained with the interpolation of the transducer signals. In the plot the pressure time histories for two pressure transducers respectively located at 175 mm and 50 mm from the bottom of the tank are reported. The vertical black lines indicate the position of the 5

snapshots. The first stage is the *closure* of the cavity against the wall (first snapshot). It is mainly characterized by the gas leakage from the forming cavity caused by the surrounding water flow, which compresses and forces the gas to escape from the cavity. The leakage phenomena are crucial for the definition of the initial conditions of the subsequent stage in terms of pressure and density of the gas.

After the cavity is closed there is a phase of *isotropic* compression/expansion due to the compressibility of the gas. From the second to the fourth snapshots the first compression of the cavity, characterized by the maximum value of the pressure and the two following expansions are shown. The term isotropic refers to an almost equal deformation of the cavity boundary in all the directions. During this stage the cavity maintains the same position and it is not raised up by the vertical water flow. This is due to the gas compressibility which counteracts the flow acceleration. Similar to the flip-through impact, the vertical distribution of the hydrodynamic load, at the impact instant, is quite localized in space and the area where the maximum load is exerted is around the gas cavity.

Subsequently (fifth snapshot), the isotropic behaviour changes toward an *anisotropic* one. The compression/expansion of the cavity is characterized by a vertical stretching due to the surrounding vertical water flow. In particular, while in the lower part of the cavity, the high pressure gradients are still able to counteract the water flow, in the upper part the fluid flow prevails inducing a local compression against the wall and consequently its vertical deformation. The last stage displays the rise of the cavity along the wall pushed up by the water flow and its subsequent fragmentation in smaller bubbles.

From the dynamic point of view, the analysis of the pressure recorded in the impact against a rigid wall shows a well-defined oscillation of this quantity. In particular, while the first pressure peak is dominated by inertial effects, i.e. the strong acceleration of the fluid flow on the wetted part of the wall and the initial compression of the cavity due the water mass approaching the wall, the *isotropic* and *anisotropic* compression/expansion stages are mainly governed by the compressibility of the gas and this is confirmed by the oscillatory behavior of the pressure. After the oscillatory stage, the remaining part of the evolution is mostly governed by gravity, which acts on the mass of water accelerated upward during the previous stages, forcing it to a free fall along the vertical wall. Several are the parameters which influence the dynamic behaviour of the cavity; from the theoretical point of view in [34] Topliss gives the estimation of the cavity natural frequency (f_r) considering a potential two-dimensional problem of a semicircular bubble under the hypothesis of small oscillations, the following expression is valid when the cavity is close to the free-surface:

$$fr^2 = -\frac{2\gamma p}{4\pi\rho r^2 \log(r/2h)} \quad (2.4)$$

where p is the atmospheric (ullage) pressure, ρ is the water density, γ is the ratio of specific heat, r the initial bubble radius and h the distance of the bubble from the free surface. Equation (2.4) shows a proportional dependence of the natural frequency on the ullage pressure and an inverse dependence on the bubble radius.

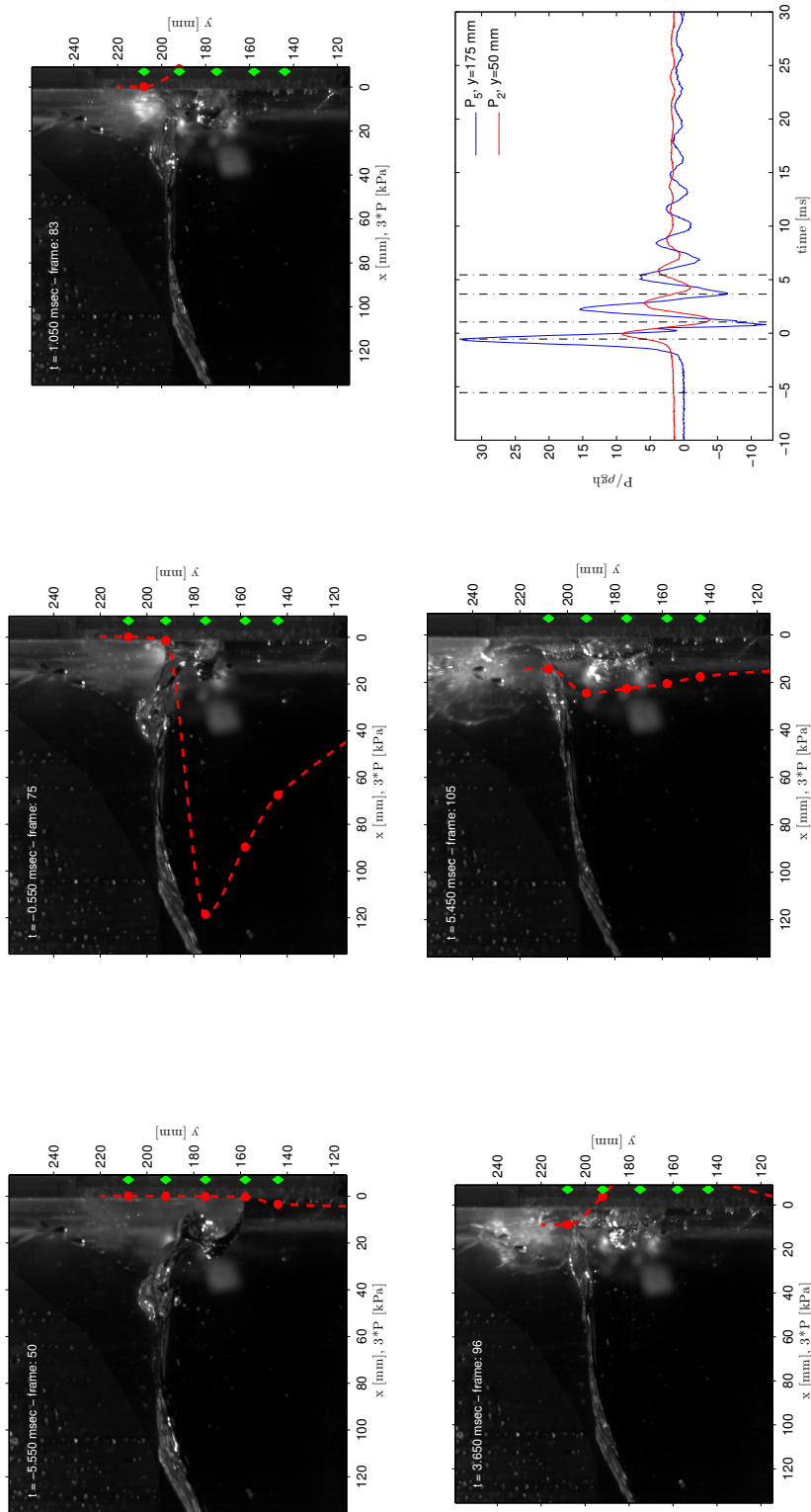


Figure 2.10. In the five snapshots the kinematic evolution and the hydrodynamic pressure profile along the vertical wall are reported. The red dots show the instantaneous values of the pressure recorded during the experiment by the pressure transducers highlighted by the green diamonds. In the plot the pressure time histories are shown. The blue and the red lines represent the signals of sensors 5 and 2, respectively. The five dashed black vertical lines identify the snapshots time instants.

2.3 Discussion of the results

2.3.1 Flip-through impact

In the previous section, the kinematic and dynamic characteristics of the flip-through impact against a rigid wall have been discussed, here, it is presented the case of impact against an elastic structure. While the kinematic evolution of the flow shows the same characteristics between the two cases: evolution divided in the stages, *advancement*, *focusing* and *flip-through*, the dynamic behaviour appears totally different especially after the *focusing stage*.

Figure 2.11 shows the temporal dynamic evolution of the elastic case. In particular, the three upper plots show the dimensionless stresses with respect to the yield stress of aluminium ($\sigma_y = 15$ MPa), recorded by the strain gauges installed at $y = 192$, 175 and 158 mm respectively. In the lower plot is shown the hydrodynamic pressure measured on the rigid part of the vertical wall, at $y = 35$ mm from the bottom of the tank. The pressure is made dimensionless with respect to the hydrostatic pressure in undisturbed condition. In the plots are reported the mean value signals and the associated error bar of stresses and pressure, calculated through 5 repetitions of the same run.

During the first part of the evolution, named *wave advancement* stage, the behavior of the structural stresses, as well as of the pressure, reflects the quasi-static behaviour observed in the rigid case: a slow deflection of the structure due to the slow rise up of the wave trough along the vertical wall. Moving toward the focusing instant (t close to 0 ms), the structural deflection velocity increases non-linearly due to the growing of the fluid vertical acceleration at the wall, until, when a time instant between those labelled B and C (in figure) is reached, the rise time of the hydrodynamic pressure is comparable to the highest natural period of the structure and then it is able to excite the corresponding natural modes of vibration. From this instant the second stage starts, called *fully hydroelastic* which governs the dynamic evolution of the phenomenon up to $t \approx 5$ ms. At time $t = 0$ ms, the structure reaches its maximum displacement. The maximum value is recorded by the strain gauges installed in the middle of the structure ($y = 175$ mm) and this indicates that the first natural mode is the predominant one. The asymmetric behaviour of the maximum values recorded by the other two strain gauges highlights the presence of the higher modes too. From the *fully hydroelastic* stage and for the subsequently instants, the stresses behaviour is characterized by an evident oscillation with the frequency equal to the lower wetted natural frequency of the structure. Also the hydrodynamic pressure recorded by the probe shows the same oscillatory behaviour and this emphasizes the role of the hydroelasticity if compared with the signal recorded by the same probe in the rigid test (probe P_1 in figure 2.8). Looking at the maximum value recorded by the pressure probe, this, in the elastic case, is about twice than that in the rigid wall case. The increase of the hydrodynamic load can be ascribed to the structural reaction, in particular, after the structure reaches its maximum deflection, it moves against the incoming wave, opposing to the hydrodynamic load (which is increased up to its maximum value at time D). The hydroelastic (coupling/behaviour), which is identified with the opposite phase of oscillation between the pressure and structure deflection, goes on for the three next oscillations of the signals ($t = 6 - 7$ ms). Later it is possible to identify a further stage called *free-vibration* where the beam behaves like a free oscillating system. As for the previous stage, there is an opposition of phase between deflection and pressure signals.

As said before, both stress and pressure signals are characterized by a frequency which is ascribed to structural wetted natural frequency. Such frequency is not constant in time because depends on the instantaneous wetted length of the structure. The more the structure is wet, the more the added mass effects will reduce the natural frequencies. To investigate the strong nonlinear and transient signal which characterize the flip-through event, the Fourier Transform is not the best tools, since the stationarity and periodicity of the signal is required for a proper employ. For such kind of signal, the Empirical Mode Decomposition (EMD) is a more suitable mathematical tool since is based on the Hilbert Transform, which allows the definition of the instantaneous frequency and the relative amplitude of the signals. An additional step of the EMD is the identification of the Intrinsic Mode Functions (IMF) of the signal: i.e. the original signal is decomposed in several signals with zero mean value and each one characterized by a well defined frequency. In the upper plot of figure (2.12) are shown both the temporal evolution of the dimensionless stress signal (blue line) and the first

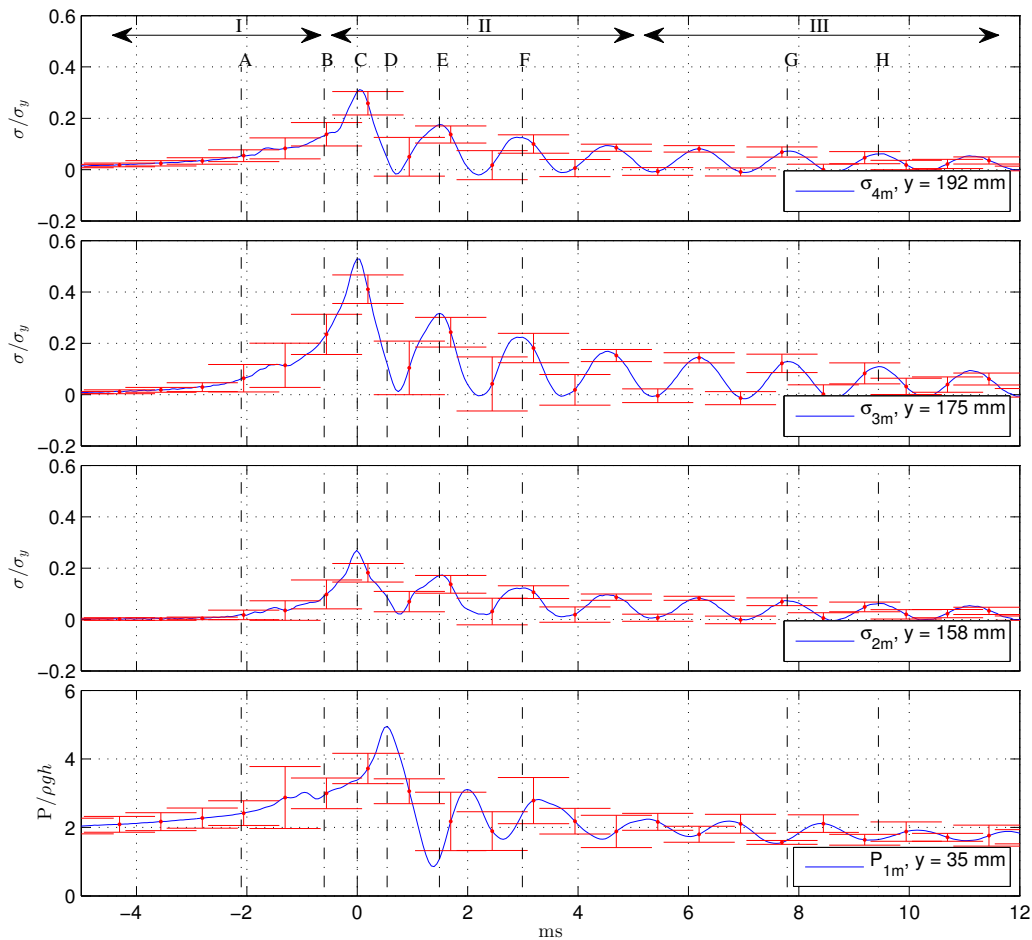


Figure 2.11. Dynamic temporal evolution of the flip-through impact against an elastic structure. The three upper panels show the dimensionless stresses recorded by the three central gauges. In the lower panel the hydrodynamic pressure measured close the tank bottom is shown. The black arrows in the upper panel identify the *stages* of hydroelastic impact.

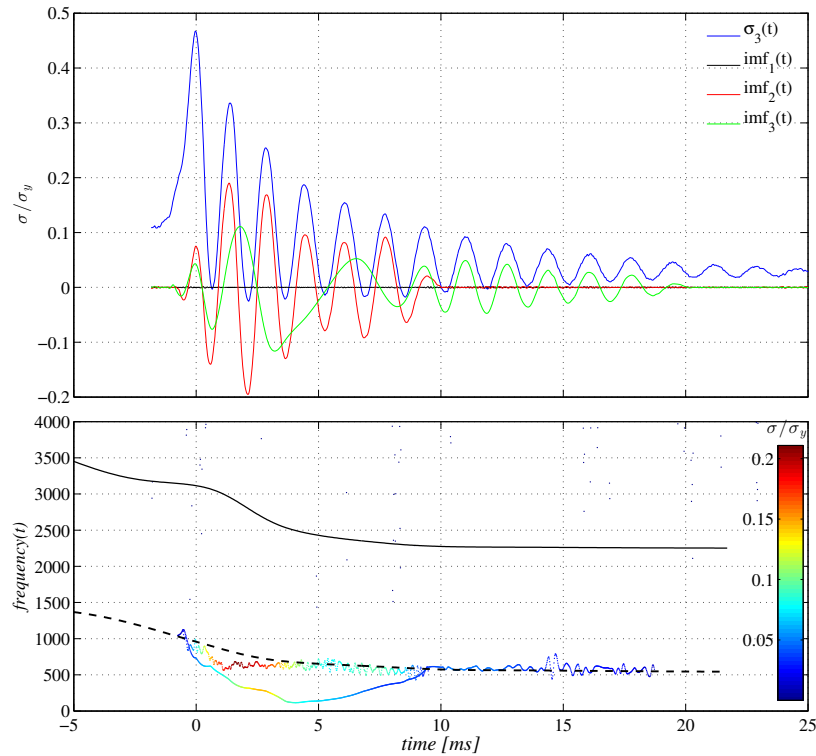


Figure 2.12. Top panel: Time history of the dimensionless stress measured in the middle of the beam and the first three IMF estimated with the EMD. Bottom panel: Time history of the instantaneous frequencies, which characterize the three IMF reported. The dashed and continuous black line show the theoretical variation of the first two wet natural frequencies of the beam, respectively.

three IMF obtained with the decomposition. With the exception of the (quasi-static trend) the second and the third IMF are sufficient to describe the whole oscillatory behaviour up to 20 ms. In the lower plot the instantaneous frequencies of the IMF are shown (scatter plot, where the color represents the IMF signal amplitude) compared with the theoretical ones estimated through an analytical model with the help of fast-cam images, which had allowed to evaluate the beam wetted length (dashed and continuous black line). The variation of the principal instantaneous frequency is in a quite good agreement with the theoretical variation of the first natural wet frequency. The first IMF amplitude, which reproduces the effect of the higher modes, is almost zero because the central point of the beam is a stationary point for the second mode and the third one is not so influent. The second IMF contains the first six oscillation cycles characterized by the dominant frequency which changes its value from about 1 kHz to 600 Hz, which is the expected value for a fully wet condition for the structure. For $t > 10$ ms, the third IMF is the one which contains the most part of the original signal and the frequency is almost constant in time. This means that the variation of the added mass effects in the last hydroelastic stage is quite null oppositely to the previous one, where a quick variation occurs.

Similarly as done in the previous section, also in the flip-through impact, for the estimation of the dimensionless damping coefficient ξ the same approach has been used, i.e. the signals have been considered as a free-vibration response of a linear system. The mean value obtained is about $.0315 \pm .0039$. Such value, collocated on figure 2.5 corresponds to the damping for a filling depth of about $0.125 L$, which means, for the beam, a fully dry condition. Differently from the results obtained in the static test, where the value of the damping coefficient increases with the wetted length of the structure, here during the wave impact, although the water is rising up along the structure, the damping coefficient does not change with respect to the dry condition.

2.3.2 Impact with gas cavity

The breaking waves which are studied during the experimental activities have been generated by imposing a pure sinusoidal motion to the sloshing tank with a fixed period of oscillation equal to $T = 1.6 \text{ sec}$. By changing the motion amplitude A , it has been possible to investigate three cavities with different size respectively named *large* ($A = 65 \text{ mm}$), *medium* ($A = 63 \text{ mm}$) and *small* ($A = 61.5 \text{ mm}$), each one characterized by an oscillation frequency inversely proportional to the initial cavity size. The ullage pressure, and hence the Euler and Cavitation numbers, has been varied from the atmospheric value down to values close to the vapour pressure of the water in order to study the influences of the cavity frequencies and to reproduce as much as possible the phenomena present in the full scale problem. The differences observed between the impacts against rigid and elastic wall are highlighted in the following, paying particular attention to the characteristics of the dynamic system in terms of natural frequencies and damping.

Figures 2.13-2.15 show the wave configuration just before the impact against the vertical wall for the three cases considered. In each figure the impacts at the different ullage pressures and the related structural stresses measured by the strain gauge installed in the middle of the plate ($y = 175 \text{ mm}$) are reported. The stresses in the plots are normalized with respect to the yield stress σ_y . The red circle in the plots shows the time instant of the image. The kinematic evolution in the elastic case is the same as in the rigid case for all the cavities studied and for all the ullage pressure considered.

The repeatability of each run is shown in figures 2.16-2.18, where the mean value of the structural stress has been calculated with 5 repeated tests. To avoid the spreading of the signal due to small changes in the frequency of oscillation, for each run, i.e. same cavity size and ullage pressure, the mean value has been calculated by considering the signals in the non dimensional time scales t/T_n , where T_n is the first natural period of the cavity.

All the signals show an oscillatory behaviour characterized mostly by the first natural frequency of the cavity. As much as the ullage pressure decreases, the influence of the non-linear effects, due to gas compressibility, becomes more evident, characterizing the signal with sharper peaks and flatter troughs. For the *medium* and *small* cavity, the time scales which characterize the first peaks of compression are such to excite the natural frequencies of the structure (rise time $\approx 1 \text{ ms}$). As consequence of that, it is possible to observe a higher oscillation frequency, just after that peak. It starts to be particularly evident for the cases with an ullage pressure lower than 200 mbar. In this condition, the longer expansion phase as well as the low hydrodynamic loads allow the structure to oscillate with its natural wetted period. In the other cases, the structural natural modes are mostly hidden by the oscillation due the cavity dynamics.

A quantification of the error due to the different cavity oscillation frequency is shown in figure 2.19. Here the mean values of the natural frequencies for each cases are plotted with their error bars as function of the ullage pressure. The frequency fluctuations about the mean value decrease with the ullage pressure. In the plot, the natural frequencies calculated in the elastic case (blue lines) are compared with those obtained for the same cavity in the rigid case (red lines). For both cases the values decrease with the ullage pressure. While for the *large* cavity (dots in the plot), the value of the frequencies is almost the same for both the rigid and elastic case, with the exception of the test at atmospheric pressure, a different behaviour is observed for the other two cases, *medium* and *small* cavity. Especially for the *medium* cavity, the natural frequencies are lower for the elastic than for the rigid case, and

the differences fall down with the ullage pressure.

Similar to what already done for the estimation of the damping for the structure in case of impulsive test, also for the impact cases the linear non-forced damped mass-spring response is used. The temporal behaviour of the signal peaks is expressed as a simple exponential law $y = y_0 e^{-\xi \omega_n t}$, where y_0 depends on the initial condition and the exponential decay $\xi \omega_n$ is the product of the damping coefficient ξ and the angular frequency ω_n . In figure 2.20 the damping coefficient (top plot) and the exponential decay (bottom plot) are plotted for the three cavity sizes as function of the ullage pressure, both for the elastic and rigid case, line and dashed line, respectively. The damping estimation for the elastic case has been calculated on the structure deflection signal, while for the rigid case the pressure signal has been used. Because both deflection and pressure signals are characterized by a nonzero mean value the mean trend was removed from the original signal. Such mean trend has been calculated as the mean value of its maxima and minima envelopes (fig. 2.21). For the *large* cavity (blue line) the exponential decay decreases with the ullage pressure up to 600 mbar and then it is quite constant and the differences between the rigid and elastic case are small (continuous and dashed line). For the other two cavities (red and green line), their values decrease for all the ullage pressures and the values in the elastic case are smaller with respect to the rigid case. These differences are reduced for the lower pressure. For the damping coefficients, in terms of differences between rigid and elastic cases, it is possible to observe an analogue behavior of both the exponential coefficient and the natural frequencies: large differences for the *small* and *medium* cavity, which decrease with the pressure and smaller differences for the *large* cavity. In terms of the damping coefficients, for *small* and *medium* cavity in the rigid case, they are quite constant with the pressure, around 0.15 and 0.12 respectively, while all the other cases show an initial drop, up to 600/800 mbar with a successive increase up to 100 mbar where they reach their maximum value. Figure 2.22, shows how the exponential law, assumed for the decay, fits the peaks of the signal for the elastic and rigid case, blue and red line, respectively. While for the rigid case the approximation is quite good for the whole time evolution, in the elastic case a different behaviour has been observed for the different cavities. In the elastic case, the approximation used shows a good agreement for the *large* cavity and for the first oscillation periods of the *medium* and *small* cavity, for these latter a decrease of the exponential decay in the subsequent time evolution has been observed, as shown in figure 2.22. Such behaviour of the exponential decay is present for the *medium* cavity for all the ullage pressures and for the *small* cavity only for pressure between 1000 and 600 mbar, with a mean value respectively of 54 ± 26 and 58 ± 20 (1/sec) for the exponential decay.

Particularly in low ullage pressure condition, during the first expansion of the cavity, the hydrodynamic pressure of the liquid in contact with the cavity, can reach values close or lower to the vapour pressure of the water and trigger cavitation phenomena. In figure (2.23, left column) the minimum values of hydrodynamic pressure recorded by the pressure sensors are plotted. The continuous and the dashed line show the values obtained from the sensors installed at 5 cm from the bottom of the tank, respectively, in the rigid and elastic test, while the dot-dashed line is the measurement in the impact area in the rigid test (≈ 17 cm above the bottom of the tank). The black dashed line shows the vapour pressure of water at $T = 20^\circ\text{C}$. The log-scale representation shows clearly the asymptotic behaviour of the pressure. For the *small* and *medium* cavity the differences between the value recorded on the bottom and in the impact area are reduced with the pressure, while for the *large* cavity the maximum difference is observed for an ullage pressure of 400 - 200 mbar. Small

differences between elastic and rigid cases can be observed for the *small* and *medium* cavity for almost all the ullage pressures, while for the *large* cavity they appear only at atmospheric pressure. Also such differences, whose behaviour is similar to the one observed also for the cavity natural frequency and damping, could be ascribed to a hydroelastic interaction. No cases of cavitation have been highlighted by the pressure transducer signals, but this does not exclude that local cavitation phenomena could occur, specially in the test at 50 mbar where the mean minimum value reached is 39 ± 11 mbar. In the right column of figure 2.23 the maximum values of structural stress and hydrodynamic pressure recorded respectively in elastic (top) and rigid (bottom) test are plotted. In the elastic test, the behaviour of the stresses shows an increase for the structural loads specially for the *medium* and *small* cavity as the Cavitation number tends to zero. For the rigid test, the hydrodynamic pressure is almost constant for the *large* cavity, while shows a small increase for the *medium* cavity and a pronounced increase for the smallest cavity specially for C_v lower than 5. It is worth to note that the maximum values of hydrodynamic pressure recorded are strongly influenced by the position of the pressure transducer with respect to the “real” location of maximum pressure and this could justify the large increase observed for the *small* cavity.

The differences observed between the rigid and elastic cases, both in terms of natural frequencies and exponential decay coefficient, can be ascribed to a hydroelastic interaction between the structural and gas cavity dynamics. In particular, the most clear signal of such interaction is the elongation of the “life time” of the gas cavity oscillations and this is reflected in a prolongation of the structural stresses too. The fact that for *large* cavity or impacts in low Cavitation number condition ($C_v < 0.9$) the hydroelastic effects are missing or strongly reduced can be ascribed to a larger difference between the cavity and structural natural frequencies of oscillation and the whole system behaves like a forced mass-spring system. In terms of the scaling problem between model and full scales, the importance of the Cavitation and Euler numbers, concerns not only the correct scaling of the hydrodynamic pressure but also the effects of a hydroelastic interaction.

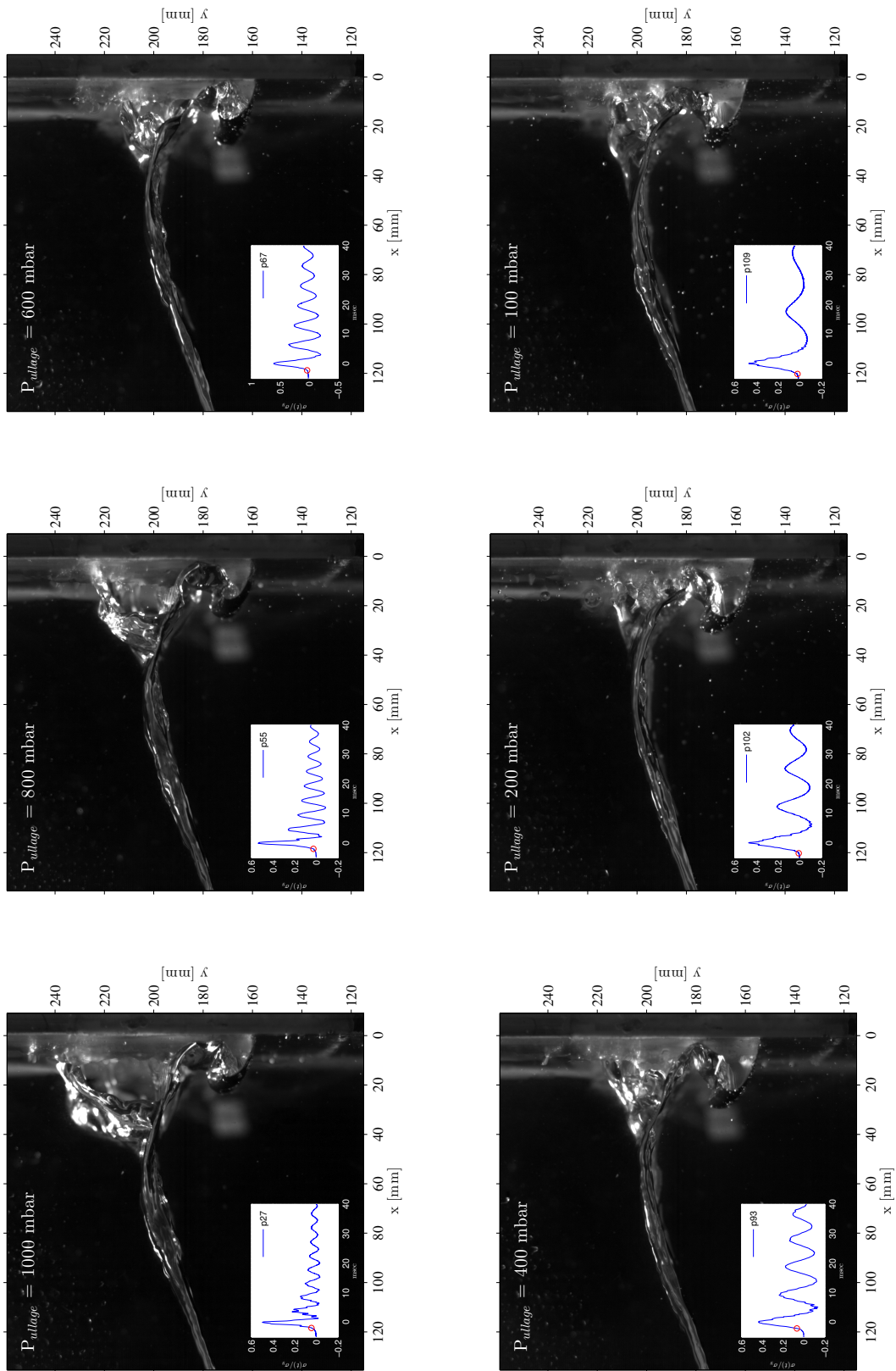


Figure 2.13. Large size Cavity. The six snapshots shows the wave front configuration just before the impact against the elastic vertical wall for different ullage pressures. In each snapshot, the time evolution of the recorded structural stress is reported. The circle before the first peak show the snapshot position in the stress time history.

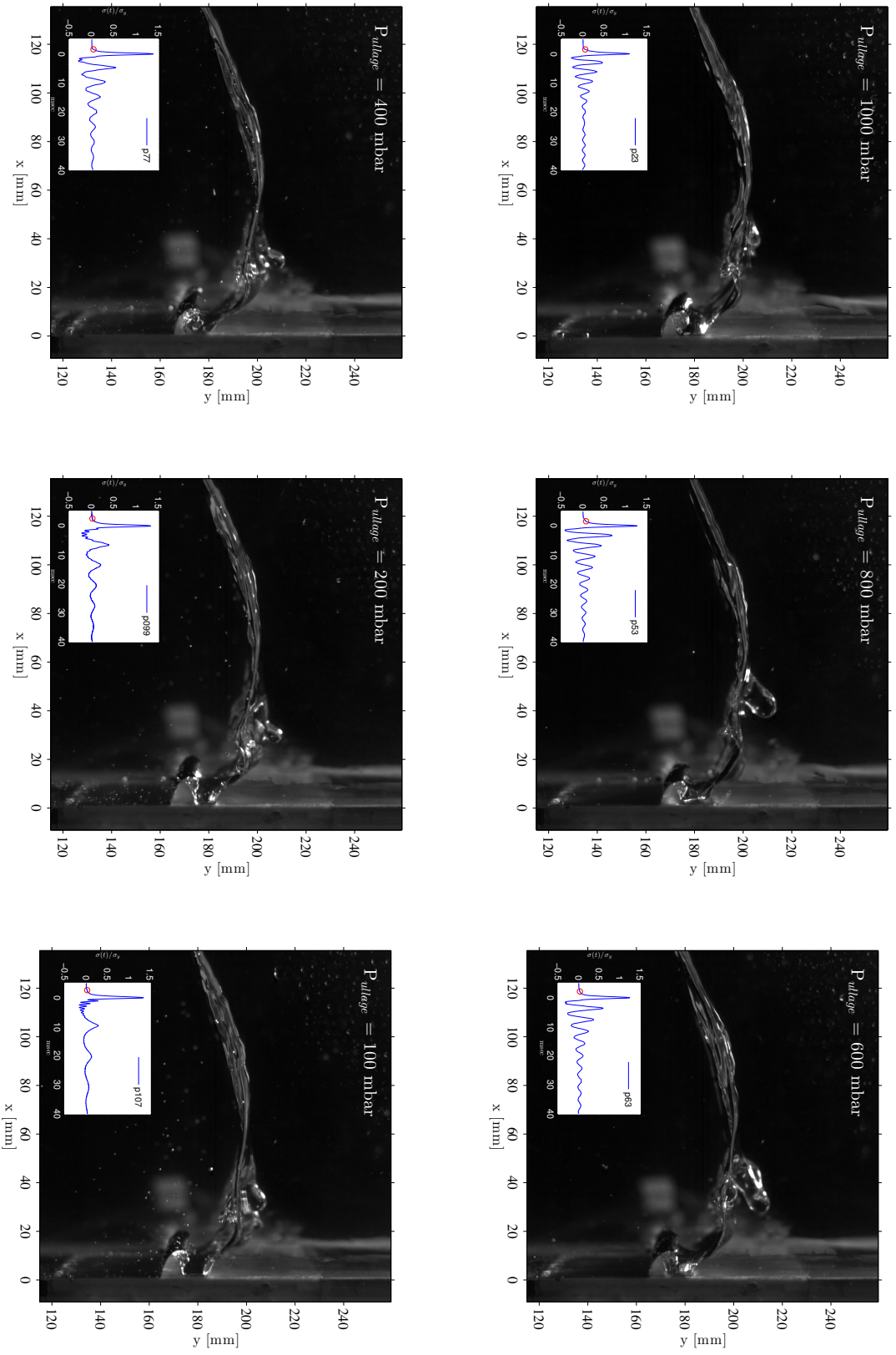


Figure 2.14. Medium size Cavity. The six snapshots shows the wave front configuration just before the impact against the elastic vertical wall for different ullage pressures. In each snapshot, the time evolution of the recorded structural stress is reported. The circle before the first peak show the snapshot position in the stress time history.

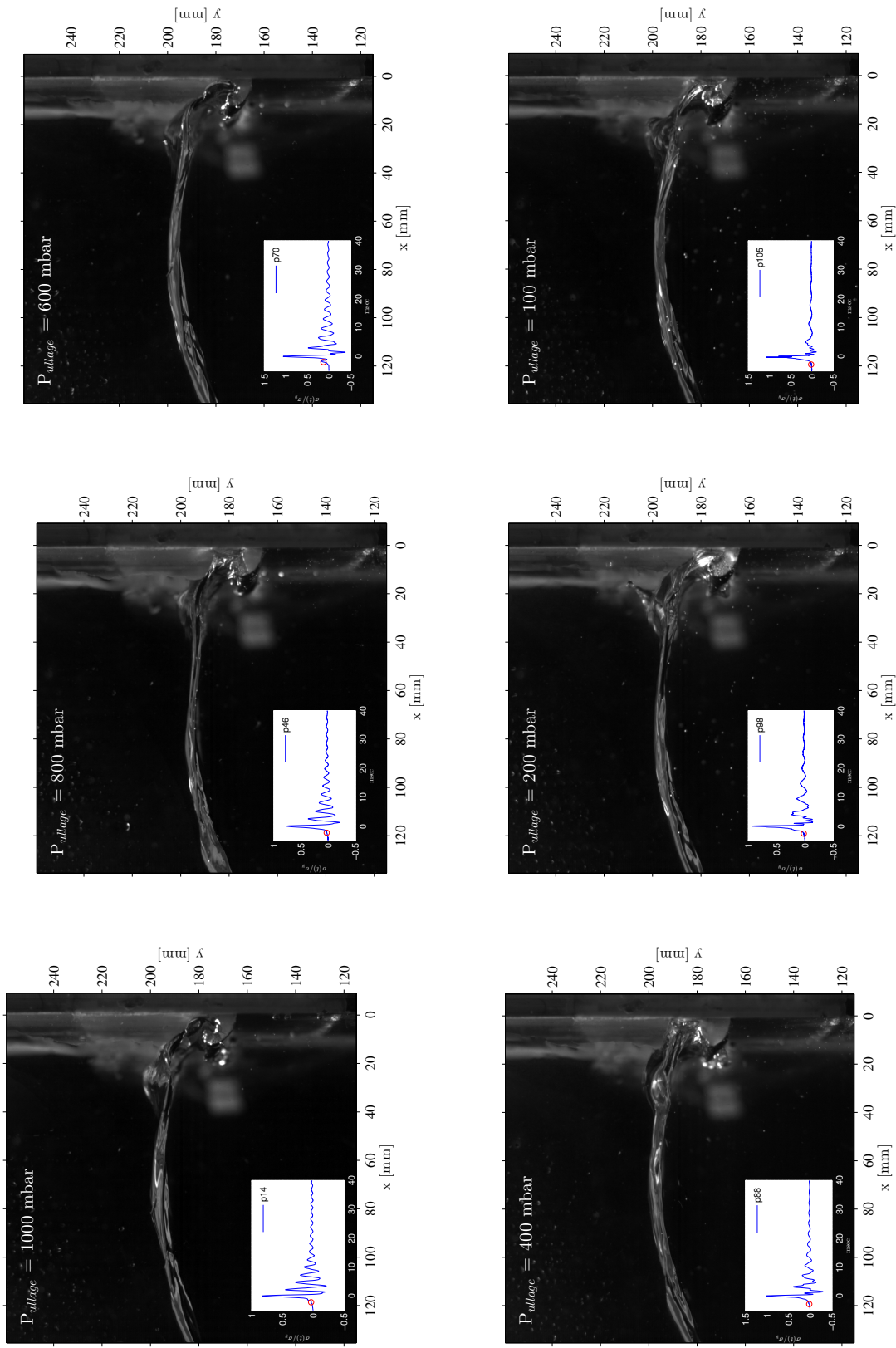


Figure 2.15. *Small size Cavity.* The six snapshots shows the wave front configuration just before the impact against the elastic vertical wall for different ullage pressures. In each snapshot, the time evolution of the recorded structural stress is reported. The circle before the first peak show the snapshot position in the stress time history.

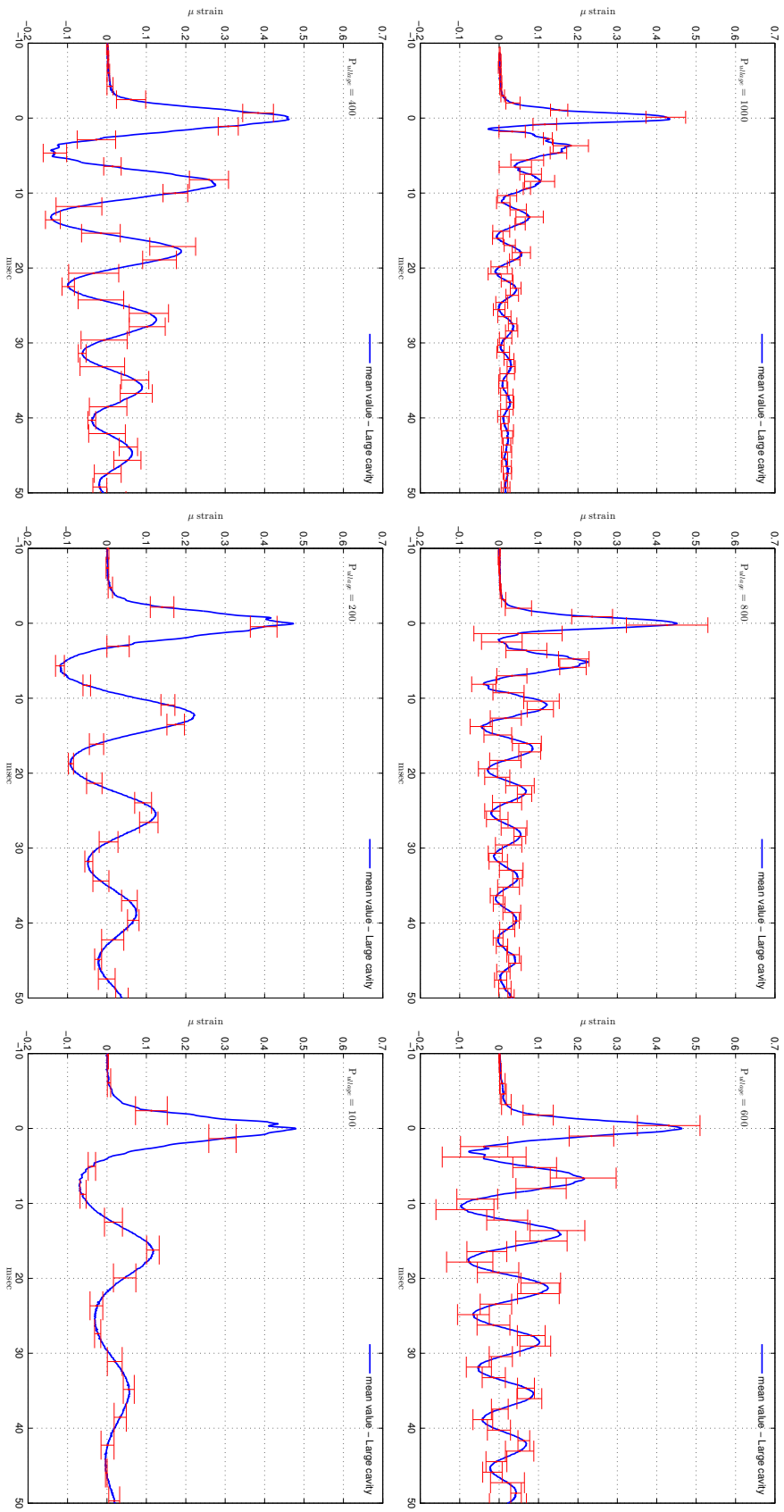


Figure 2.16. Large size Cavity. Time evolution of the mean normalized stress measured in the middle of the structure.

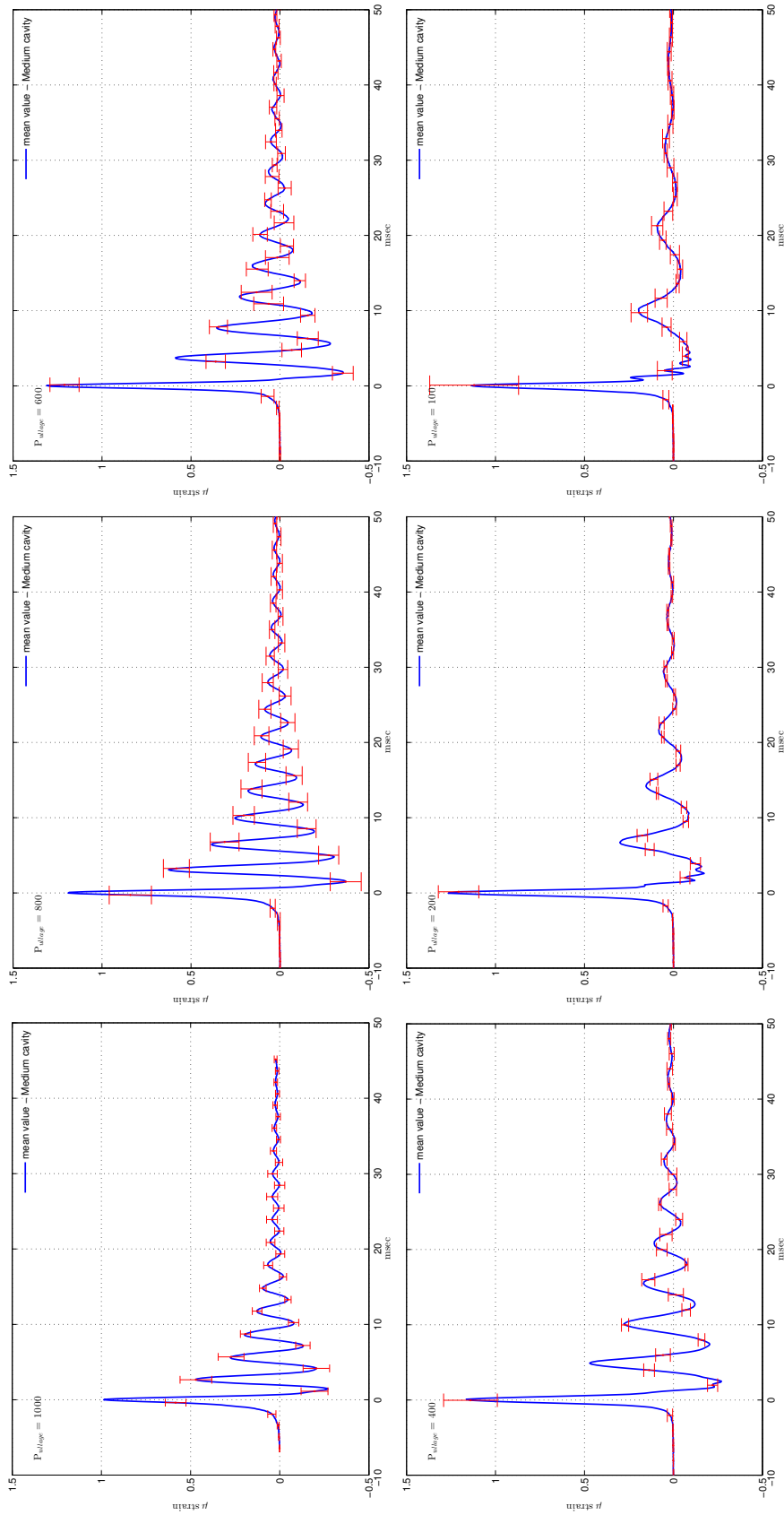


Figure 2.17. *Medium size Cavity.* Time evolution of the mean normalized stress measured in the middle of the structure.

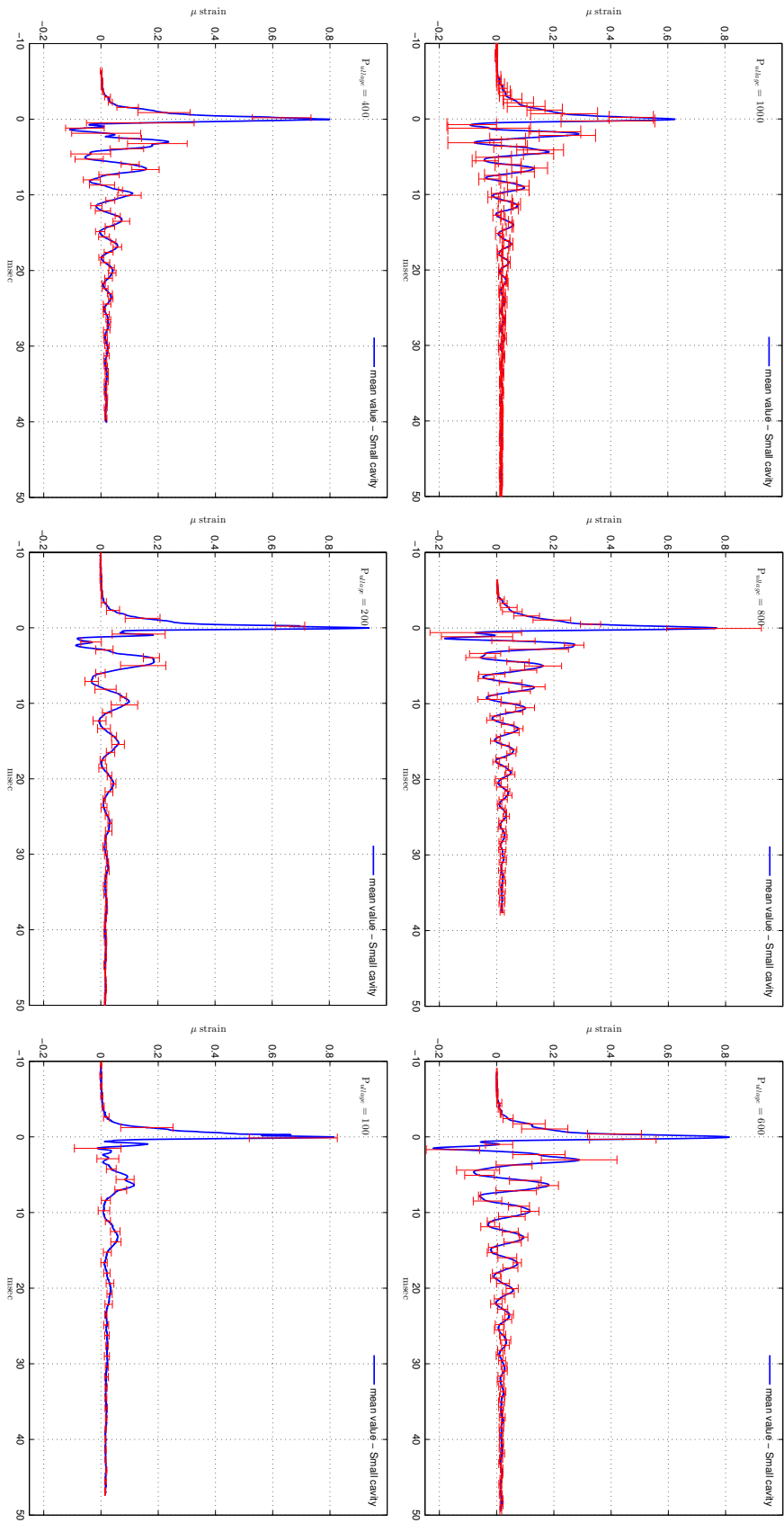


Figure 2.18. Small size Cavity. Time evolution of the mean normalized stress measured in the middle of the structure.

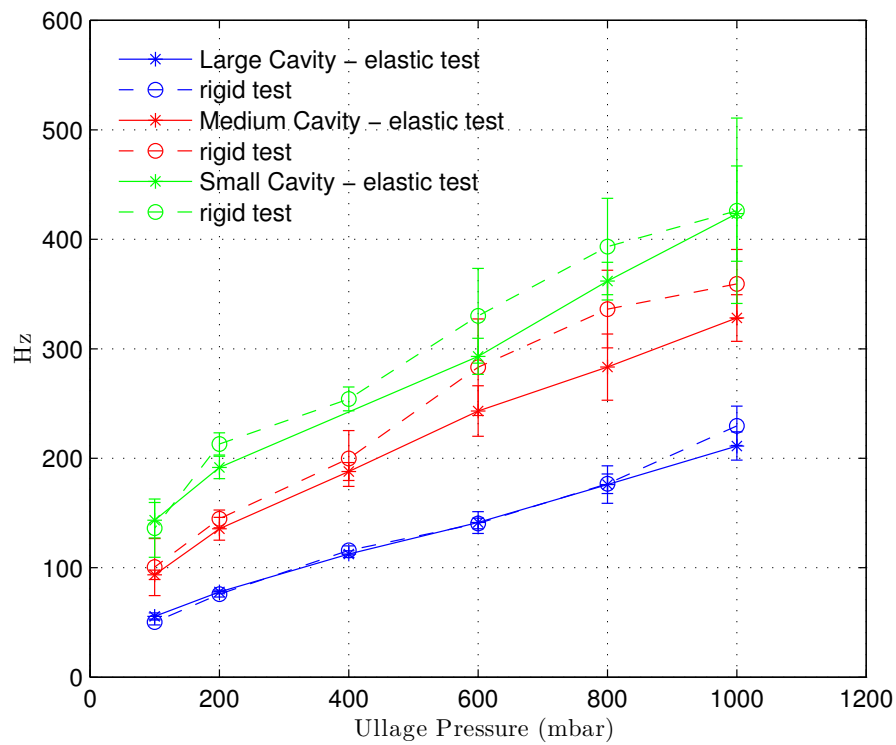


Figure 2.19. Lowest natural frequency of the gas cavity as function of the ullage pressure for rigid (blue line) and elastic test (red line) for the three different cavity sizes.

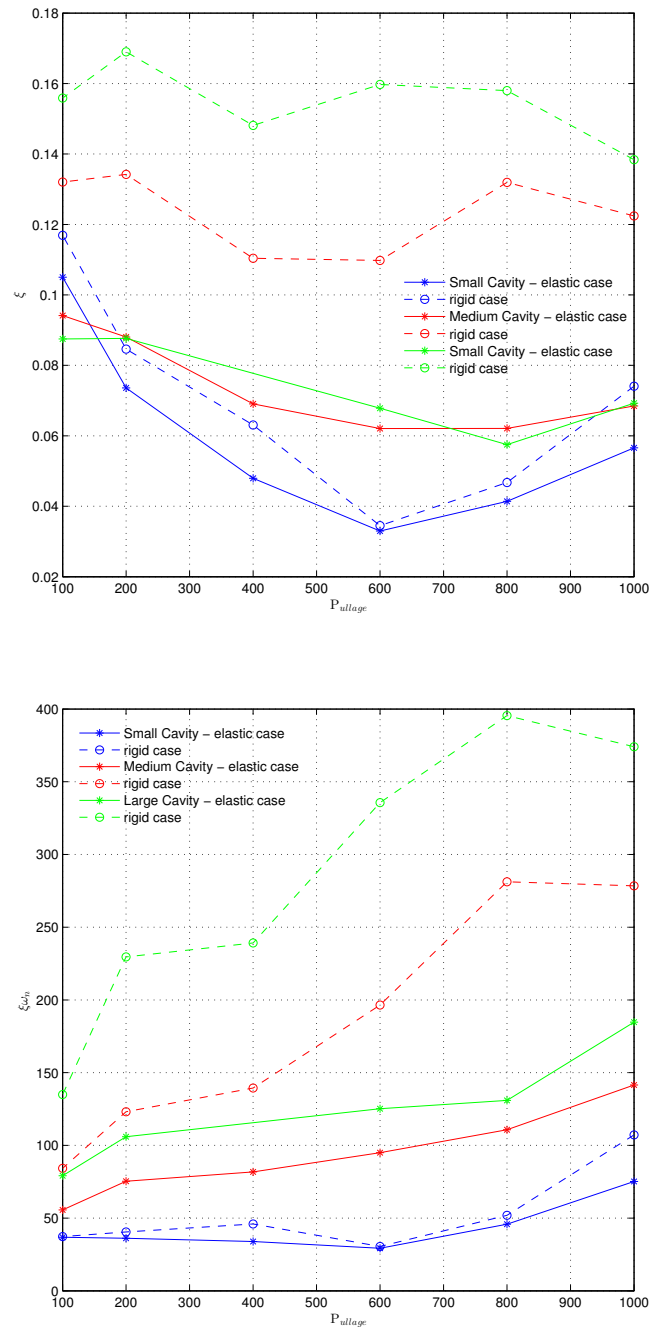


Figure 2.20. Damping ratio (top plot) and exponential decay (bottom plot) for the different cavity size impact as function of the ullage pressure.

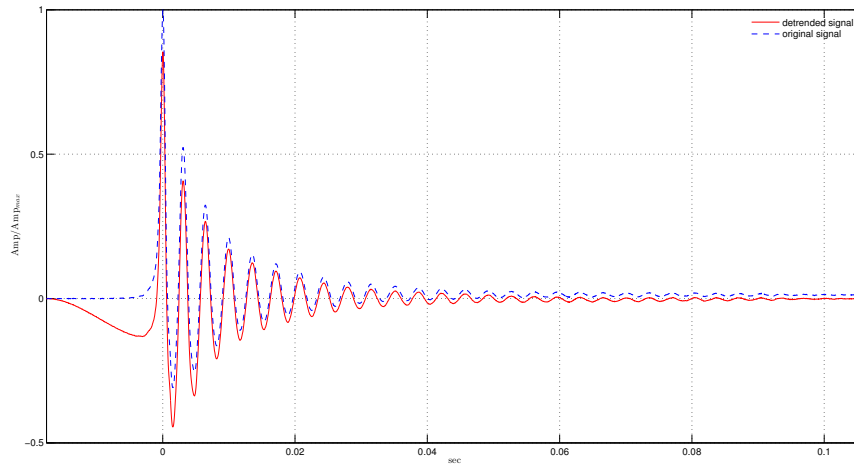


Figure 2.21. Comparison between the original signal (blue dashed line) and the de-trended one (red continuous line), which has been used for the estimation of the exponential decay.

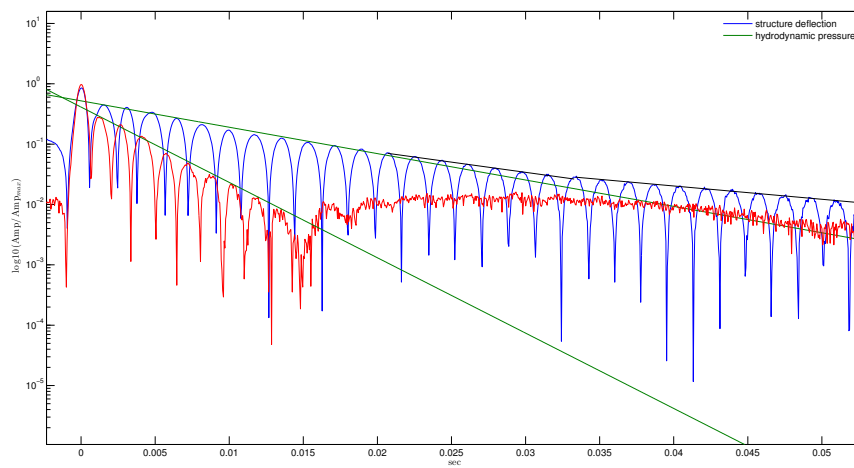


Figure 2.22. Exponential fitting and damping stages for the elastic case.

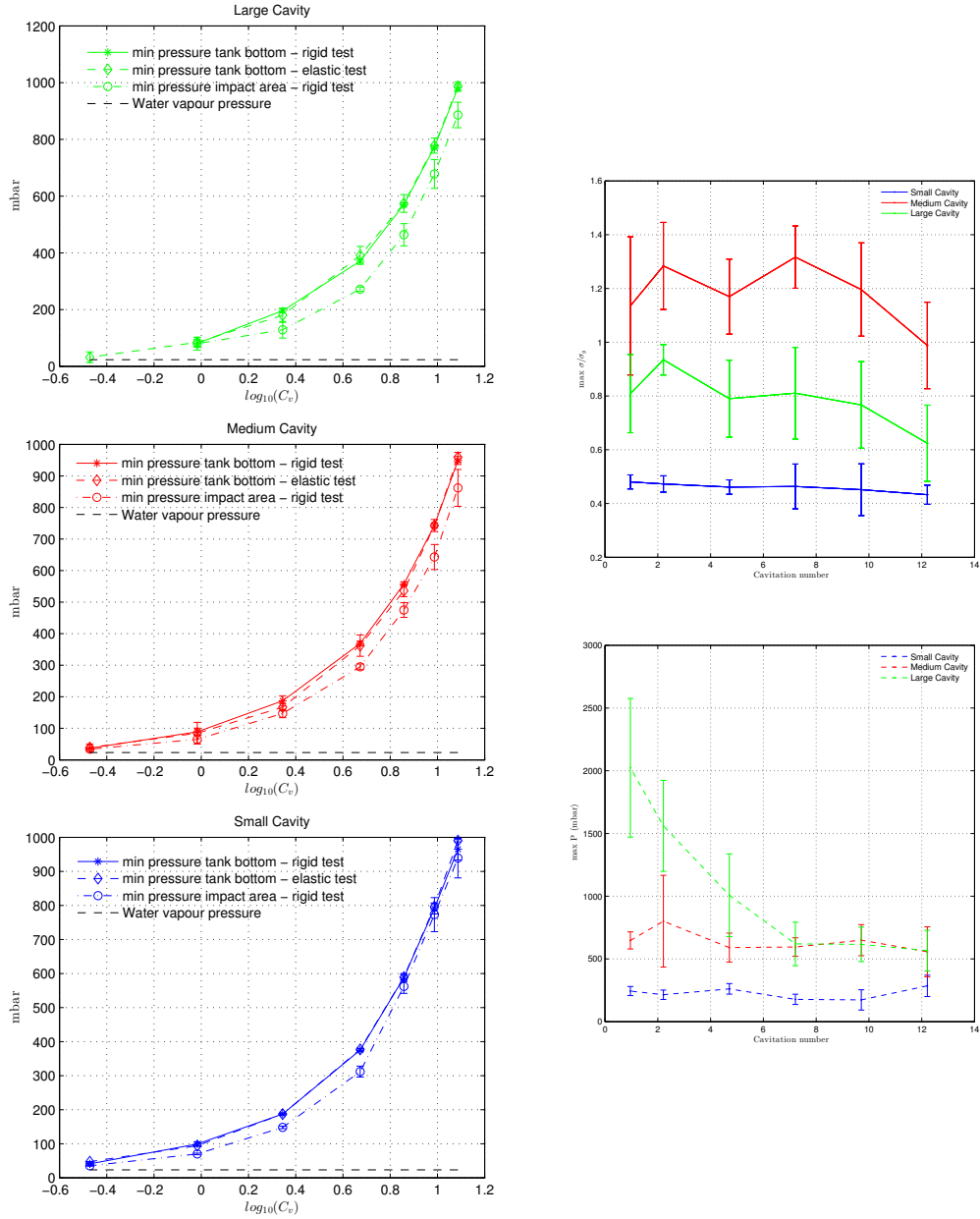


Figure 2.23. (Left column): Values of the minimum pressure recorded during the experimental test for the three cavities as function of the cavitation number (log scale), ullage pressure from 50 to 1000 mbar. (Right column): Maximum values of the structural stress (top) and hydrodynamic pressure (bottom) as function of the cavitation number.

Chapter 3

Mathematical Model

In this section the mathematical approach for studying the hydroelastic problem will be discussed. The development of a mathematical tool is required for a better understanding of the main physical features which are actively involved in the overall event. These were highlighted during the experimental activities but due to the phenomenon complexity and to the difficulties to quantify them with laboratory apparatus it was not possible to investigate them in depth.

With the aim to study a problem characterized only by the relevant physical features, a simplified model will be proposed, based on observations done during the experiments as well as from the literature.

The global problem will be split in three sub-problem:

- 1a) Single-phase sloshing problem
- 1b) Two-phase sloshing problem - Gas cavity problem
- 2) Structural problem

and each of them will be discussed separately. Moreover, two semi-analytical hydroelastic models will be presented, concerning the flip-through and the impact with gas cavity. Both of them do not consider the full coupling of the identified sub-problems, in particular, the sloshing problem has been treated in a very simplified way. While for the flip-through impact the hydrodynamic loads are obtained from the experimental activities concerning the rigid test, for the gas cavity wave impact the sloshing stage has been completely neglected and the impact problem as been treated in a similar way as for a water entry problem. The solution of the complete hydroelastic problem, with the coupling of the different sub-problems, will be presented in the next section from the numerical point of view.

3.1 Physical assumptions for the hydroelastic problem

The experimental findings highlighted that the wave impact event which may occur during the evolution of sloshing flows in a tank is a complex problem because it may involve multiphase flows with violent fluid-structure interaction. It is characterized by physical phenomena extremely localized in time and space; they may excite hydroelastic effects when the typical time duration of the local hydrodynamic load is shorter or comparable with the typical natural period of the structure. A suitable mathematical model must take into account all these features. Navier-Stokes equations for the hydrodynamic flow field, (possibly) coupled with a proper model for the structural part is definitely, the more complete mathematical method to be used at the purpose. However, it could be extremely challenging and expensive to be solved numerically, in particular when multiphase flows are involved.

Some simplified assumptions are necessary for modeling the phenomenon; they must be done looking at the physics of the event as it will be detailed in the following. A first simplification arises from the modality used to originate the wave-impact events considered in the present investigation. Indeed, the experimental motion of the tank has been properly designed in order to realize an *ad hoc* impact phenomenon during the first two or three oscillations of the tank and such that the desired impact is the first one which occurs. Because of this assumption, we can distinguish two stages in the overall flow evolution: i) Single phase hydrodynamic problem, which characterizes the evolution of the sloshing flow until the beginning of the impact event. This is identified hereinafter as *sloshing stage*; ii) Single or two-phase hydroelastic problem, which characterizes the flow evolution during the impact event. In this case the local hydrodynamic problem, single or two-phase depending on the modality of the wave impact, i.e. without or with air-cavity entrapped, is coupled with the structural problem. This is identified hereinafter as *hydroelastic stage*.

More in detail, two different scenarios have been considered in the present experimental investigation during the hydroelastic stage: a) flip-through case; b) an almost breaking wave that impacts against the wall entrapping a single and well defined gas cavity and producing a two-phase flow.

Note that this simplification is not valid as it is for a general motion of the tank; more precisely, a robust procedure must be found in order to recognize automatically the occurrence of an impact event. However, the aim of the present work is the understanding of the hydroelastic behavior of a structure when a wave impact occurs; the capability of the numerical model to be generalized will be left to future studies.

A second strong simplification is directly related to the two-dimensional assumption done in building the experimental set-up. This motivated the geometry of the tank, with a dimension along the transversal direction which is one tenth of the in-plane one, and the motion of the tank, which is prescribed along the longitudinal direction only.

Because of the experimental simplification, the mathematical and numerical models considered in this work will be 2D.

Although the accuracy used in the preparation of the set-up and in the execution of the experiments, some of the flow phenomena experimentally observed were intrinsically three dimensional. This is the case, for example, of the breaking wave entrapping air; the almost breaking wave crest approaching the wall was characterized by transversal instability on the wave front, inducing not negligible 3D effects on the closure of the cavity and on the related air-leakage flow [24], [25]. This is expected to strongly influence the damping of the local loads. Although the 3D effects are not directly modeled in the numerical approach proposed,

they will be considered as possible bias in the comparison of the numerical results with the experimental data.

3.2 Mathematical Model for the sloshing stage

For the sloshing problem, which concerns the fluid motion up to the starting point of the impact phenomena, the hypothesis of incompressible and irrotational fluid have been adopted, then the fluid behaviour can be modelled with the potential flow theory. The effects of viscosity have been neglected mainly for two reasons, the first one is the short time evolution of the fluid flow (2-3 sloshing cycles), which does not give enough time for their development and the second one is the greater contribution of the inertial force term with respect to the viscous one in the momentum equations. During this stage, the presence of gas does not affect the evolution of the sloshing flow and it can be neglected for the entire evolution. Also the characteristic time scales of the hydrodynamic pressure are completely different from the structural one and no significant interactions between fluid and structure are expected. For this reason a fully rigid tank is assumed for the sloshing stage. On the physical assumptions presented, the equations system which describe the sloshing problem is:

$$\Delta \bar{\phi}(\mathbf{x}, \mathbf{t}) = 0 \quad \text{in } \Omega \quad (3.1)$$

$$\frac{\partial \bar{\phi}(\mathbf{x}, \mathbf{t})}{\partial n} = u^*(\mathbf{x}, t) \quad \text{on } \Omega_{solid} \quad (3.2)$$

$$\text{FreeSurf B.C.} \quad \text{on } \Omega_{fs}$$

The Laplace equation (3.1) for the velocity potential derives from the continuity equation for incompressible flow and from the hypothesis of irrotational flow ($\mathbf{u}(\mathbf{x}, \mathbf{t}) = \nabla \phi(\mathbf{x}, \mathbf{t})$, where $\mathbf{u}(\mathbf{x}, \mathbf{t})$ is the fluid velocity). The boundary conditions associated are, respectively, the impermeability condition (3.2) on the solid walls of the tank (Ω_{solid}), where $u^*(\mathbf{x}, t)$ is the solid boundary normal velocity, and the kinematic and dynamic boundary conditions on the free-surface (Ω_{fs}) that will be detailed in the following section.

Free surface boundary condition

The fully-nonlinear equations for the free surface have been adopted. The kinematic and dynamic equations state, respectively, that the fluid particles on to the free surface always remain on it and the pressure must be continuous at the free surface. In the case that the free surface is considered as a singled-valued function $y_p = y_p(x, t)$, the kinematic boundary condition is obtained as:

$$\frac{D(y_p - y)}{Dt} = 0$$

$$\frac{\partial y_p}{\partial t} = \frac{\partial \bar{\phi}}{\partial y} - \frac{\partial \bar{\phi}}{\partial x} \frac{\partial y_p}{\partial x} \quad (3.3)$$

while the dynamic one, which comes from Bernoulli equation, reads:

$$\bar{p} + \rho \frac{\partial \bar{\phi}}{\partial t} + \frac{\rho}{2} \nabla \bar{\phi} \cdot \nabla \bar{\phi} + \rho g y = p_0, \quad \text{with } \bar{p} = p_0 \quad (3.4)$$

The equations system (3.1), (3.2), (3.3) and (3.4) is valid in an Earth-fixed (inertial) reference frame. Otherwise, when the governing equations are expressed in a moving

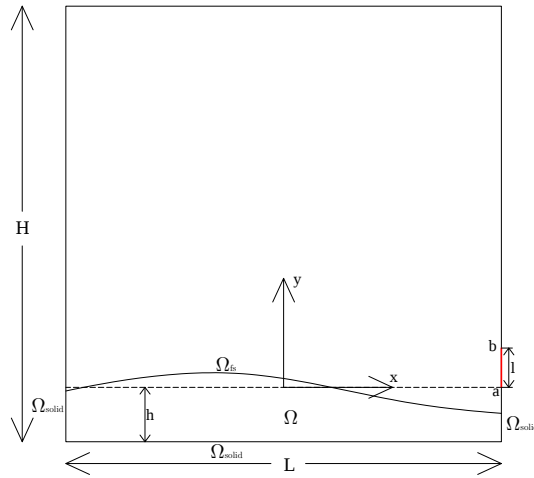


Figure 3.1. Tank model

coordinate system fixed to the tank, i.e. with the origin on the still water level in the middle of the tank (see fig.(3.1)), the motion of the tank must be taken in account. While the Laplace equation is invariant with respect to a change of reference, this is not for the Bernoulli equation, and how the time derivative of the velocity potential changes under the reference transform must be studied [11]. The time derivative of the velocity potential in a “fixed” point (x, y, z) in a non-inertial reference frame can be written in terms of the same time derivative in an inertial one, as follow:

$$\left. \frac{\partial \bar{\phi}}{\partial t} \right|_{\text{noninertial } Oxyz} = \lim_{\Delta t \rightarrow 0} \frac{\bar{\phi}(x, y, z, t + \Delta t) - \bar{\phi}(x, y, z, t)}{\Delta t} \quad (3.5)$$

$$\begin{aligned} \left. \frac{\partial \bar{\phi}}{\partial t} \right|_{\text{noninertial } Oxyz} &= \lim_{\Delta t \rightarrow 0} \frac{\bar{\phi}(x', y', z', t + \Delta t) + \mathbf{v}_p \cdot \nabla \bar{\phi} \Delta t - \bar{\phi}(x, y, z, t)}{\Delta t} \\ &= \left. \frac{\partial \bar{\phi}}{\partial t} \right|_{\text{inertial } Oxyz} + \mathbf{v}_p \cdot \nabla \bar{\phi} \end{aligned} \quad (3.6)$$

where \mathbf{v}_p is the velocity of the moving reference frame (i.e. considering the only sway motion of the tank $\mathbf{v}_p = [u_x, 0]$). The velocity potential for the relative velocity, observed when moving with the tank and always taking in account the only sway motion, can be expressed as:

$$\phi = \bar{\phi} - u_x x \quad (3.7)$$

where $\bar{\phi}$ is the absolute velocity potential, i.e. $\nabla \bar{\phi}$ is the velocities in the inertial reference system. The Bernoulli equation in a non-inertial reference system, with acceleration a_x , considering the relative velocities reads:

$$\rho \frac{\partial \phi}{\partial t} + x\rho a_x - \frac{\rho}{2}u_x^2 + \frac{\rho}{2}\nabla\phi \cdot \nabla\phi + \rho gy = 0 \quad (3.8)$$

Also the conditions on the solid boundary will be different, in particular along the vertical walls, the gradient of the velocity potential, in the normal direction, has to be set equal to zero as the tank speed in the moving reference frame is zero. The kinematic free-surface boundary condition, as well as the Laplace equation, will not change. For most of the time evolution of the sloshing stage, the free-surface can be considered as a single-value function $y_p(x, t)$ and the time evolution of the particles can be tracked in a semi Lagrangian way, following their motion only along the vertical direction. When the wave is close to the impact, in the case of both flip-through and air cavity entrainment, the single value approach for the description of the free surface evolution is not suitable anymore and a fully Lagrangian model is required. The kinematic and dynamic conditions can be written in the following formulation, which can be used both for the semi Lagrangian and the Lagrangian descriptions [32]:

$$\frac{\delta x_p}{\delta t} = \frac{\partial \phi}{\partial x} + (\underline{v} - \nabla\phi)^T \cdot \nabla x_p \quad \text{on } \Omega_{fs} \quad (3.9)$$

$$\frac{\delta y_p}{\delta t} = \frac{\partial \phi}{\partial y} + (\underline{v} - \nabla\phi)^T \cdot \nabla y_p \quad \text{on } \Omega_{fs} \quad (3.10)$$

$$\frac{\delta \phi}{\delta t} = -gy_p - \frac{1}{2}\nabla\phi \cdot \nabla\phi + \underline{v} \cdot \nabla\phi - xa_x + \frac{1}{2}u_x^2 \quad \text{on } \Omega_{fs} \quad (3.11)$$

where $\frac{\delta(\cdot)}{\delta t} = \frac{\partial(\cdot)}{\partial t} + \underline{v} \cdot \nabla(\cdot)$.

\underline{v} is the fluid(particle) velocity. We assume $\underline{v} = \{0, \delta\eta/\delta t\}$ for the semi Lagrangian tracking and $\underline{v} = \nabla\phi$ for the Lagrangian one.

Damping due to boundary layer flow

As already said, the viscous effects have been neglected in the mathematical model of the sloshing stage, here, a procedure to quantify their contribution will be discussed. The approach, following Faltinsen and Timokha [11], is based on Keulegan's theory. A two-dimensional linear flow outside the boundary layer is considered. Assuming no excitation of the tank, i.e. fixed tank, and concentrating on the velocity potential of a natural mode that is antisymmetric with respect to the y-axis (fig. 3.1), it is possible to express the total energy, i.e. sum of kinetic and potential energy, according to the linear potential flow theory as:

$$E = E_k + E_p = \frac{1}{4}\rho g A^2 l B \quad (3.12)$$

where ρ is the liquid density, A is the wave amplitude, l and B are the length and the breadth of the tank respectively. Assuming that the dissipation occurs on time scale longer than the natural period of of the examined mode and considering a laminar boundary-layer flow, it is possible to express the time rate of viscous dissipation over one period (assuming harmonic oscillations of the liquid with frequency sigma of the examined mode) per unit area of the plate, as

$$\langle \dot{E}_{vd} \rangle = -12\nu \sqrt{\sigma/2\nu} U_0^2(x) \quad (3.13)$$

Here ν is the kinematic viscosity of the liquid in the tank and U_0 is liquid horizontal velocity along the vertical walls. Using eq. (3.13) to estimate the viscous contributions from the bottom and vertical walls of the tank, the total rate of energy dissipation can be written as function of the total energy as:

$$\langle \dot{E} \rangle \equiv -2\alpha T^{-1} E \quad (3.14)$$

where the coefficient α is defined as

$$\alpha = \frac{\sqrt{\pi\nu T}}{B} \left[\left(\frac{B}{l} \right) \left(1 + \frac{.5kl - kh}{\sinh(kh) \cosh(kh)} \right) + 1 \right] \quad (3.15)$$

If $\nu = 1.01 \times 10^{-6} \text{ m}^2/\text{s}$ and $T = 1.6 \text{ sec}$ the coefficient α is 0.0309. This means that for each sloshing cycle there is a loss of energy due to the viscous boundary layer of about 3.8% of the total energy. To keep into account, in the mathematical model, the damping effect due to the boundary layer, the term $-2\alpha/T_n\phi$ [11] is added in the right-hand side of the dynamic boundary condition for the free surface (3.11).

3.3 Mathematical model for the hydroelastic stage

The hydroelastic stage concerns the coupling of the hydrodynamic and the structural problem, this implies that the mutual interaction between fluid and structure cannot be separated. As done for the sloshing stage, also for the structural problem some simplifying assumptions have been adopted. The dimensions of the elastic panel designed for the experiments ($L \times W \times T$ is $10 \times 9 \times 0.25$ cm), the constraints applied (double-clamp for the upper and lower sides and free to move for the lateral ones) as well as the hydrodynamic loads allow to consider the behaviour of the vertical centre-line of the panel as a beam. In particular, because the pressure loads are orthogonal to the structure and due to the small beam transverse displacement ($w \ll L$), the Euler theory can be considered a good approximation. In [22] it has been pointed out, from the dynamic analysis of the plate, that its behaviour is affected by small three-dimensional effects when it is subjected to impulsive load as the hammer hits. Even if the elastic plate has been hit in the middle, beside the first bending mode, which mainly characterizes the structural response, also the first two lower torsional modes appear in the plate response. Because the hydrodynamic load acts along the whole breadth of the plate in an almost uniform way, no three-dimensional effects are expected. Furthermore, the analysis of the natural frequencies of the plate shows a quite good agreement with the natural frequencies estimated with the Euler beam theory, at least for the first two bending modes (as discussed in the experimental setup section). This supports the use of an Euler beam model for the plate. A modal expansion in terms of eigenfunctions has been used in the following for the representation of the beam deflection $w(y, t)$. For the estimation of the hydrodynamic loads a proper model for the fluid problem is required. This stage can be characterized by a single or two-phase problem depending on the impact scenario. In both cases the viscous effects for the hydrodynamic problem are negligible with respect to the inertial ones and the problem can be modelled as already done for the sloshing stage. Differently from the flip-through case, where the fluid problem can be considered as a single phase flow for the entire evolution of the phenomena (sloshing + hydroelastic stages), in the case of impact with gas entrainment the presence of the gas phase cannot be excluded. In particular, the presence of the gas is important since the formation of the cavity and subsequently for the impact evolution. During the initial stage, gas leakage phenomena occur, modifying the following evolution of the cavity once it is completely closed against the wall. During the initial phase, before the cavity closure, the hypothesis of incompressible flow can be extended also to the gaseous phase, as it is expected a limited effect of the gas flow on the liquid evolution. After the cavity closure compressible effects must be taken into account for the gas inside the cavity.

The mathematical formulation of the simplified hydroelastic problem reads:

$$p(y, t, w) = M_B \frac{\partial^2 w(y, t)}{\partial t^2} + EI \frac{\partial^4 w(y, t)}{\partial y^4}, \quad a \leq y \leq b \quad (3.16)$$

$$w(y, t) = 0, \quad \forall t, \quad y = a, b \quad (3.17)$$

$$\frac{\partial w(y, t)}{\partial y} = 0, \quad \forall t, \quad y = a, b \quad (3.18)$$

$$\Delta \phi = 0, \quad \text{in } \Omega \quad (3.19)$$

$$\frac{\partial \phi}{\partial n} = 0, \quad \text{on } \Omega_{rigid} \quad (3.20)$$

$$\frac{\partial \phi}{\partial n} = \dot{w}(y, t) \cdot \vec{n}, \quad \text{on } \Omega_{elastic} \quad (3.21)$$

$$\frac{\partial \underline{X}_p}{\partial t} = \nabla \phi + (\underline{v} - \nabla \phi)^T \cdot \nabla \underline{X}_p \quad \text{on } \Omega_{fs} \quad (3.22)$$

$$\frac{\delta \phi}{\delta t} = -gy_p - \frac{1}{2} \nabla \phi \cdot \nabla \phi + \underline{v} \cdot \nabla \phi + \frac{p_0 - p(t)}{\rho} - xa_x + \frac{1}{2} u_x^2 \quad \text{on } \Omega_{fs} \quad (3.23)$$

Eq. 3.17 is the beam equation with $a \leq y \leq b$ the beam position on the right tank wall; the rest of this and the other walls are assumed rigid. Here M_B is the mass of the beam per unit length, E is the Young modulus and I is the area moment of inertia of the beam cross-section. Equations 3.17 and 3.18 represent the beam boundary conditions reproducing clamped-end constrains at the beam ends $y=a$ and b . Equations ??-?? are the Boundary Value Problem (BVP) for the velocity potential in the liquid domain written in the tank fixed reference frame. In order, we have the governing equation, impermeability condition along the rigid and the elastic (beam) walls and the kinematic and dynamic free-surface boundary conditions. Here $\Omega_{elastic}$ refers to the wetted part of the beam, i.e. $a \leq y \leq \min(b, h^*(t))$, where $h^*(t)$ is the instantaneous wave elevation on the right wall.

Eqs. (3.16)-(3.23) represent a general formulation of the hydroelastic problem, with coupling between fluid and structural evolutions given by the hydrodynamic pressure term in the beam equation. They can be used in the case of a flip-through impact only. In fact the additional condition, that has to be added is the Bernoulli equation (3.23), where, for the dynamic boundary condition on the free-surface, is required that the pressure is continuous through it, i.e. $p(t) = p_0$.

Otherwise, in the case of impact with gas entrainment, a mathematical model for the gaseous phase must be added. During the first stage, when the cavity is not yet closed against the wall, the hypothesis of incompressible and irrotational flow can be adopted also for the gaseous phase. At the interface between the two phases the pressure and the normal component of the velocity are required to be continuous.

Differently, when the cavity is closed, the gas compressibility causes an oscillatory motion characterized by the natural frequency which depends on the gas-cavity properties. The inner pressure oscillates with the same frequency. In the dynamic boundary condition at the free surface, the dynamic pressure must be set equal to the pressure inside the gas cavity. In the following a simplified mathematical model, which describe the behaviour of the cavity is presented.

3.3.1 “Lumped” model for the gas-cavity

The proposed model is valid after the closure of the gas-cavity against the wall and it does not take into account leakage phenomena which are present just before the closure of the cavity. For the sloshing model, the simplifying hypotheses adopted are still valid, the liquid can be considered even now as inviscid and irrotational and also the hypothesis of incompressibility holds because the time scales of the pressure oscillations are not such to induce compressibility effects. The pressure inside the gas cavity is assumed to be spatially uniform and adiabatic or isothermal process for the gas can be considered. The fact that thermal conductivity, as well as shear viscosity and acoustic wave radiation are not taken into account means that no damping sources are present in the model. Two additional unknowns are added to the problem: the pressure and the gas density and two more equations are required. The first one establishes a relationship between pressure and density in the case of adiabatic or isothermal transformation:

$$\bar{p}_g(t) = p_{0g} \left(\frac{\rho_g}{\rho_{0g}} \right)^k \quad (3.24)$$

where $\bar{p}_g(t)$ and ρ_g are the instantaneous pressure and density inside the cavity, p_{0g} and ρ_{0g} are the pressure and the density at the moment of the cavity closure and $k = 1$ or $k = 1.4$ are respectively the coefficients for an adiabatic or isothermal transformation. The initial values for pressure and density can be set equal to the ullage values, i.e. $p_{0g} = p_0$ and $\rho_{0g} = \rho_0$, or they can be estimated by taking into account the leakage phenomena present just before the closure of the cavity. The latter requires the solution of the gas problem at least during the final part of the sloshing stage.

The second equation is the mass conservation for the gas cavity, which is expressed as $\Omega_{g0}\rho_{0g} = \Omega_g(t)\rho_g$. With this, it is possible to write the pressure as function of the cavity volume $\Omega_g(t)$. While Ω_{g0} is the initial volume of the cavity at the time of the closure. Combining the last link with eq. (3.24), we have

$$\bar{p}_g(t) = p_{0g} \left(\frac{\Omega_{g0}}{\Omega_g(t)} \right)^k \quad (3.25)$$

It is not easy to identify the transformation that better characterizes the relationship between pressure and density. As shown in [1], through a linear steady state thermodynamical analysis of the cavity problem, the adiabatic transformation seems to be the most appropriate.

3.3.2 Structural sub-problem

The deflection $w(y, t)$ can be expressed in terms of the eigenfunctions $\psi_k(y)$ of the structural differential operator $L = EI\partial^4(\bullet)/\partial y^4$:

$$w(y, t) = \sum_{k=1}^{\infty} w_k(t)\psi_k(y) \quad (3.26)$$

The expression of the eigenfunctions and the relative eigenvalues are obtained by solving the differential problem $L[\psi_k(y)] = \lambda_k^4\psi_k(y)$ with the boundary conditions (3.17-3.18). A possible solution for the eigenfunctions is:

$$\psi_k(y) = A_k \sin(\lambda_k y) + B_k \cos(\lambda_k y) + C_k \cosh(\lambda_k y) + D_k \sinh(\lambda_k y) \quad (3.27)$$

With the assignment of the boundary conditions it is possible to evaluate the constants A_k, B_k, C_k, D_k , which are determined but for a multiplicative constant:

$$A_k = -B_k \frac{\cos(\lambda(a-b)) - \cosh(\lambda(a-b))}{\sin(\lambda(a-b)) - \sinh(\lambda(a-b))}$$

$$B_k = -1$$

$$C_k = -A_k$$

$$D_k = -B_k$$

and a compatibility condition which allows for the calculation of the eigenvalues λ_k

$$\cos(\lambda_k(a-b)) \cosh(\lambda_k(a-b)) = 1$$

Because the structural operator L is self-adjoint, both the eigenfunctions and the eigenvalues are real and the eigenfunctions are orthogonal. From the physical point of view, the eigenfunctions $\psi_k(y)$ correspond to the natural dry modes of vibration of the structure associated to the natural angular frequencies $\omega_k = \sqrt{\frac{\lambda_k^4}{M_B}}$.

3.4 Hybrid hydroelastic model

In this section, a semi-analytical hybrid hydroelastic model is presented, where the fluid dynamic problem is not solved numerically but via a mix of a mathematical model for the added mass and experimental results for the hydrodynamic loads.

The proposed hybrid model is based on the assumptions of a weak interaction between excitation and response and on the absence of gas cavity during the impact, so that the forcing term $p(y, t, w)$ can be decomposed as the following linear superposition:

$$p(y, t, w) = p_r(y, t) + p_v(y, t, w) \quad (3.28)$$

The first contribution $p_r(y, t)$ is the pressure field induced by a wave impact event on the fully rigid wall. It is a fully nonlinear load which depends on the nonlinear kinematics of the wave impact and needs to be modeled as such. In the present case it is modelled using the experimental value of the pressure measured during the experimental activities on a fully rigid tank. During these experiments the same filling condition and the tank motion used in the case of a deformable panel, have been reproduced, hence the features of the wave interacting with the wall are the same.

The second contribution, $p_v(y, t, w)$ is the vibrational pressure, which solves the hydroelastic problem of the vibrating beam around a rest state. Using the potential flow assumption for an incompressible fluid with density ρ_w , the pressure forcing term $p_v = -\rho_w \frac{\partial \phi_v}{\partial t}$ is given by the linearized Bernoulli equation. The vibrational potential function is instantaneously determined as the solution of the following boundary value problem:

$$\begin{aligned} \Delta \phi_v &= 0 && \text{in the water fluid} \\ \frac{\partial \phi_v}{\partial n} &= 0 && \text{on the rigid walls of the tank} \\ \frac{\partial \phi_v}{\partial n} &= \frac{\partial w}{\partial t} && a \leq y < \min(b, h(t)) \\ \phi_v &= 0 && y = h(t) \end{aligned} \quad (3.29)$$

In this case the vibrational pressure is assumed to be independent from the local shape of the free surface and from the local kinematics of the wave impact (which is already taken into account in the term p_r). However, p_v accounts for the instantaneous wetted length $h(t)$ of the vertical beam, influenced by the evolution of the impact event. Because of the large value of the lowest wetted natural vibration frequency of the beam (with respect to the typical frequency range when gravity affects the free surface behavior), a high-frequency approximation is assumed for the combined free surface boundary condition. This approximation simplifies greatly the problem and is also consistent with the fact that, during the water impact with the tank and subsequent water rise up, the liquid velocity at the free-surface is expected to be almost vertical near the wall. Its validity can be verified through the comparison with the experiments. Like p_r , also the wetted length $h(t)$ of the beam depends on the evolution of the wave, hence it cannot be predicted numerically and it has been measured from the experimental images. Recalling eq. (3.16), the hydroelastic problem reads:

$$M_B \ddot{w}_k(t) \psi_k(y) + EI \lambda_k^4 w_k(t) \psi_k(y) = -\rho_w \frac{\partial \phi_v}{\partial t} + p_r(y, t) \quad (3.30)$$

where the beam deflection is expressed in terms of the eigenfunctions, here the repeated index k means summation, and the vibrational pressure through the linearized Bernoulli equation. The velocity potential associated to the k -th natural mode of the beam is defined as $\dot{w}_k \phi_k(y)$. By replacing the last definition in eq. (3.30) and projecting on the generic m -th mode ψ_m

$$(M_{mm} + A_{mm}) \ddot{w}_m(t) + \sum_{k \neq m} A_{mk} \ddot{w}_k(t) + K_{mm} w_m(t) = p_{r_m}(t) \quad (3.31)$$

where

$$\begin{aligned} M_{mm} &= M_B \int_l \phi_m(y) \phi_m(y) dy \\ A_{mm} &= \rho_w \int_l \psi_m(y) \phi_m(y) dy \\ A_{km} &= \rho_w \int_l \psi_k(y) \phi_m(y) dy, \quad k \neq m \\ K_{mm} &= EI \lambda_m^4 \int_l \phi_m(y) \phi_m(y) dy \end{aligned}$$

are, respectively, the mass, the hydrodynamic added mass and the stiffness matrices and $p_{r_m}(t)$ is the generalized hydrodynamic pressure. Due to the orthogonality property of the eigenfunctions the mass and stiffness matrices are diagonal, while the added mass matrix is full. The wetted natural frequencies of the beam can be easily evaluated from the homogeneous solution of eq. (3.31), in particular considering only the first natural mode ($m = k = 1$):

$$\omega_{1w} = \sqrt{\frac{K_{11}}{M_{11} + A_{11}}} = \omega_1 \sqrt{\frac{M_{11}}{M_{11} + A_{11}}} \quad (3.32)$$

Note that the wetted natural frequency is equal to the dry one ω_1 when $A_{11} = 0$. The added mass matrix requires the solution of the boundary value problem (3.29), which can be rewritten, introducing the eigenfunction expansion for the beam deformation, as follows:

$$\begin{aligned} \Delta \phi_v &= 0 && \text{in the water domain} \\ \phi_v &= 0 && y = h(t) \\ \frac{\partial \phi_v}{\partial n} &= \begin{cases} \psi(y, t) & a \leq y \leq a + l \\ 0 & \text{otherwise} \end{cases} \end{aligned} \quad (3.33)$$

Numerical solution

Eq. (3.31) is integrated in time by using a fourth-order Runge-Kutta method. At each time step, the forcing pressure $p_r(y, t)$ is prescribed by using the experimental distribution

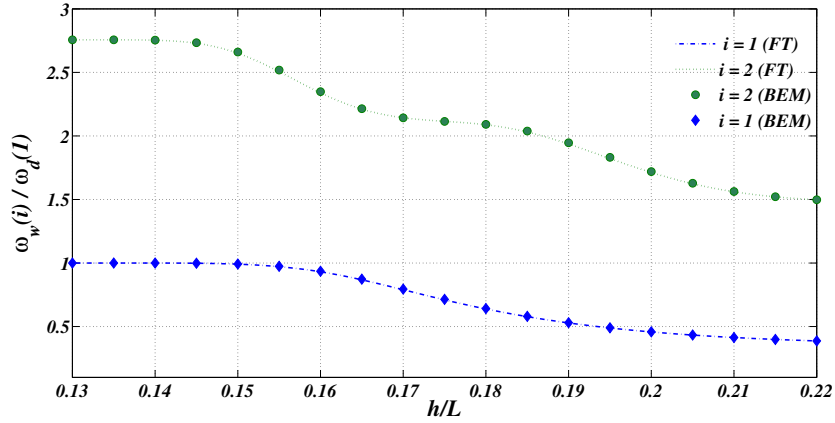


Figure 3.2. Variation of the first (blue) and second (green) wet natural frequency as function of the filling depth. Symbols are obtained from the HOBEM, while lines come from the Fourier Transform method.

measured through the pressure transducers distributed along a rigid wall located like the beam in the fully rigid experiments. The vibration potential ϕ_v comes from the numerical solution of the boundary value problem (3.33). A possible solution was proposed by Faltinsen and Timokha [11] with an analytical solution assuming a Fourier expansion for ψ and ϕ_v but its validity is limited to the fully wet beam case. Since the dynamics of the wave impact phenomena imposes a rapid change of the beam conditions from completely dry to fully wet, a numerical solution is used to solve the vibrational problem associated to each mode. The vibrational potential is assumed of the form

$$\phi_v = \sum_n A_n \sin \left[(2n+1)\pi \frac{y}{2h} \right] \cosh \left[(2n+1)\pi \frac{x+L}{2h} \right] \quad (3.34)$$

which satisfies the Laplace equation and the boundary conditions on the free surface, on the bottom and on the wall opposite to the impact of problem (3.33). This corresponds to using the Fourier Transform method, thus a linear system is solved for the unknown coefficients A_n which forces the fulfillment of the boundary condition on the tank side with the deformable beam. At each time step t , $h(t)$ is measured from the corresponding experimental image.

The present solution of the potential has been validated against the results of a Higher Order Boundary Element Method (HOBEM) used to solve problem (3.33). Figure 3.2 shows an estimation of the first two natural frequencies as function of the wetted length of the beam. Problem (3.33) is solved considering different wetted lengths, from the dry to a fully wet condition for the estimation of the added mass contribution. The lowest dry natural frequency $\omega_d(1) = 1575 \text{ Hz}$ has been used to make the data dimensionless. The symbols represent the value of the natural frequencies obtained by the solution of the boundary value problem (3.33) through the HOBEM method, while the lines stand for the solution obtained with the shape function (3.34). The good agreement between the two solutions confirms the trustworthiness of the second approach (shape function), which is more advisable because of its higher efficiency.

In figure 3.3 the comparison of the model with the experimental results is shown. The purple lines represent the temporal evolution of the strain recorded in the middle

of the structure, the black ones are the results obtained via the model while the dashed green line (when present) is the value of the instantaneous wave height at wall measured through the fast-cam image. In the top-left plot it is shown the comparison assuming the structural problem undamped and the instantaneous wave height changing in time according to the measured values. On the right the structural damping, which exponential decay coefficient has been estimated with free-decay test in dry condition, was employed. From the comparison it is quite evident how only the structural damping gives an underestimation of the real damping, which characterizes the hydroelastic phenomenon. In terms of natural vibration frequency, the instantaneous beam wetted length, and hence the added mass effects, gives a quite good approximation of the frequency up to ≈ 5 ms, after such time, considering the further increase of the wave elevation gives a natural frequency lower than the actual one (left and right bottom panels in fig. 3.3). In the bottom-left plot, the exponential decay coefficient has been assumed depending on the instantaneous wetted length of the beam, according to the law reported in section (2.1.2) (see figure (2.5)). The comparison shows a better behaviour of the model. Finally, in the last plot (bottom-right), the instantaneous wave height has been restricted to ≈ 0.22 cm, which corresponds to a fully wet condition for the flexible structure. This assumption allows to reproduce the correct vibration frequency for a longer time (up to ≈ 15 ms). Anyway, at a later time the period of oscillation of the measured signal is larger than the simulated one, pointing out the continuous, even if slow, growth of the added mass effects. The overestimation of the added mass effects in the model can be justified with the fact that a flat free-surface condition with a water depth equal to the instantaneous wave height at the wall is used, whereas, it seems that the more the wave height grows ($h(t) \geq 0.22$ cm) the more is the influence of the free-surface shape (for the added mass estimation).

In terms of oscillations amplitude (with reference to the last plot, bottom-right), the model is not able to reproduce the maxima and minima values recorded in the experiments, especially in the *fully hydroelastic* stage and this can be ascribed to a stronger interaction between fluid and structure than the modelled one. Later, i.e. for $t \geq 6 - 7$ ms, the hydroelastic evolution resembles the free-vibration behaviour with an almost constant added mass.

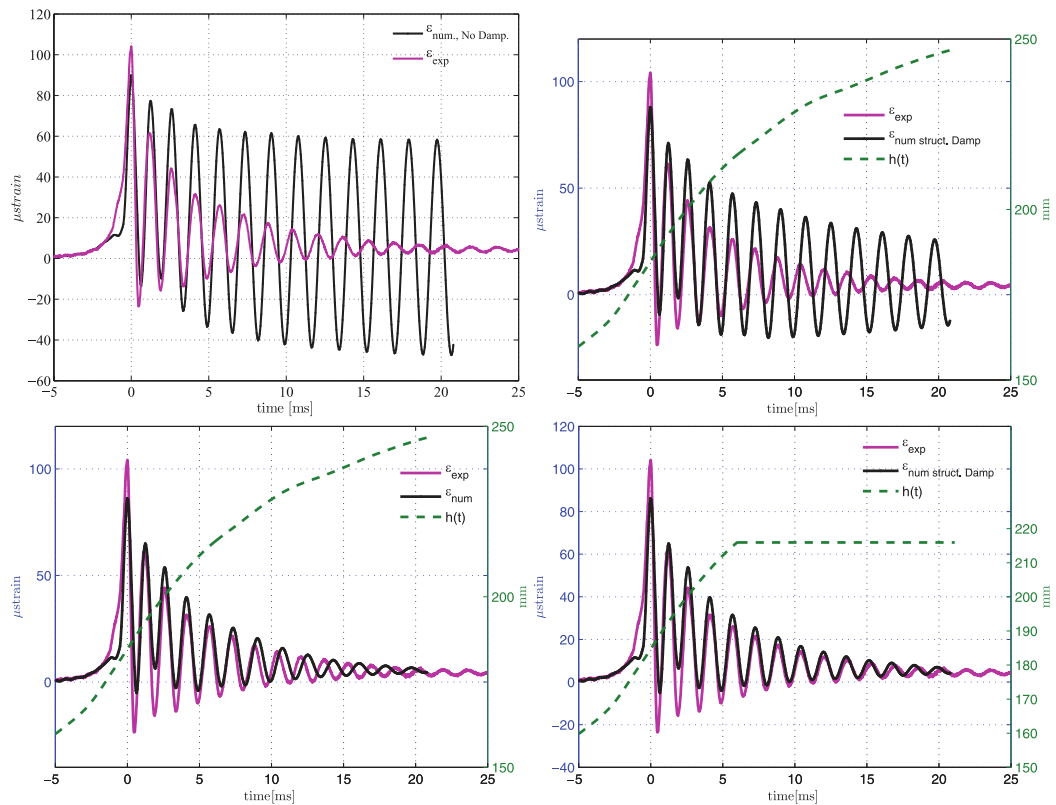


Figure 3.3. Elastic test. Comparison between the numerical prediction (purple line) and experiment (black line). If present the dashed green line shows the instantaneous wave elevation at wall. In the top-left panel, no damping term is used in the model. In the bottom-left panel a constant structural damping is added to the model. On the top-right panel, a time varying damping coefficient is used. In the bottom-right panel, the time history of the wave height has been restricted until to 0.22 cm.

3.4.1 Gas cavity analytical model

With the intent of deriving an analytical model also for the hydroelastic problem when a gas cavity is present during the impact, in this section the preliminary study is presented concerning the problem considering the structure as rigid instead of elastic. The study starts from the analytical model proposed by Faltinsen and Timokha [11] and in the successive improvement in [2]. The model in [11], concerns the problem of a cavity entrapped by a wave against the roof of a sloshing tank. It is proposed both a linearized estimation of the cavity natural frequency and also the non-linear dynamic system, which describes the problem. In [2] the linearized problem has been generalized also to a breaking wave, which entraps gas cavity on the vertical wall. The influence of the free surface shape has been also considered.

Here, the non linear model for a cavity entrapped against a vertical wall is taken into account. This is done because the non-linearity plays an important role if the fluid structure interaction is considered and also because in case of low ullage pressure the experiments show a strong non-linear behaviour of the gas cavity both in rigid and elastic case.

Differently from the hybrid analytical model presented in the previous section (concerning the flip-through impact) where the forcing hydrodynamic loads have been estimated from the rigid test, in this case, the sloshing stage has been neglected at all and the effects of the wave impact, i.e. impulsive hydrodynamic load, has been reproduced using the same approach as done for the water entry problem.

The physical assumptions adopted here are the same as those considered in the cited works and discussed in section (3.3.1). In figure (3.4) the simplified physical problem with the associated boundary conditions is shown. A thin gas cavity is located in $C \leq y \leq B$. The gas is considered compressible and characterized by spatially homogeneous properties. For the water flow it has been neglected both viscosity and compressibility effects, the fluid has also been considered irrotational and this allows to use the potential flow theory. The domain is assumed infinite in the positive x direction. The frequency of the cavity can be considered high so to avoid the gravity effect and then the flat free surface condition with constant null value of the velocity potential can be adopted ($\phi = 0$). On the rigid wall the impermeability condition is imposed. In order to satisfy the impermeability condition on the bottom of the tank, a mirroring of the physical domain with respect to the axis $y=0$ is used. For the estimation of the velocity potential, the idea is to collocate a vortex distribution along the vertical wall, with the exception of the cavity area, such as to satisfy the boundary conditions. This approach is similar to the one already proposed by Newman in the study of the lifting surface problem [27]. To transform the domain in a simpler one for which the analytical solution of the boundary value problem can be easily derived, the Schwarz-Christoffel mapping is used. In particular the transformation (3.35), allows to transform a semi-infinite rectangle in a infinite half plane where all the physical boundaries lie on the axis $\eta = 0$. Figure (3.5) shows the transformed domain with the new boundary conditions. The half plane $\xi > 0$ represents the mirrored domain.

$$z = M \cosh^{-1}(\xi) + N \quad (3.35)$$

Always through eq. (3.35) all the boundary conditions are modified for the new domain

following the expressions:

$$\tilde{u} = \frac{-2hv}{\pi\sqrt{1-\xi^2}}, \quad \tilde{v} = \frac{2hu}{\pi\sqrt{1-\xi^2}}, \quad |\xi| < 1 \quad (3.36)$$

$$\tilde{u} = \frac{2hu}{\pi\sqrt{\xi^2-1}}, \quad \tilde{v} = \frac{2hv}{\pi\sqrt{\xi^2-1}}, \quad |\xi| > 1 \quad (3.37)$$

where \tilde{u}, \tilde{v} are the velocity components in the transformed plane and u, v are the components in the physical plane. h is the water depth and in the sketch is represented by the length of the segment \overline{AD} . The velocity components in the transformed plane, when $\eta \rightarrow 0^+$, can be expressed as function of the vortex density $\gamma(\xi)$ as:

$$\tilde{u}(\xi) = -\frac{1}{2}\gamma(\xi) \quad (3.38)$$

$$\tilde{v}(\xi) = -\frac{1}{2\pi} \int_{-a}^a \frac{\gamma(x')}{x' - \xi} dx' \quad (3.39)$$

where the integral \int means that the Cauchy Principal Value method has to be used for the evaluation of the integral. A solution for eq. (3.39), considering the function $\gamma(\xi)$ unbounded at both extrema, is:

$$\gamma(\xi) = \frac{2}{\pi} \frac{1}{\sqrt{a^2 - \xi^2}} \left[\int_{-a}^a \frac{\sqrt{a^2 - x'^2}}{x' - \xi} \tilde{v}(x') dx' + C \right] \quad (3.40)$$

where the constant C can be assumed equal to zero because of the symmetry of the problem about the origin d . In the interval $c \leq |\xi| \leq b$ we are looking for the homogeneous solution of (3.40), (i.e. $\gamma(\xi) = 0$), for instance, considering the interval $-b \leq \xi \leq -c$ it is possible to

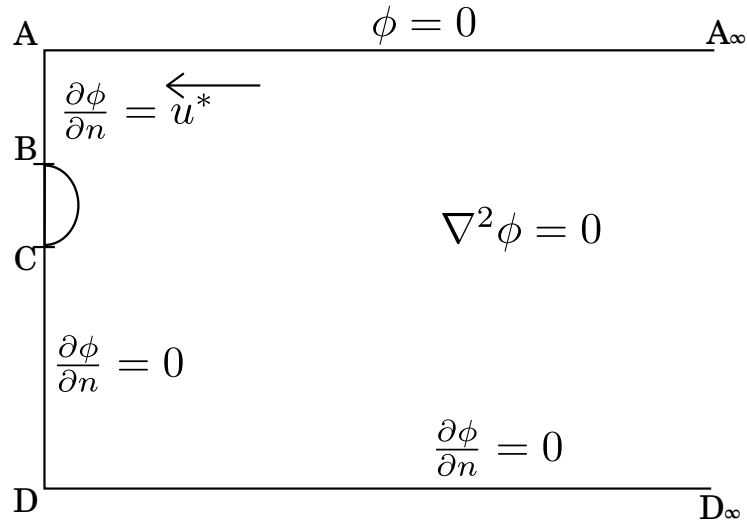


Figure 3.4. Sketch of the proposed mathematical model for the gas cavity problem. $\overline{AA_\infty}$ free surface, \overline{AD} tank vertical wall, $\overline{DD_\infty}$ tank bottom, \overline{BC} cavity size. The boundary conditions and the governing equation are also reported.

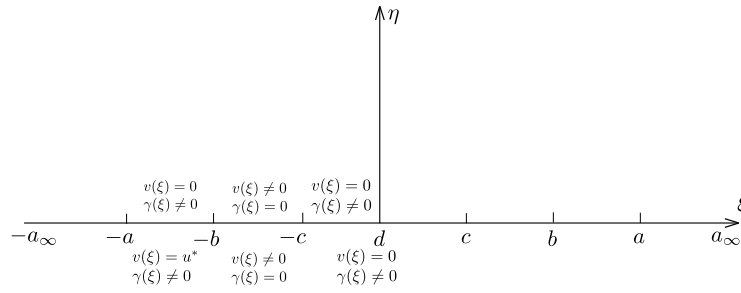


Figure 3.5. In the half plane $\eta > 0$ we have the transformed boundary conditions for the free oscillation problem. For $\eta < 0$ we find the boundary conditions for the forced problem.

rewrite the integral equation as follow:

$$0 = \int_{-b}^{-c} \frac{\sqrt{a^2 - x'^2}}{x' - \xi} \tilde{v}(x') dx' + \int_c^b \frac{\sqrt{a^2 - x'^2}}{x' - \xi} \tilde{v}(x') dx' \quad (3.41)$$

By using the symmetry property for the velocity function $\tilde{v}(\xi)$, which requires it to be an even function $\tilde{v}(\xi) = \tilde{v}(-\xi)$, the integral may be rewritten as:

$$0 = \int_{-b}^{-c} \frac{\sqrt{a^2 - x'^2}}{x'^2 - \xi^2} \tilde{v}(x') dx' \quad (3.42)$$

by defining $\frac{\sqrt{a^2 - x'^2} \tilde{v}(x')}{x'} = g(x')$ and operating the following change of variable $-\sqrt{\eta} = x'$, then we get an integral equation (eq. 3.43) for which the solution (eq. 3.44) is known:

$$0 = \int_{c^2}^{b^2} \frac{g(\eta)}{\eta - y} d\eta \quad (3.43)$$

$$g(y) = \frac{1}{\pi^2} \frac{D(t)}{\sqrt{(y - c^2)(b^2 - y)}} \quad (3.44)$$

and then, the velocity distribution along the cavity is

$$v(\xi) = \frac{1}{\pi^2} \frac{D(t)\xi}{\sqrt{a^2 - \xi^2} \sqrt{(\xi^2 - c^2)(b^2 - \xi^2)}} \quad (3.45)$$

The same steps are valid for the interval $c \leq \xi \leq b$ and give the same result. Once the vertical velocity is known, it is possible to estimate the vorticity distribution $\gamma(\xi)$ along the rigid wall by the (3.40)

$$\begin{cases} \gamma(\xi) = \frac{-2D\xi}{\sqrt{a^2 - \xi^2} \sqrt{(\xi^2 - c^2)(\xi^2 - b^2)}} & -a \leq \xi \leq -b \\ \gamma(\xi) = \frac{2D\xi}{\sqrt{a^2 - \xi^2} \sqrt{(-\xi^2 + c^2)(-\xi^2 + b^2)}} & -c \leq \xi \leq c \\ \gamma(\xi) = \frac{-2D\xi}{\sqrt{a^2 - \xi^2} \sqrt{(\xi^2 - c^2)(\xi^2 - b^2)}} & b \leq \xi \leq a \end{cases} \quad (3.46)$$

From the expression of the horizontal velocity (3.38), it is possible, by integration and by using the boundary condition on the free surface ($\phi(-a) = 0$), to estimate the value of the

velocity potential on the left boundary of the cavity:

$$\int_{-a}^{-b} \frac{\partial \phi}{\partial \xi} d\xi = \int_{-a}^{-b} -\frac{1}{2} \gamma(\xi) d\xi = \phi(-b) - \phi(-a) = \phi(-b) = \frac{-D(t)K \left[\sqrt{\frac{1-(b/a)^2}{1-(c/a)^2}} \right]}{\pi^2 \sqrt{a^2 - c^2}} \quad (3.47)$$

where $K(k)$ is the complete elliptic integral of the first kind.

With the assumptions that the non linear term as well as the hydrostatic term can be neglected in the Bernoulli equation, the dynamic pressure on the cavity side, and then also inside, may be expressed as the time derivative of the velocity potential

$$p_D = -\rho_l \frac{\partial \phi}{\partial t} = \rho_l \frac{-\dot{D}(t)K \left[\sqrt{\frac{1-(b/a)^2}{1-(c/a)^2}} \right]}{\pi^2 \sqrt{a^2 - c^2}} \quad (3.48)$$

The pressure inside the cavity is expressed as the sum of the static pressure p_0 and the dynamic pressure p_D . If the gas is considered to be compressed with an adiabatic transformation then the relation between pressure and density is:

$$p_{gas}/p_0 = (\rho_{gas}/\rho_0)^\gamma \rightarrow \rho_l \frac{-\dot{D}(t)K \left[\sqrt{\frac{1-(b/a)^2}{1-(c/a)^2}} \right]}{\pi^2 \sqrt{a^2 - c^2}} = (\rho_{gas}/\rho_0)^\gamma - p_0 \quad (3.49)$$

where γ is the ratio of specific heats. Because in this model the formation of the cavity is not considered and then leakage phenomena are neglected, the static values of pressure and density are the ullage one. The hypothesis about leakage phenomena allows to write the mass conservation equation for the gas cavity as $\Omega_{gas}\rho_{gas} = \Omega_0\rho_0$ and it can be used in eq. (3.49) to express the pressure as function of the volume for which its time rate of change can be estimated by integrating, along the cavity, the vertical component of velocity $v(\xi)$:

$$\begin{aligned} \dot{\Omega} &= - \int_{-b}^{-c} v(\xi) d\xi = - \frac{D(t)}{\pi^2} \int_{-b}^{-c} \frac{\xi}{\sqrt{a^2 - \xi^2} \sqrt{(\xi^2 - c^2)(b^2 - \xi^2)}} d\xi \\ &= - \frac{D(t)}{\pi^2 \sqrt{a^2 - c^2}} K \left[\sqrt{\frac{1-(b/c)^2}{1-(a/c)^2}} \right] \end{aligned} \quad (3.50)$$

By defining $D_1 = \frac{-D(t)K \left[\sqrt{\frac{1-(b/a)^2}{1-(c/a)^2}} \right]}{\pi^2 \sqrt{a^2 - c^2}}$ and by taking the time derivative of eq. (3.50) and then by substituting the value of \dot{D}_1 from (3.49), a non linear second order equation is obtained:

$$\ddot{\Omega}(t) = -\frac{p_0}{\rho_l} \left(1 - \left(\frac{\Omega_0}{\Omega(t)} \right)^\gamma \right) \frac{K \left[\sqrt{\frac{1-(b/c)^2}{1-(a/c)^2}} \right]}{K \left[\sqrt{\frac{1-(b/a)^2}{1-(c/a)^2}} \right]} \quad (3.51)$$

Through the linearization of the term $\Omega^{-\gamma}$ it is possible to calculate a linear estimation of the cavity natural frequency

$$\ddot{\Omega}(t) = -\frac{p_0\gamma}{\rho_l\Omega_0} \bar{K}\Omega(t) + \frac{p_0\gamma}{\rho_l} \bar{K} \quad (3.52)$$

where \bar{K} is the ratio between the two elliptic integrals. The system looks now as a classical mass-spring system with natural frequency equal to:

$$\sigma_n^2 = \frac{p_0\gamma}{\rho_l\Omega_0} \bar{K} \quad (3.53)$$

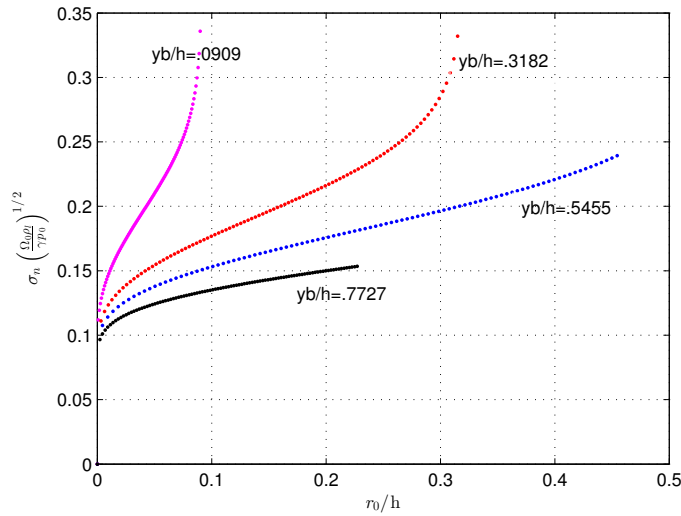


Figure 3.6. Non dimensional natural frequencies of the cavity as function of the initial cavity radius at different position of the cavity center(y_b).

Figure 3.6 shows the non dimensional natural frequency as function of the cavity radius and position of the cavity center with respect to the free surface. The natural frequency approaches to zero when the radius goes to zero too. When the cavity radius is such that the upper part of the cavity is close to the free surface, the frequency tends to infinity while if the lower part is close to the bottom of the tank the frequency approaches to a finite value. It is also possible to observe as the natural frequency, for a fixed initial radius r_0 , is inversely proportional to the distance from the free surface. The comparison with the analytical model by Topliss shows a quite different behavior of the natural frequency. The proposed model shows an underestimation of the natural frequency if compared with the Topliss's model. An additional comparison with the results of Topliss's model and with experiments is shown in table (3.1). The experimental activity concerns the entrainment of cylindrical air cavity during a wave impact against a vertical wall. Differently from the Topliss model, which predicts the natural frequency with a good accuracy in case of large air cavity, the proposed model seems to be more accurate in the case of small cavity radius. In any case, some differences with respect to the experimental results, for all the data, are shown. This could be ascribed to the different hypotheses made in the analytical models with respect to the experimental tests.

Equation (3.51) can be solved numerically with the suitable initial conditions. The proposed models are used in the following to evaluate the cavity natural oscillation frequency starting from initial conditions from the experimental activity. In particular, as initial time ($t_0 = 0$) the instant for which, the pressure transducer closer to the gas cavity recorded its maximum value has been considered. In this condition the time rate of change of the cavity volume is equal to zero, and then $\dot{\Omega}(0) = 0$, while the cavity volume $\Omega(0)$ can be estimated from the fast cam image. In fact, once the volume and the pressure at $t = 0$ are known, from eq. (3.49) combined with the continuity equation it is possible to estimate the equilibrium volume of the cavity $\Omega_0 = \Omega(0) \left(\frac{p(0)}{p_0} + 1 \right)^{1/\gamma}$.

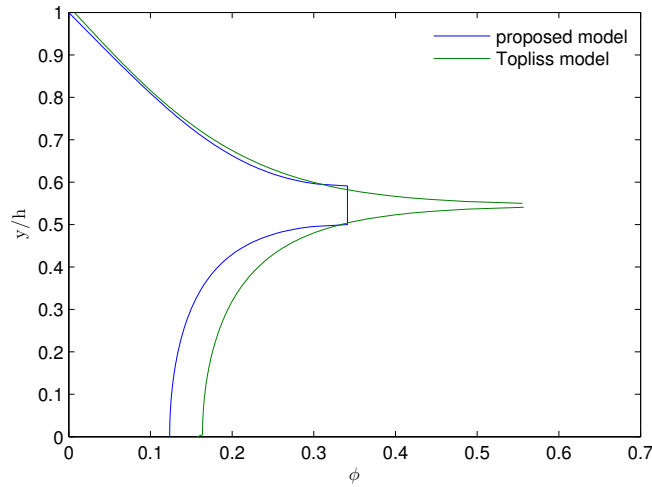


Figure 3.7. Comparison of the velocity potential along the vertical wall calculated with the proposed analytical model and with the Topliss model. The center of the cavity is at $y/h = 0.5455$

A different way to assign the initial condition to the dynamic problem is to consider the pressure impulse. Integrating in time eq. (3.48) from t_0 to $t_1 = 0$ and using the condition $D_1(0) = 0$ we have

$$\int_{t_0}^{t_1} p_D dt = \rho_L D_1(t_0) = -\rho_L \frac{\dot{\Omega}(t_0)}{\bar{K}} \quad (3.54)$$

while the initial condition for the cavity volume is $\Omega(t_0) = \Omega_0$.

In figures (3.9 - 3.14) the liquid and cavity configurations chosen for the free evolution problem with respect to the real case are shown (top image). The blue line represents the flat free surface, the water depth has been chosen as the wave height at the moment of the impact when the pressure reaches its maximum value. During the whole evolution of the impact the water depth is considered constant. This implies that also the distance between the cavity center and the free surface is constant. The red line shows the gas cavity form which has been assumed semi-circular. The yellow markers show the position of the five pressure transducers along the vertical wall. The lower panels show the comparison with the experiments. The left panel shows the pressure time evolution recorded by the pressure transducer inside or closer the gas cavity (blue line) and the time evolution of the pressure inside the cavity calculated with the analytic model (red line). On the right panel the Fast Fourier Transform of the signals plotted on the left are shown.

From the comparison of the results emerges that the non-linear effects characterize the cavity behaviour specially when the ullage pressure is much lower than the atmospheric value. The cavity size shows a dependence from the ullage pressure. In particular, as the pressure decreases, the dimension of the cavity seems to decrease too for the cases marked 63 mm (*medium* cavity size) while an opposite behaviour is observed for the cases 65 mm (*small* cavity size). In both cases, the natural oscillation frequency decreases with the ullage pressure. From the linear model it has been observed that the resonance frequency decreases as the cavity size become larger, this can lead to say that, in this case, the influence of

distance d (m)	distance y_b (m)	radius r_0 (m)	frequency (Hz) Hattori experiment	frequency (Hz) Topliss analytical model	frequency (Hz) proposed model
.06	.016	.011	210	235	194
.06	.017	.011	210	228	190
.061	.017	.011	210	228	190
.031	.038	.007	210	233	206
.032	.04	.007	210	231	204
.033	.042	.007	210	229	202
.031	.024	.008	190	241	208
.031	.04	.008	190	207	183
.031	.044	.008	190	202	179
.027	.025	.02	104	142	111
.029	.041	.02	104	106	88
.029	.043	.02	104	104	87
.029	.044	.024	100	93	76
.03	.047	.024	100	90	74
.03	.05	.024	100	87	72
.032	.037	.02	99	113	92
.032	.044	.02	99	104	87
.032	.049	.02	99	99	84

Table 3.1. Comparison of the natural oscillation frequency of a gas cavity during a wave impact. In the first two columns the distance of the cavity center from the bottom of the tank and from the free surface are indicated respectively, in the third column the cavity radius is indicated while in the last three columns the natural frequency estimated from the experiment, from the Topliss analytical model and from the proposed model are reported.

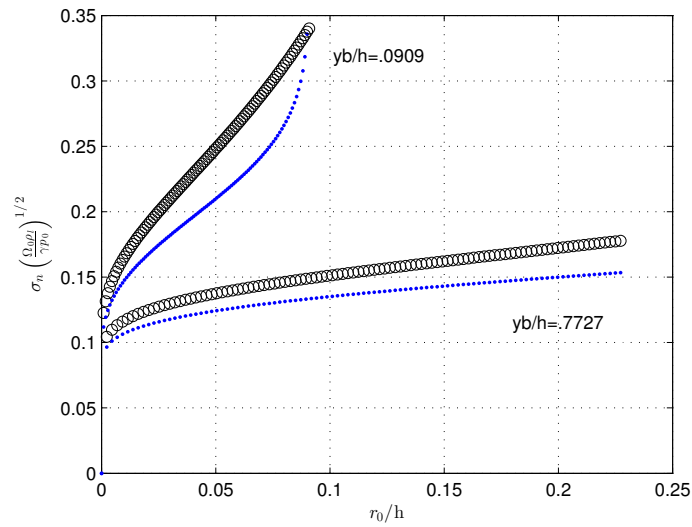


Figure 3.8. Non dimensional natural frequencies (blue dots) compared with the ones from Topliss analytical model (black circles).

the ullage pressure on the natural frequency of oscillation is most influent with respect to the cavity size and position. In all the presented cases, the comparison of the natural frequency shows a quite good agreement between the values obtained experimentally and those calculated numerically with the analytical model, in special way, with the non-linear one. The Topliss's model shows an overestimation of the frequency for all the cases.

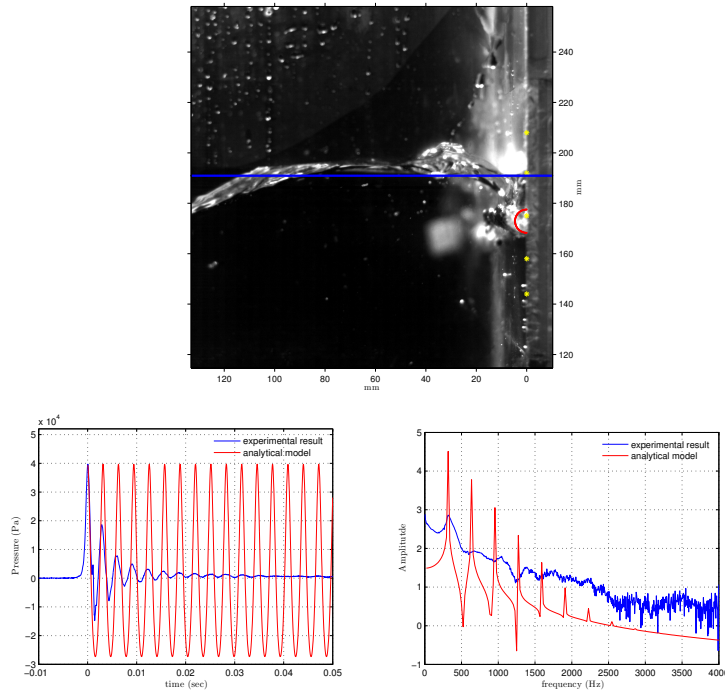


Figure 3.9. Medium cavity size at 1000 mbar, $r_0=.0052$ m, $d=.1729$ m, $h=.1910$ m, Non-Linear model 320 Hz, Linear model 319.61 Hz, Topliss model 366.89 Hz, experimental ≈ 320 Hz.

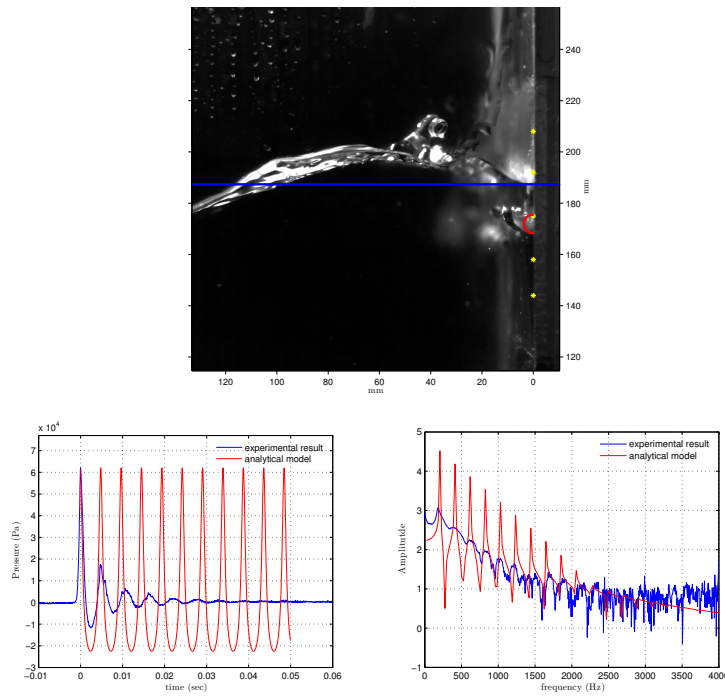


Figure 3.10. Medium cavity size at 400 mbar, $r_0=.0051$ m, $d=.1719$ m, $h=.1873$ m, Non-Linear model 200 Hz, Linear model 213.56 Hz, Topliss model 246.40 Hz, experimental ≈ 185 Hz.

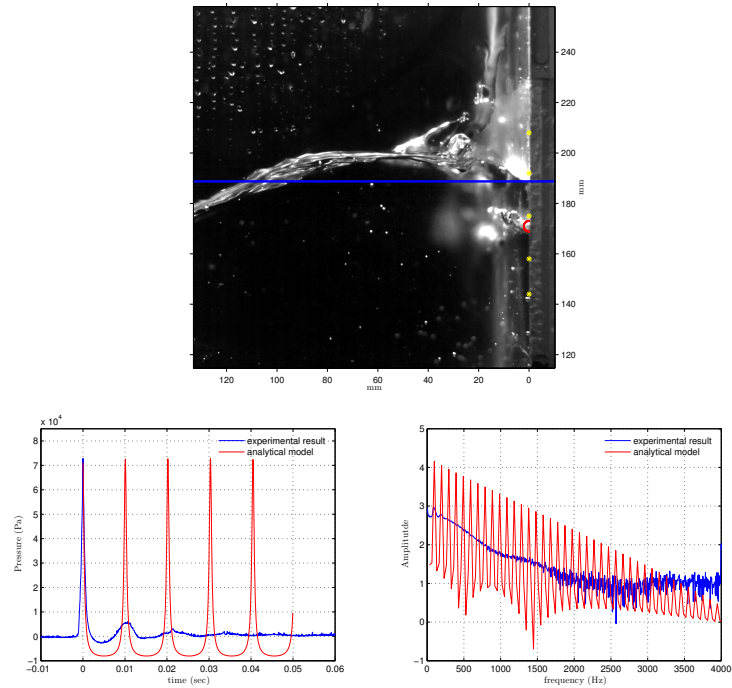


Figure 3.11. Medium cavity size at 100 mbar, $r_0=.0045$ m, $d=.1709$ m, $h=.1887$ m, Non-Linear model 100 Hz, Linear model 114.32 Hz, Topliss model 130.63 Hz, experimental ≈ 90 Hz.

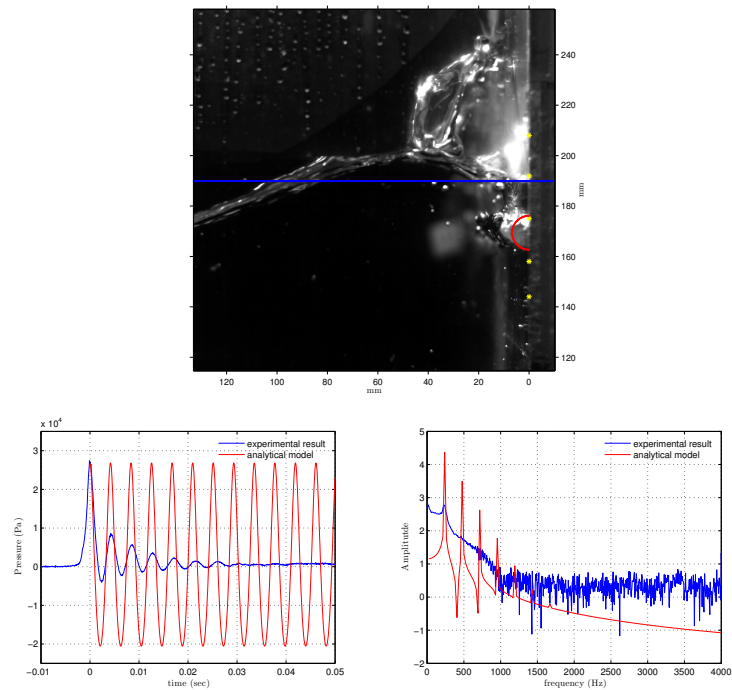


Figure 3.12. Small cavity size at 1000 mbar, $r_0=.0073$ m, $d=.1694$ m, $h=.1899$ m, Non-Linear model 240 Hz, Linear model 239.2 Hz, Topliss model 276.95 Hz, experimental ≈ 233 Hz.

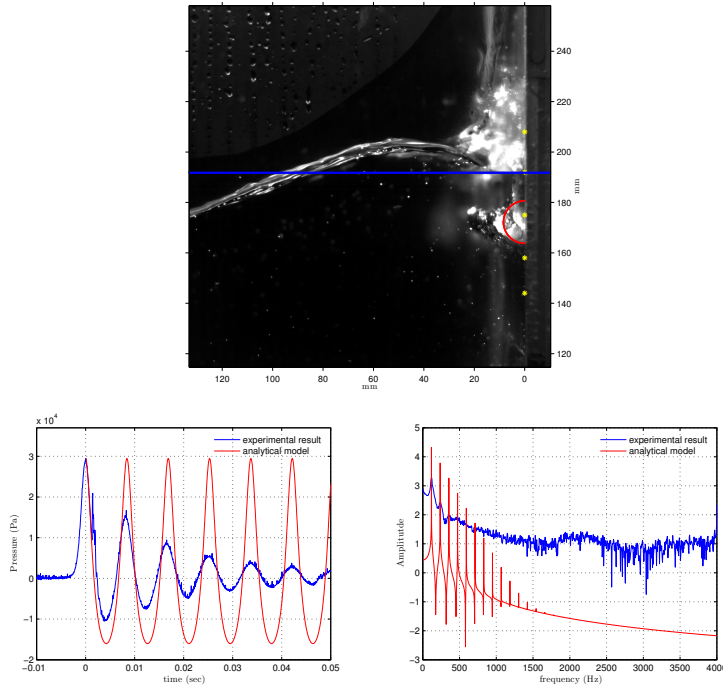


Figure 3.13. Small cavity size at 400 mbar, $r_0=.0103$ m, $d=.1722$ m, $h=.1918$ m, Non-Linear model 118 Hz, Linear model 120.14 Hz, Topliss model 141.72 Hz, experimental ≈ 120 Hz.

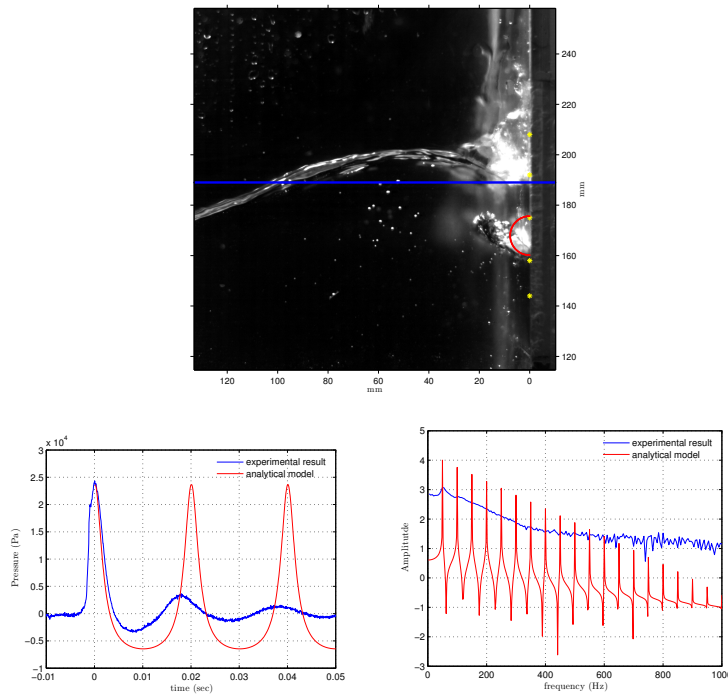


Figure 3.14. Small cavity size at 100 mbar, $r_0=.012$ m, $d=.1679$ m, $h=.1890$ m, Non-Linear model 50 Hz, Linear model 52.9 Hz, Topliss model 62.68 Hz, experimental $\approx 50/55$ Hz.

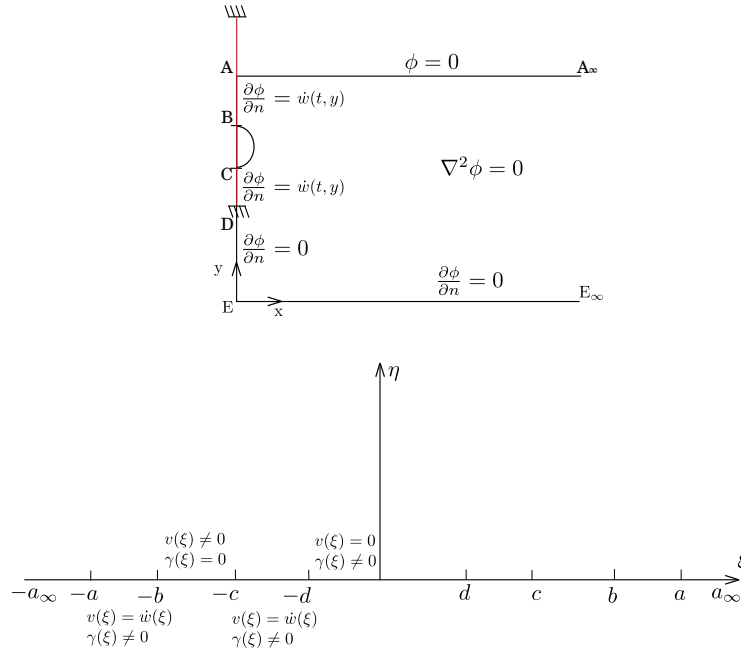


Figure 3.15. Top sketch: representation of the physical problem with boundary conditions and governing equation. \overline{AA}_∞ free surface, \overline{EE}_∞ tank bottom, \overline{AE} tank vertical wall, \overline{BC} gas cavity and D lower extrema of the elastic beam. Bottom sketch: geometry and the boundary conditions are reported in the transformed plane (ξ, η) .

3.4.2 Gas cavity hydroelastic model

Differently from the previous section, where the free oscillating problem of a gas cavity in contact with a rigid vertical wall has been considered, in this section the coupled forced problem of the gas cavity in contact with an elastic wall is presented. Figure 3.15 shows the characteristics of the problem in the physical (upper drawing) and the transformed (lower drawing) plane respectively. The elastic structure is represented by the red vertical line, the gas cavity is located between the point B and C. In order to take into account the forcing term, the velocity potential $\phi(x, y, t)$ has been considered as the superposition of two contributions: the first due to the vibrational problem ϕ_{bc} and the other one due to the incident flow $\phi_r = xV(t)f(y)$. The structure is modeled by the Euler beam theory and the displacement is expressed in term of its first eigenfunction only.

As for the previous case, we are looking for a vortex distribution along the vertical wall, with the exclusion of the cavity area, with the form of eq. (3.40):

$$\begin{aligned} \gamma(\xi) &= \frac{2}{\pi} \frac{1}{\sqrt{a^2 - \xi^2}} \int_{\text{wetbeam}} \frac{\sqrt{a^2 - x'^2}}{x' - \xi} \frac{2h}{\pi} \frac{(-\dot{w}_1(t)\psi_1(x') - V(t))}{\sqrt{1 - x'^2}} dx' + \\ &\quad \frac{2}{\pi} \frac{1}{\sqrt{a^2 - \xi^2}} \int_{\text{cavity}} \frac{\sqrt{a^2 - x'^2}}{x' - \xi} v_{\text{cav}}(x') dx' = \\ &= \frac{2}{\pi} \frac{1}{\sqrt{a^2 - \xi^2}} \left[\dot{w}_1(t)f_v(\xi) + V(t)f_v(\xi) + \int_{\text{cavity}} \frac{\sqrt{a^2 - x'^2}}{x' - \xi} v_{\text{cav}}(x') dx' \right] \end{aligned} \quad (3.55)$$

Because the vorticity is equal to zero inside the cavity, $c \leq |\xi| \leq b$, by solving integral equation in the square bracket of eq.(3.55), we get the expression of the velocity inside the cavity:

$$v_{cav}(\xi) = \frac{1}{\pi^2} \frac{-(D(t)\xi + \dot{w}_1(t)F(\xi) + V(t)F_v(\xi)) \text{sign}(\xi)}{\sqrt{a^2 - \xi^2} \sqrt{(\xi^2 - b^2)(c^2 - \xi^2)}} \quad (3.56)$$

Substituting the expression of the cavity velocity in eq. (3.55), we find the vorticity distribution along the vertical wall:

$$\gamma(\xi) = \frac{2}{\pi} \frac{1}{\sqrt{a^2 - \xi^2}} \left[\dot{w}_1(t) (f(\xi) + G(\xi)) + V(t) (f_v(\xi) + G_v(\xi)) + \frac{D(t)\xi \text{sign}(|\xi| - c)}{\pi \sqrt{(\xi^2 - b^2)(\xi^2 - c^2)}} \right] \quad (3.57)$$

As done for the rigid case, using the expression (3.38) for the horizontal velocity component and integrating from the free surface (-a) to the cavity boundary (-b) (see eqs. 3.47-3.48), we get the value of the dynamic pressure inside the cavity:

$$p_d(t) = \rho_l \left(\frac{-\dot{D}(t)K \left[\sqrt{\frac{1-(b/a)^2}{1-(c/a)^2}} \right]}{\pi^2 \sqrt{a^2 - c^2}} + \ddot{w}_1(t)\Phi_B + \dot{V}(t)\Phi_v \right) \quad (3.58)$$

By integrating the vertical component of velocity along the cavity (from -b to -c, see eq. 3.50) we get time rate of change of the cavity volume:

$$\dot{\Omega} = -\frac{D(t)}{\pi^2 \sqrt{a^2 - c^2}} K \left[\sqrt{\frac{1 - (b/c)^2}{1 - (a/c)^2}} \right] + \dot{w}_1(t)\Omega_B + V(t)\Omega_v \quad (3.59)$$

Using the state equation for gases and the mass conservation equation ($\Omega_{gas}\rho_{gas} = \Omega_0\rho_0$), as done for the ‘‘rigid’’ model, we obtain the non-linear hydroelastic model:

$$\begin{cases} \dot{\Omega}(t) = D_1(t)\bar{K} + \dot{w}_1(t)\Omega_B + V(t)\Omega_v + F_\mu(\Omega) \\ \dot{D}_1(t) = \frac{p_0}{\rho_l} \left[1 - \left(\frac{\Omega_0}{\Omega(t)} \right)^\gamma \right] - \ddot{w}_1(t)\Phi_B - \dot{V}(t)\Phi_v \\ M\ddot{w}_1(t) + C\dot{w}_1(t) + EI\left(\frac{1}{l}\right)^4 w_1(t) = \int P(y, t)\psi_1(y)dy = \int_{-a}^{-d} P(\xi, t)\psi_1(\xi)\frac{dy}{d\xi}d\xi \end{cases} \quad (3.60)$$

In the first equation of the system (3.60) the artificial term $F_\mu(\Omega)$ has been added to try to keep into account the dissipative effects which are not present in the presented model. If the pressure acting on the beam is approximated by the time derivative of the velocity potential, $P(\xi, t) \approx -\rho \frac{d\phi(\xi, t)}{dt}$, the R.H.S of the third equation of the dynamic system can be written as:

$$\int_{-a}^{-d} P(\xi, t)\psi_1(\xi)\frac{dy}{d\xi}d\xi = -\ddot{w}_1 M_{add} + p_0 \left(-1 + \frac{\Omega_0}{\Omega(t)} \right)^\gamma K_s - \dot{V}(t)M_v \quad (3.61)$$

where

$$\begin{cases} M_{add} = \int_{\xi_{wetbeam}}^{\xi_{cavity}} \rho_l \left(\phi_b(\xi) - \frac{\Phi_B}{\Phi_R} \phi_r(\xi) \right) \psi_1(\xi) \frac{dy}{d\xi} d\xi \\ K_s = \int_{\xi_{wetbeam}}^{\xi_{cavity}} \frac{\phi_r(\xi)}{\Phi_R} \psi_1(\xi) \frac{dy}{d\xi} d\xi + \int_{\xi_{cavity}} \psi_1(\xi) \frac{dy}{d\xi} d\xi = K_c + \Psi_c \\ M_v = \int_{\xi_{wetbeam}} \rho_l \left(\phi_v(\xi) - \frac{\Phi_v}{\Phi_R} \phi_r(\xi) \right) \psi_1(\xi) \frac{dy}{d\xi} d\xi \end{cases}$$

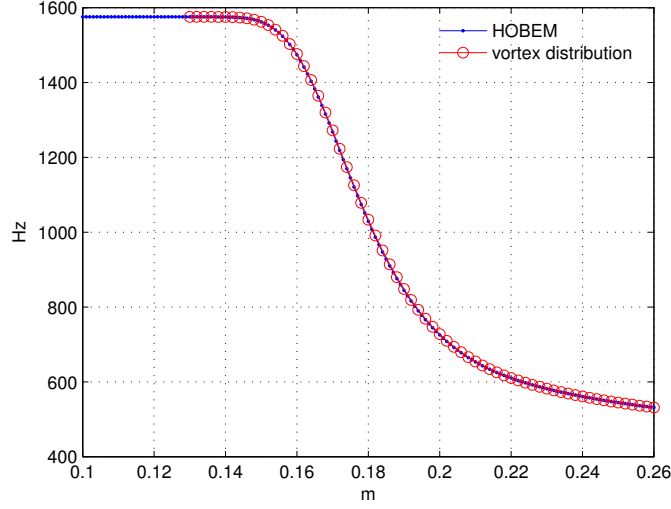


Figure 3.16. First wet natural frequency as function of the filling depth. Comparison of the results obtained by solving the fluid problem with a HOBEM method (blue markers) and using the vortex distribution along the vertical wall.

Taking the derivative with respect to time of the first equation in (3.60) and substituting the value of \dot{D}_1 in both the equations we get:

$$\begin{cases} \ddot{\Omega}(t) = -p_0 \left(\frac{\Omega_0}{\Omega(t)} \right)^\gamma K_\Omega - \mu \dot{\Omega}(t) + K_{\Omega w} \frac{C}{M_{tot}} \dot{w}_1(t) + K_{\Omega w} \frac{K_{EL}}{M_{tot}} w_1(t) + p_0 K_\Omega + \dot{V}(t) K_{\Omega V} \\ \ddot{w}_1(t) = p_0 \left(\frac{\Omega_0}{\Omega(t)} \right)^\gamma \frac{K_s}{M_{tot}} - \frac{C}{M_{tot}} \dot{w}_1(t) - \frac{K_{EL}}{M_{tot}} w_1(t) - p_0 \frac{K_s}{M_{tot}} - \dot{V}(t) \frac{M_v}{M_{tot}} \end{cases} \quad (3.62)$$

where $M_{tot} = M + M_{add}$, $K_{\Omega w} = \bar{K} \Phi_B - \Omega_B$, $K_{\Omega V} = -\bar{K} \Phi_V + \Omega_v + K_{\Omega w} M_v / M_{tot}$ and $K_\Omega = \bar{K} / \rho_l + K_{\Omega w} K_s / M_{tot}$. The time derivative of the unknown function F_μ gives the damping term $\mu \dot{\Omega}$.

In figure (3.16) the behaviour of the first wet natural frequency of the beam is shown as function of its wetted length. It has been calculated avoiding the gas cavity in the analytical model. The comparison with the values estimated with a HOBEM method shows the same results which are consistent with the experimental findings [22].

The linearization of the non-linear term $\Omega^{-\gamma}$ in the dynamic system (3.62) allows the study of coupled eigenvalues as function of different parameters of the system. In figure (3.17) the behaviour of the coupled problem eigenvalues (dots) is shown as function of the cavity radius r . The values of the same eigenvalues are also shown when the two problems (i.e. cavity and beam oscillation) are considered uncoupled (circles, green and magenta, respectively). It is possible to observe the asymptotic behavior of the eigenvalues (dots): when the cavity size is very small or comparable with the beam length the eigenvalues tend to their values in the case of uncoupled problem. In the other conditions the presence of the gas cavity seems to induce a reduction of the added mass effects on the beam due to the presence of the liquid (vertical shift of the red line with respect to the purple one). This is due not only to the fact that the presence of the gas cavity reduces the wetted length of the beam but also to an additional contribution related to the coupling of the two dynamic system. In (3.62), in the M_{add} equation, beside the term ϕ_b , which is used for the added

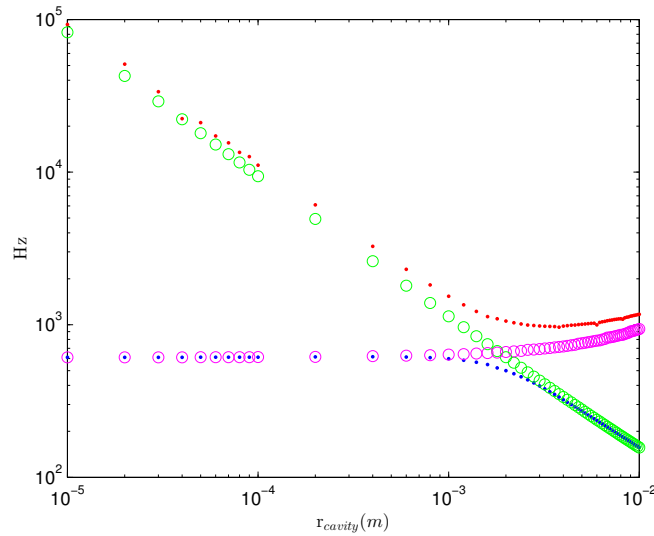


Figure 3.17. Behaviour of the eigenvalues of the linearized dynamic system as function of the cavity radius (red and blue dots). The circle show the eigenvalues trends in the case of uncoupled problem.

mass estimation in absence of gas cavity, it appears the term $-\Phi_B/\Phi_R\phi_r$, which is due to the coupling of the beam and cavity problems. A further consideration, which can be done by observing the figure 3.17 is the fact that no resonance condition will occur. The eigenvalues of the coupled system will be always quite separated.

Figures (3.19) to (3.24) show the comparison between the proposed model and the experimental results. The cases considered are the same that have been shown for the rigid wall case. Each panel shows the comparison of the deformation of the structure calculated in the middle of the beam (top), their Fourier transform (middle) and the hydrodynamic pressure in two points close to the bottom of the tank (bottom). In each caption the parameters used in the model are indicated: the water height h , the position of the cavity center y_{r0} , the radius of the cavity r_0 and its volume Ω_0 , the maximum velocity at the moment of the wave impact V_{max} , the quantity T_a which characterize the impulsive behaviour of the impact and the damping coefficient μ . All the parameters, with the exclusion of the damping coefficient and T_a , have been estimated from the experimental activities. In particular they have been extracted from the images of the fast cam. From the frame corresponding to the closure of the cavity against the wall the wave height, the radius and the position of the cavity and also the area where the forcing term acts have been calculated. From the evolution of the wave before the closure of the cavity, the speed at the instant of the impact has been estimated. Figure (3.18) shows an example of how the model configuration appears with respect to the experimental case. The blue line shows the water level, the red half circle represents the size and the position of the gas cavity, which will be constant for all the temporal evolution. The green line (which, in the figure, is not in the right scale, its maximum value is 1) shows the vertical shape of the forcing term $\phi_r = xV(t)f(y)$. Such shape is due to the fact that the fluid flow, below the cavity, is vertical, while in the upper part (from the cavity center till the free surface) the flow direction is almost horizontal. The temporal law assumed

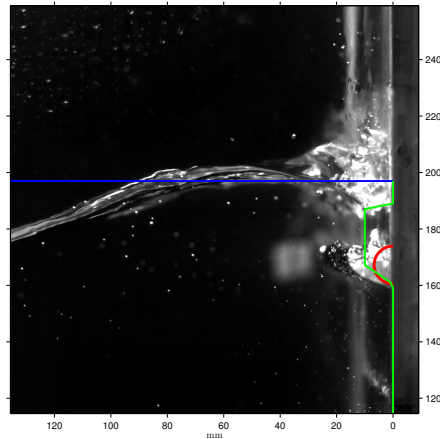


Figure 3.18. Comparison between the experiment and the analytical model in terms of impact scenario with gas-cavity. The colored lines of the model are explained in the main text.

for $V(t)$ is $V_{max}/(1 + \exp(-T/T_a))$. Once the parameters have been fixed, the value of T_a has been chosen to fit, as much as possible, the first peak of the deformation both in terms of its maximum value and in terms of rise time. Similar to the experimental results, also the model shows a behaviour of the system which is driven principally by the cavity dynamics. The external forcing is such to excite also the natural frequency of the structure but the pressure oscillation due to gas compressibility inside the cavity prevails. From the comparison of the Fourier transforms, it is possible to note how the model overestimates the contributions of the non-linear frequencies, particularly in the case of ullage pressure equal to the atmospheric value and in case of large cavity. This can be ascribed to a non accurate modelling of the damping term for the cavity. The hypothesis of stationary state for the water height at the wall, as well as for the cavity position, used in the analytical model, is reflected by the fact that the oscillation frequency, which characterizes the model response does not change in time. While the predicted frequency is quite similar to the experimental one during the first oscillation cycles ($t < 0.01/0.02$ sec), successively a temporal shift between the signals is present in agreement with the increasing of the distance between the free surface and the cavity, which determines the decreasing of the natural frequency. From the case in figure (3.21) it is possible to notice that the structure is highly damped when oscillating in water and the only structural damping, present in the model, is not enough. In fact the high frequency, associated with the first wet natural frequency of the structure, persists for a longer time with respect to the experimental case.

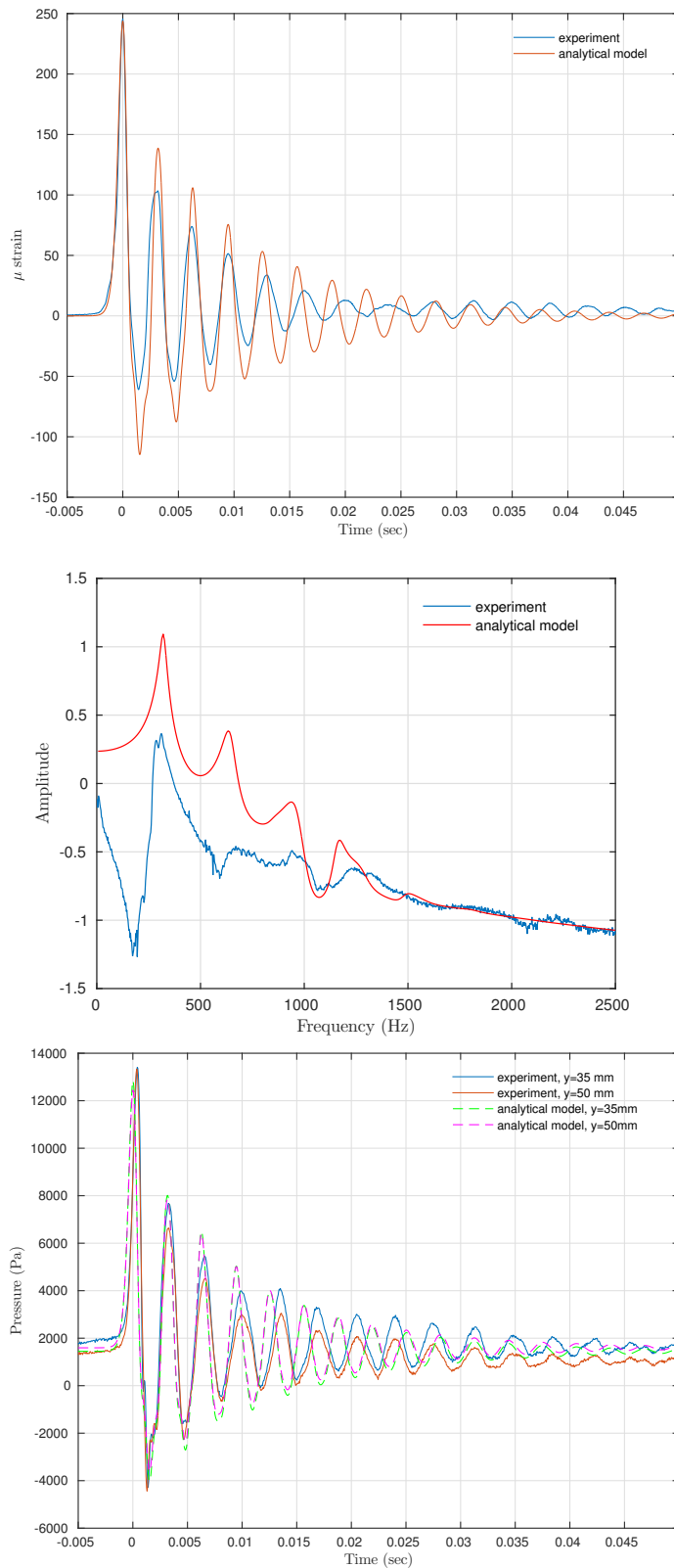


Figure 3.19. Comparison between experiments and analytical model of impact with gas cavity: *Medium* size cavity - 1000 mbar. Top plot: structural stresses evaluated in the middle of the structure. Center plot: Fast Fourier Transform of stress signals. Bottom plot: hydrodynamic pressure for the two pressure transducers located close to the tank bottom. Parameters used in the analytical model: $h = 0.19765$ m, $y_{r0} = .17215$ m, $r_0 = .00463$ m, $\Omega_0 = 3.36E-5$ m², $V_{max} = 2$ m/s, $T_a = 3.0E-4$ s, $\mu = 200$.

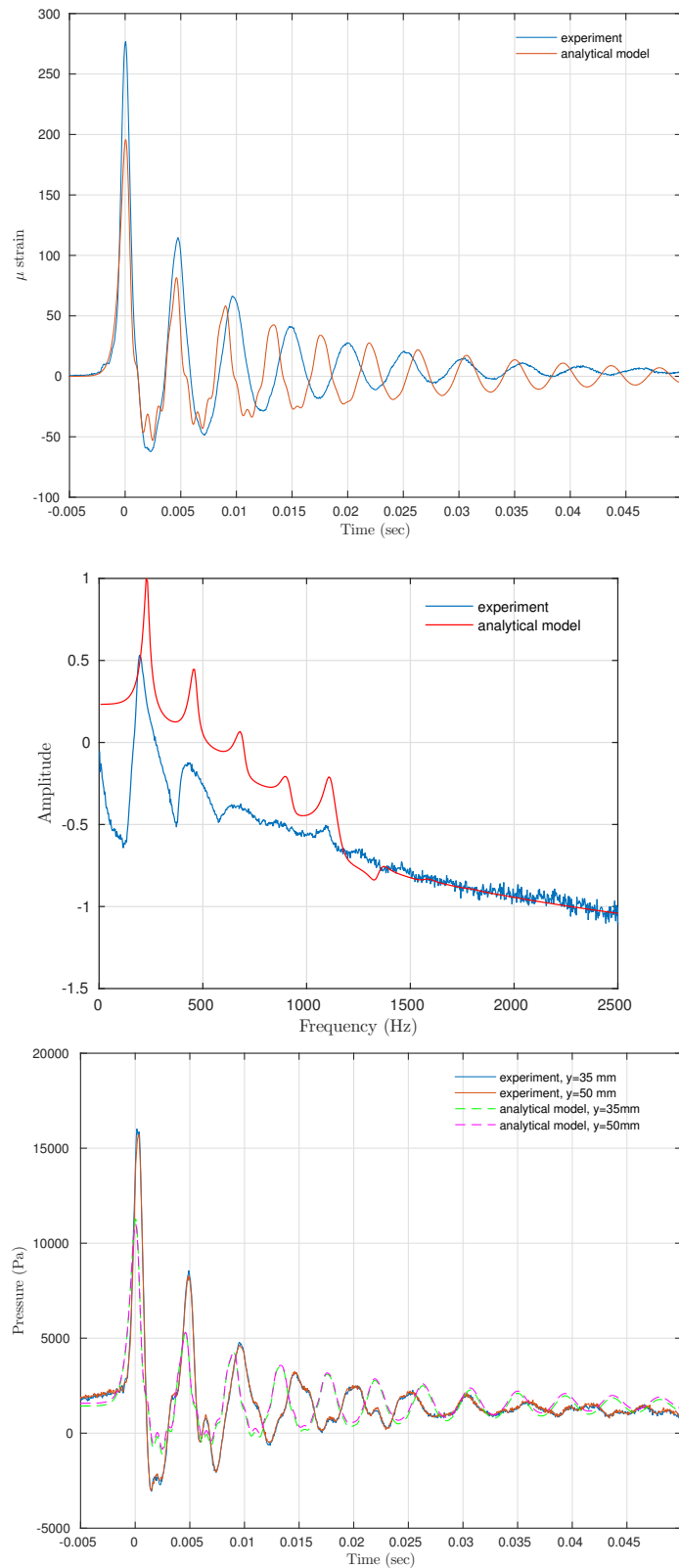


Figure 3.20. Comparison between experiments and analytical model of impact with gas cavity: *Medium* size cavity - 400 mbar. Top plot: structural stresses evaluated in the middle of the structure. Center plot: Fast Fourier Transform of stress signals. Bottom plot: hydrodynamic pressure for the two pressure transducers located close to the tank bottom. Parameters used in the analytical model: $h = .19507$ m, $y_{r0} = .17086$ m, $r_0 = .00376$ m, $\Omega_0 = 2.207 \cdot 5$ m², $V_{max} = 2$ m/s, $T_a = 4.6E-4$ s, $\mu = 100$.

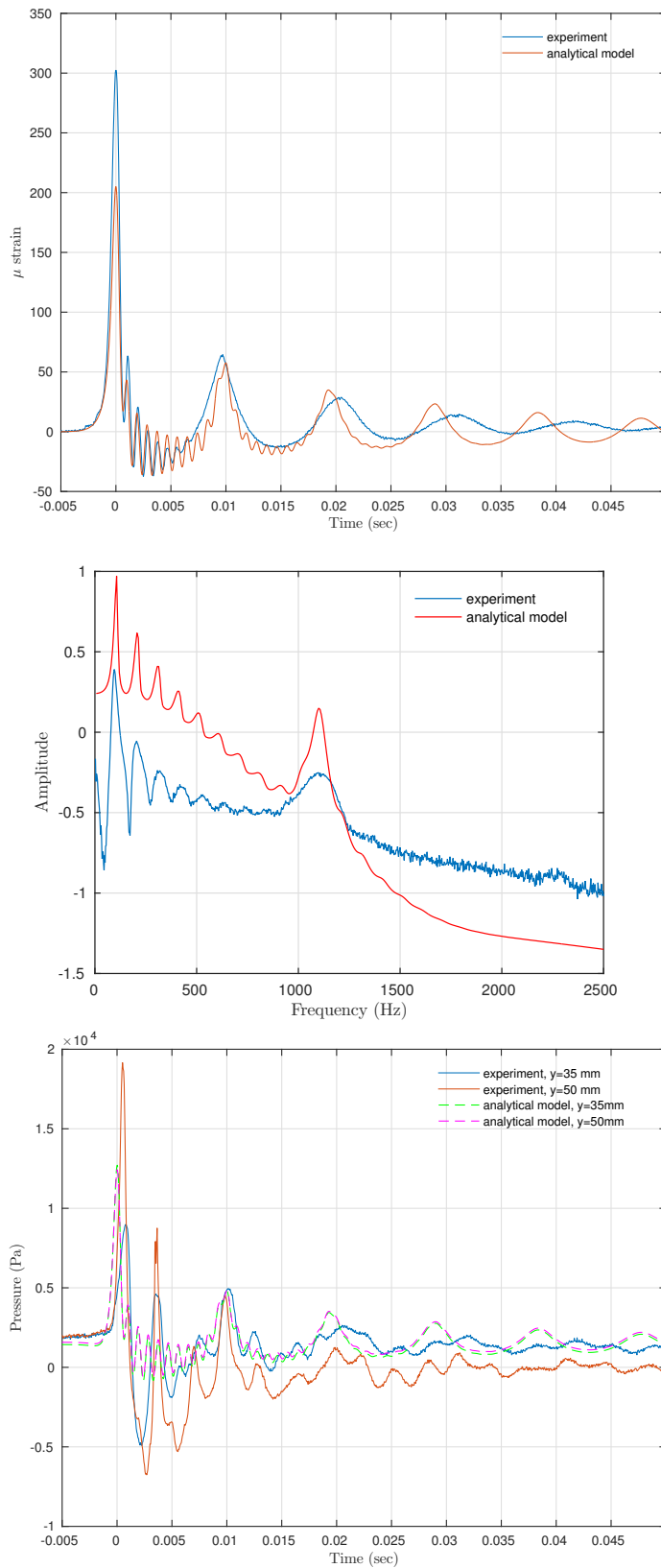


Figure 3.21. Comparison between experiments and analytical model of impact with gas cavity: *Medium* size cavity - 100 mbar. Top plot: structural stresses evaluated in the middle of the structure. Center plot: Fast Fourier Transform of stress signals. Bottom plot: hydrodynamic pressure for the two pressure transducers located close to the tank bottom. Parameters used in the analytical model: $h = .19559$ m, $y_{r0} = .17260$ m, $r_0 = .00495$ m, $\Omega_0 = 3.30E-5$ m², $V_{max} = 2$ m/s, $T_a = 6.2E-4$ s, $\mu = 60$.

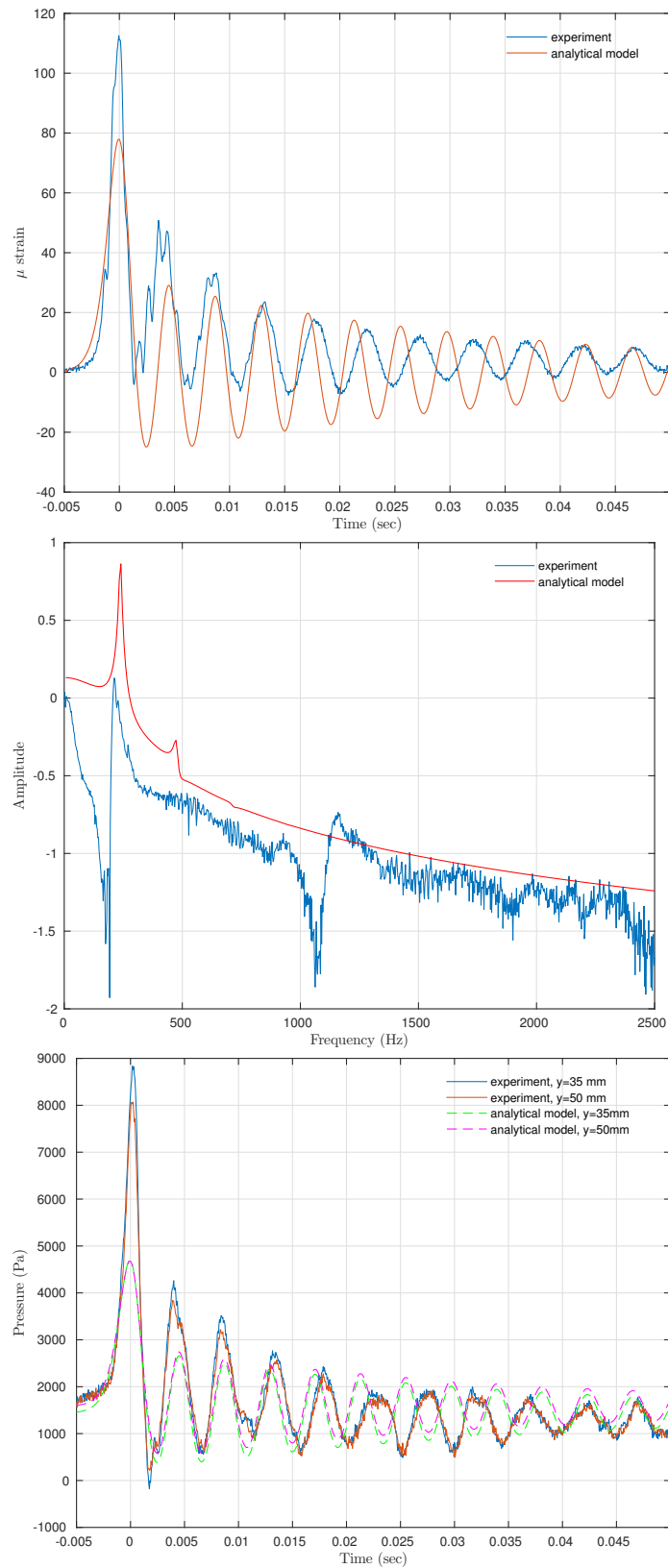


Figure 3.22. Comparison between experiments and analytical model of impact with gas cavity: *Large size cavity - 1000 mbar.* Top plot: structural stresses evaluated in the middle of the structure. Center plot: Fast Fourier Transform of stress signals. Bottom plot: hydrodynamic pressure for the two pressure transducers located close to the tank bottom. Parameters used in the analytical model: $h = .19610$ m, $y_{r0} = .17240$ m, $r_0 = .00734$ m, $\Omega_0 = 8.46E-5$ m², $V_{max} = 2$ m/s, $T_a = 8.0E-4$ s, $\mu = 60$.

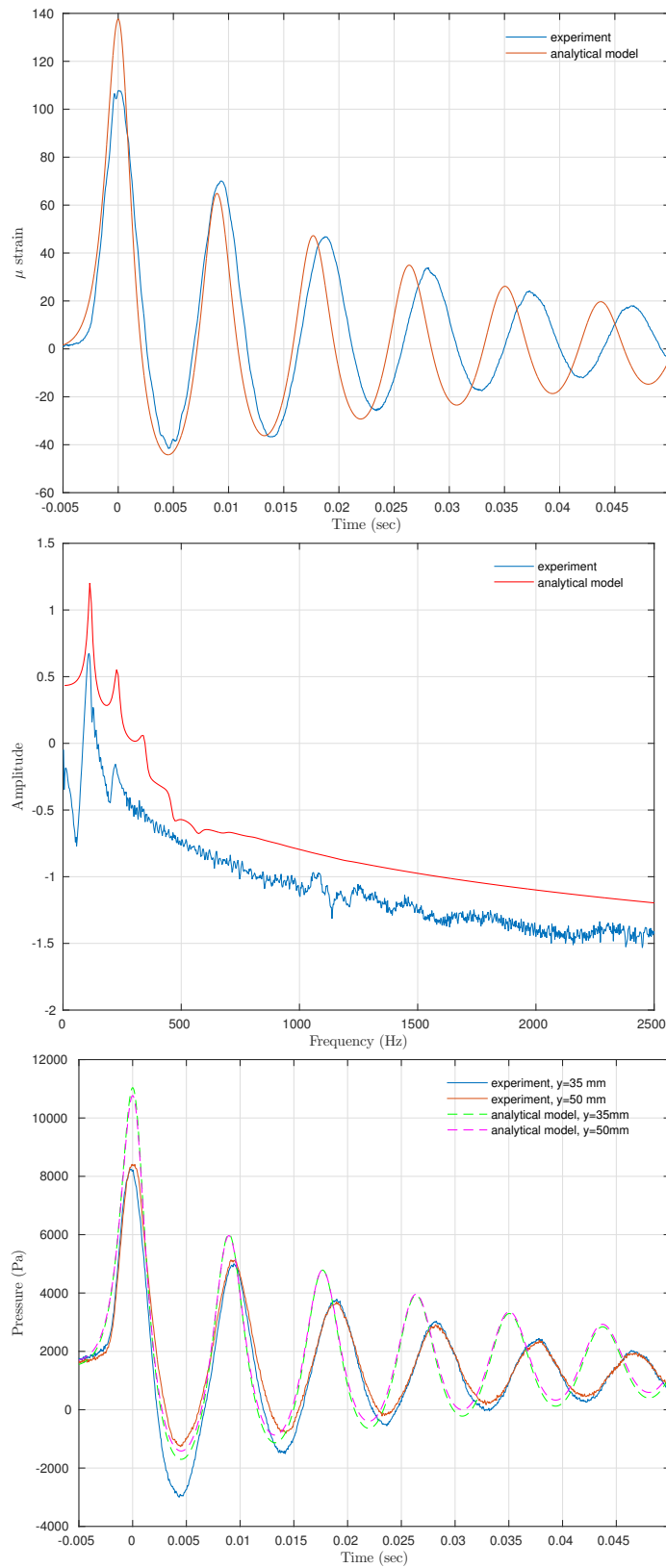


Figure 3.23. Comparison between experiments and analytical model of impact with gas cavity: *Large size cavity - 400 mbar.* Top plot: structural stresses evaluated in the middle of the structure. Center plot: Fast Fourier Transform of stress signals. Bottom plot: hydrodynamic pressure for two pressure transducers located close to the tank bottom. Parameters used in the analytical model: $h = .19765$ m, $y_{r0} = .16306$ m, $r_0 = .00867$ m, $\Omega_0 = 1.18E-4$ m², $V_{max} = 2$ m/s, $T_a = 9.0E-4$ s, $\mu = 60$.

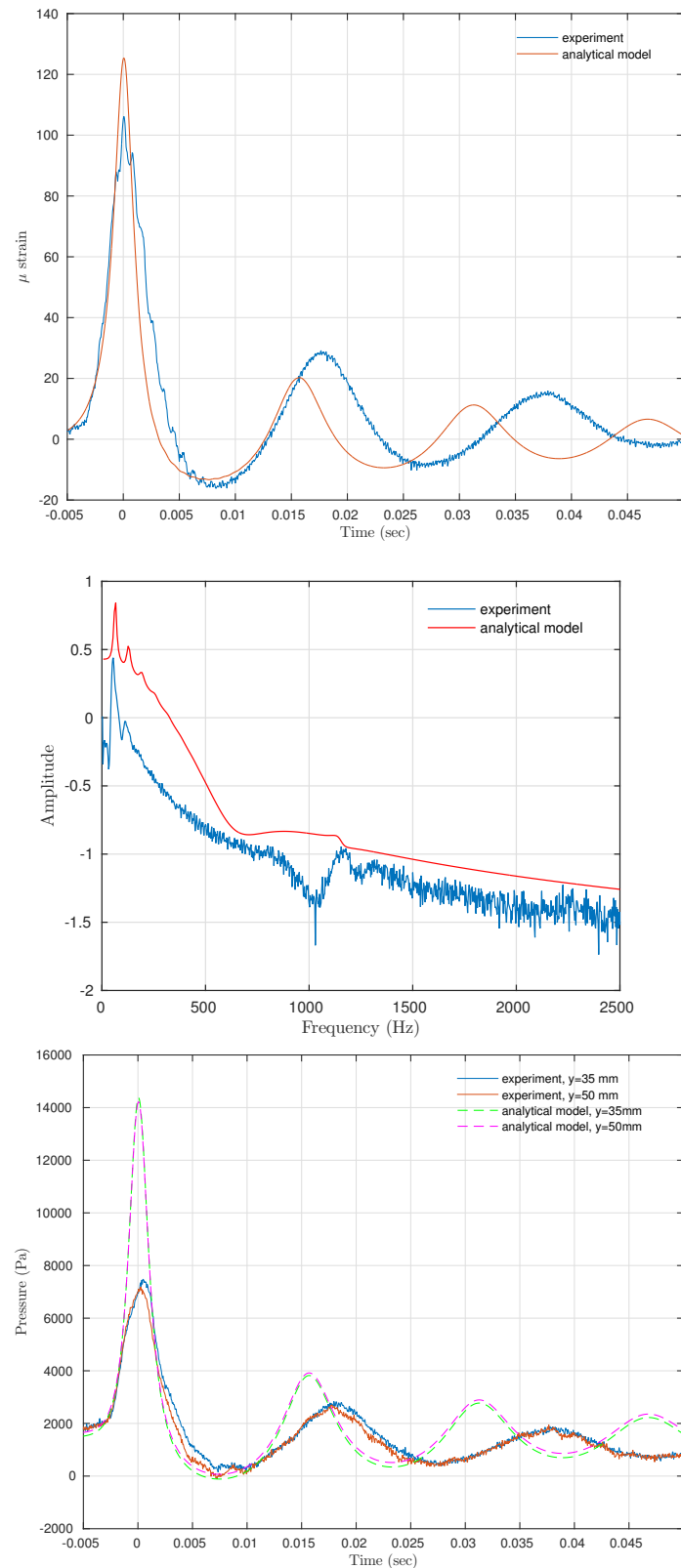


Figure 3.24. Comparison between experiments and analytical model of impact with gas cavity: *Large size cavity - 100 mbar.* Top plot: structural stresses evaluated in the middle of the structure. Center plot: Fast Fourier Transform of stress signals. Bottom plot: hydrodynamic pressure for the two pressure transducers located close to the tank bottom. Parameters used in the analytical model: $h = .19817$ m, $y_{r0} = .16573$ m, $r_0 = .00695$ m, $\Omega_0 = 7.59E-5$ m², $V_{max} = 2$ m/s, $T_a = 1.3E-3$ s, $\mu = 60$.

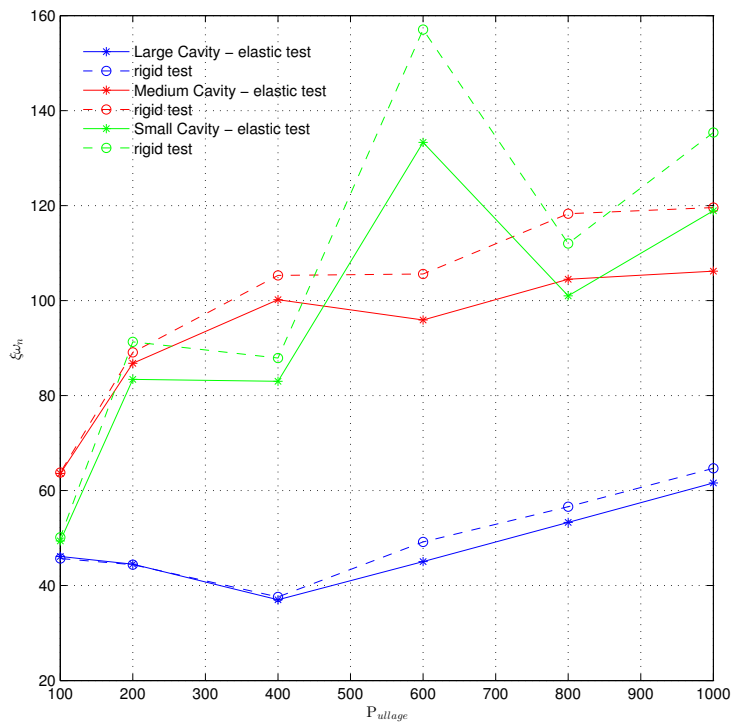


Figure 3.25. Comparison between the exponential decay as function of ullage pressure, for rigid and elastic test, marked with dashed and continuous lines respectively. The different colors refer to the three different cavity sizes: blue for large, red for medium and green for small cavity.

Chapter 4

Numerical Model

In the previous chapter we introduced the simplified mathematical model which reproduces the phenomena observed during the experiments and some semi-analytical/analytical solutions concerning only the hydroelastic interaction disregarding at all the sloshing problem. Here, the solution of the mathematical problem is treated from a purely numerical point of view. In the first part, following the scheme of the previous chapter, we present, separately, the numerical procedures which have been employed for the solution of the three mathematical sub-problems. For each of them, the results of the numerical schemes are compared against reference case in order to check the accuracy. In the second part of the chapter, the hydroelastic numerical model is discussed. In particular the coupling of the sub-problems during the time integration. Due to numerical difficulties arised during the simulation of the wave impact events, any fully numerical results of the hydroelastic interaction will be presented. Alternatively, the results of sloshing stage simulation, just before the impact phenomenum, has been employed for a parametric study on the forcing term for the semi analytical model proposed in the preuiuous chapter.

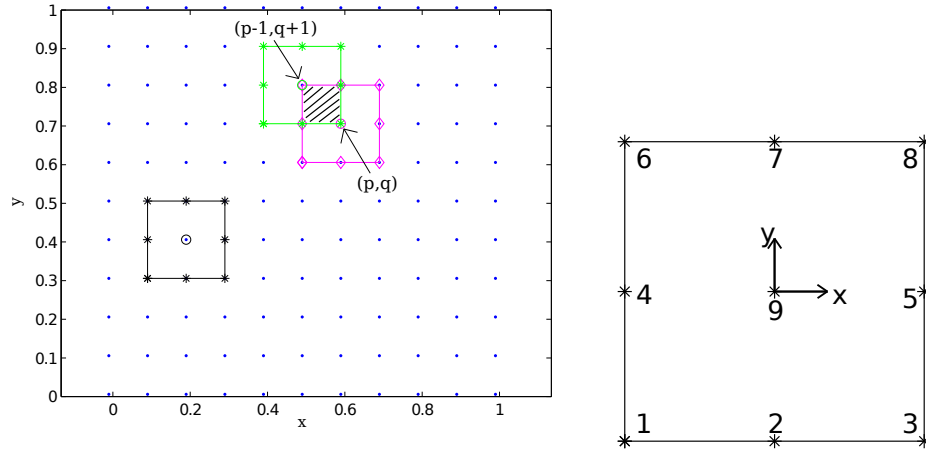


Figure 4.1. Domain discretization.

4.1 Sloshing Stage

The sloshing mathematical problem (3.1), (3.2), (3.3) and (3.4) is solved with a two step mixed Eulerian-Lagrangian (MEL) approach [26] [33]. This method, which is widely used for free-surface problems, consists in dividing the mathematical problem into a kinematic (Eulerian) and a time evolution (Lagrangian) sub-part. During the kinematic step, at a given time t , the Laplace equation is solved using the instantaneous geometry of the water domain, as it was frozen, and knowing the velocity potential on the free surface and its normal gradient on the solid boundaries. During the time evolution part the kinematic and dynamic free-surface boundary conditions are stepped forward in time updating the free-surface configuration and the values of the velocity potential on the nodes on the free surface. The applied time integration scheme is the explicit fourth order Runge-Kutta. During the sloshing stage, the normal velocity along the solid boundaries is known at any time instant .

4.1.1 Potential flow solver

Two different approaches exist for the solution of Laplace equation: the field methods and the boundary methods. For the first class the discretization of the whole domain is required while for second only the discretization of the domain boundary is necessary. This, generally, implies a lower number of unknowns for the second methodology but leads to a full matrix of the algebraic system to be solved numerically, while for the field class methods the matrix is sparse or banded if a structured grid is used. Speaking in term of computational cost, both memory usage and computation time, the use of sparse matrix instead of a full one is an advantage specially when the sparsity is lower than \mathbf{xx} % (for the method used here $\approx 1\%$).

In this work a new field method, proposed by Faltinsen and Shao [32], named Harmonic Polynomial Cell (HPC) method has been used. The high accuracy of the method, up to 4^{th} order, as well as the easy way to determine the coefficients of the algebraic system matrix were the reasons leading to the choice of such approach.

The velocity potential $\phi(x,y)$, in each nodes of the numerical grid (blue dots, see fig.

n	z^n
0	1
1	$x + iy$
2	$(x^2 - y^2) + i(2xy)$
3	$(x^3 - 3xy^2) + i(3x^2y - y^3)$
4	$(x^4 - 6x^2y^2 + y^4) + i(4x^3y - 4xy^3)$

Table 4.1. Two-dimensional harmonic polynomials with corresponding order n .

(4.1)), is approximated by a linear combination of harmonic functions, which automatically satisfy the Laplace equation. Then, the coefficients of the expansion are expressed, via a collocation procedure, as function of the velocity-potential values in the surrounding nodes, which form the associated stencil (for example, to the generic grid point (p, q) in fig.4.1 is associated the magenta stencil). Repeating the procedure for each point of the discretized domain, an algebraic linear system, for the unknown values of the velocity potential on the grid nodes, is obtained in the form

$$\phi(x, y) = a_i f_i(x, y) \quad (4.1)$$

Eq. (4.1) is the expansion of the velocity potential, where the Einstein notation of repeated indexes has been adopted. The harmonic functions $f_i(x, y)$ originate from the real and imaginary part of the complex polynomial $z = (x + iy)^n$, in particular, to achieve a 4th order approximation the first 8 functions are necessary, i.e. up to the real part of z^4 (see table (4.1)). Such functions are:

$$f_1(x, y) = 1; f_2(x, y) = x; f_3(x, y) = y; f_4(x, y) = x^2 - y^2; f_5(x, y) = 2xy;$$

$$f_6(x, y) = x^3 - 3xy^2; f_7(x, y) = 3x^2y - y^3; f_8(x, y) = x^4 - 6x^2y^2 + y^4.$$

Applying eq. (4.1) at the stencil boundary nodes (x_j, y_j) where $j = 1, \dots, 8$ (see fig. (4.1)), the coefficients a_i are obtained by solving the “local” algebraic system:

$$\phi_j = f_{ji} a_i \quad \Rightarrow \quad a_i = f_{ij}^{-1} \phi_j \quad (4.2)$$

if the velocity potential is known at such nodes. Therefore, the way to express the coefficients a_i is equivalent to consider a sub Dirichlet boundary problem in the stencil with the Laplace equation as the governing equation and where the boundary conditions are assigned on the boundary nodes. By replacing the coefficients a_i in eq. (4.1) we get the velocity potential inside a cell interpolated only by the velocity potential at its boundary nodes:

$$\phi(x, y) = f_i(x, y) f_{ij}^{-1} \phi_j \quad (4.3)$$

This last equation is then evaluated in the inner 9th node of the cell (x_9, y_9) giving:

$$\phi_9 = c_j \phi_j, \quad \text{where} \quad c_j = f_i(x_9, y_9) f_{ij}^{-1} \quad (4.4)$$

The repetition of the operation for all the center-cell nodes of the domain ensures the continuity of the flow. The Neumann boundary conditions, i.e. known normal velocity, are imposed by the analytical derivative of eq. (4.3) at the boundary nodes:

$$\frac{\partial \phi(x, y)}{\partial n} = \frac{\partial f_i(x, y)}{\partial n} f_{ij}^{-1} \phi_j \quad (4.5)$$

while for the Dirichlet boundary conditions, i.e. known velocity potential, are directly assigned on the inner nodes of the discretized domain:

$$\phi_g = \phi^* \quad (4.6)$$

Putting together the continuity constraint and the boundary condition equations (4.4-4.5/4.6) for all the computational nodes we get a “global”, i.e. for whole liquid-domain problem, linear algebraic system, which can be expressed in the following matrix form:

$$A\Phi = B \quad (4.7)$$

where the coefficients matrix A is sparse with at most 9 non-zeros element for each row (c_j), Φ and B are the column vectors representing the unknowns and the boundary conditions, respectively. The dimension of the matrix A is $N \times N$, while Φ and B have dimension N , with N the number of domain nodes, as well as of the problem unknowns. For the solution of (4.7) either a direct or an iterative algorithm can be used. In this case the UMFPAK suite with a column pre-ordering algorithm as been employed [8].

Always from eq. (4.3), it is easy to derive the matrices for estimating the gradient of the velocity potential:

$$\frac{\partial \phi(x, y)}{\partial x} = \frac{\partial f_i(x, y)}{\partial x} f_{ij}^{-1} \phi_j \Rightarrow \Phi_x = A_x \Phi \Rightarrow \Phi_x = A_x A^{-1} B \quad (4.8)$$

$$\frac{\partial \phi(x, y)}{\partial y} = \frac{\partial f_i(x, y)}{\partial y} f_{ij}^{-1} \phi_j \Rightarrow \Phi_y = A_y \Phi \Rightarrow \Phi_y = A_y A^{-1} B \quad (4.9)$$

Numerical treatment of the free surface

The HPC method requires structured mesh for the discretization of the physical domain and quadrilateral cells for the calculus of the “local” coefficients. When the free surface is a single-valued function, the grid generation is straightforward. The points on the free surface can be enforced to move only along the vertical direction and consequently a grid stretching in the same direction needs to be introduced. On the other hand, when the wave is very steep or a breaking wave is present, substantial difficulties arise to generate a “good” structured mesh deforming only the original one. For this reason, with the intent to be able to capture this kind of phenomena, as for the flip-through or breaking waves, an approach with double overlapping structured mesh has been developed (see fig. (4.2)), where a coarse background grid is kept fixed while a finer one is anchored to the free-surface and evolves with it.

With reference to fig. (4.2), the blue grid is the fixed background mesh, it is obtained by dividing in quadrilateral elements an area bigger than the physical domain. In general, a stretching both in the x and/or y direction may be considered, if required. The necessity to consider a greater area is due to the fact that during the free-surface time evolution some grid points enter or leave the physical domain. Anyway, during the computation, just the points

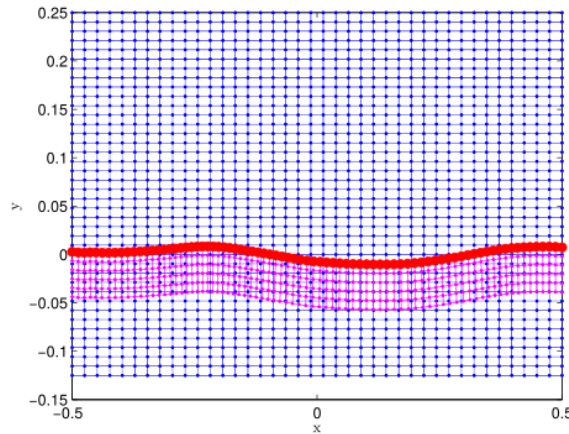


Figure 4.2. Double overlapping meshes. The blue one is the fixed background mesh, while the magenta is a moving mesh, anchored to the free-surface (red dots).

below the free-surface (red dots) are taken into account. For the nodes of the background grid, which belong to the bottom as well as to the vertical walls the Neumann boundary conditions are assigned (i.e. $\partial\phi/\partial n = \phi_n^*$). The finer grid (magenta) is structured but, differently from the blue one, it is anchored to the free-surface and moves following the free-surface motion, i.e. at each time step, after the geometry of the free-surface has been updated, the mesh is generated adapting itself to the new configuration. With respect to the free-surface, the grid rows are parallel while the columns are orthogonal. Close to the vertical boundaries, in some conditions, it may happen that, if the grid is designed following only the normal direction to the free surface, some grid points can stand outside of the domain. To avoid that problem, close to the boundary, a ramp function, which gradually rotates the grid columns from the normal to the vertical direction, has been used. On the two lateral columns and on the free surface nodes the prescribed boundary conditions are assigned. With this multi-grid configuration it is possible to identify some “special nodes”, belonging both to background and free-surface grid, for which it is impossible to define a centered stencil composed only by nodes of the same grid. These are used as connection nodes between the two grids. Typically they are in the last row for the free-surface grid and in the upper rows in the water domain for the background one. In fig. (4.3) an example of such nodes, for the background and free-surface grid, are shown named a and b , respectively. It is important to say that all the connection points, which belong to the background mesh, must be boundary points of at least one stencil of the background mesh. These “special” nodes are used to establish a communication between the two grids. The background grid, on which the Dirichlet boundary condition is not assigned, receives information from the finer grid through the nodes a . Vice-versa, the finer grid receives information for its bottom boundary condition by the nodes b . The way the grids exchange informations is explained the following considering for example the node b but the same is valid also for a nodes a : if b is observed from the background grid, it belongs to four stencils and it is possible to express its velocity potential, in each stencil, as

$$\phi(x_b, y_b)^{sten_k} = f_i(x_b, y_b) f_{ij}^{-1} \phi_j^{sten_k} \quad \text{with } k = 1, \dots, 4 \quad (4.10)$$

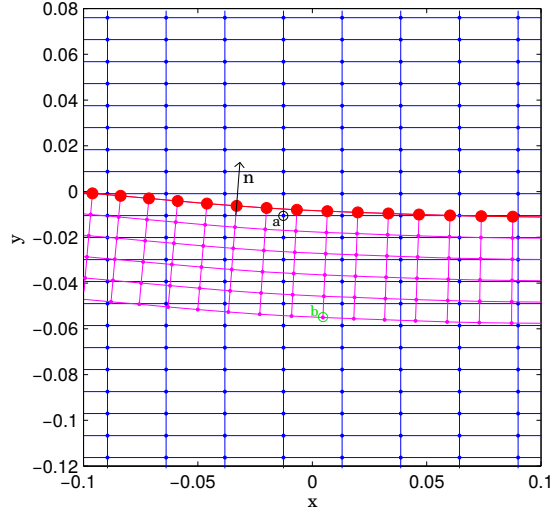


Figure 4.3. Details of the grid overlapping. The black normal vector to the free-surface shows how the moving grid (magenta) has been built. The red dots identify the free-surface nodes, while the black and green circles, named a and b , are an example of connection nodes for the background and free-surface grid, respectively.

where the index j refers to nodes of the background grid. Then a mean value is calculated:

$$\phi(x_b, y_b) = \frac{\sum_{k=1}^4 \phi(x_b, y_b)^{sten_k}}{4} \quad (4.11)$$

The necessity of the mean value is due to the non uniqueness of the interpolation of the potential in a generic point if it is estimated from different stencils. The number of points in the normal direction, as well as the spacing between them, is related to the background grid discretization. In fact, since between the two grids there is a two-way communication, an adequate overlapping is required, i.e. at least two points of the background grid must be present along the normal direction.

4.1.2 Time integration procedure

For the time evolution of eqs. (3.9), (3.10) and (3.11) an explicit 4th order Runge-Kutta (RK4) method is used. The time derivatives of the previous equations are stored as time derivative of the vector $Y = [x_p; y_p; \phi_{fs}]$ and the right-hand side in the vector F such that the time evolution problem can be written as $\dot{Y} = F(Y, t)$, where the dot denotes the time derivative.

In agreement with the accuracy order of the method used, the algebraic system (4.7) has to be solved four times for each time step. To prevent the establishment of sawtooth instabilities, each m time steps, a numerical filter [9] has been applied to the free surface position (x_p, y_p) and velocity potential (ϕ_{fs}) . The filtering frequency m depends on the characteristics of the flow and on the spatial and temporal discretization.

For $n = 1..Nt$

$$\begin{aligned} k_1 &= \Delta t F(Y_n, t_n) \\ k_2 &= \Delta t F(Y_n + \frac{1}{2}k_1, t_n + \frac{\Delta t}{2}) \\ k_3 &= \Delta t F(Y_n + \frac{1}{2}k_2, t_n + \frac{\Delta t}{2}) \\ k_4 &= \Delta t F(Y_n + k_3, t_n + \Delta t) \end{aligned}$$

$$Y_{n+1} = Y_n + \frac{1}{6}(k_1 + 2k_2 + 2k_3 + k_4), \quad t_{n+1} = t_n + \Delta t$$

4.1.3 Test cases

In the following, some test cases to check the reliability of the proposed numerical scheme are shown.

In particular, the accuracy of the Laplace solver in terms of error behaviour as function of the domain discretization and the goodness of the free-surface evolution are presented. Further, with the intent of using stencils with a deformed shape, especially in the free-surface fixed mesh, an analysis of the stencil shape influence on the error has been performed. The convergence analysis, as well as the conservation of physical properties (of the system) as mass and energy, in a time evolving problem have been tested. Finally, the proposed free-surface method has been stressed with a problem regarding the focusing of a wave packet into a steep wave with the formation of a plunging breaker.

Convergence analysis for the HPC method

The two dimensional potential velocity problem for a linear wave is solved in a rectangular domain, $L \times H$, discretized with uniform spacing in both directions ($dx = dy$). The Dirichlet boundary condition is assigned on the upper side of the boundary, while on the remaining the Neumann boundary conditions are applied.

The analytical solution reads:

$$\phi(x, y) = \cosh(k(y + h)) \sin(kx) \quad (4.12)$$

where $k = 2\pi/\lambda$ is the wavenumber, h is the depth ($L/h = 40$, $kh = \pi$ and $kh = 1$).

For the blue case in fig. (4.4) ($kh = \pi$) the theoretical order of accuracy is confirmed, while an hyper-convergence is obtained for the red one ($kh = 1$). Similar behaviour is obtained for the derivative of the velocity potential.

The stencil-shape influence on the method accuracy has been tested by solving the same boundary value problem considering a restricted domain composed by only one stencil. Dirichlet boundary conditions are assigned on the eight boundary points and then, the stencil central point is the only unknown of the problem. For such point, velocity potential and its gradient have been compared with the analytical solution.

In figures (4.5) the stencil configurations and the L_2 -norm numerical errors are shown as function of a stretching parameter α , where $\alpha = 0$ identifies the ‘‘classic’’ square configuration. For the first test, the parameter α is the slope of the upper boundary of the stencil, i.e. the left and right upper nodes have been moved in asymmetric way only in vertical direction. The error behaviour shows a minimum value for the solution and for the derivative in y direction when the stencil is not deformed, while the error for the x -derivative

shows a minimum in a stretched configuration (dashed-circle). In the second test also the x -position of the upper right and left nodes has been changed. In this case, the minimum error is obtained for the “classic configuration” both for velocity potential and derivatives. The last test concerns the movement of all the boundary points. The error for the solution is quite constant for all the configurations, while for the derivatives, there is a large differences depending on the stencil shape. As for the first configuration, it is possible to find two stencil configurations, which minimize the error on the derivative ($\alpha = 0.3$ for $\partial(\times)/\partial y$ and $\alpha = 0.05$ for $\partial(\times)/\partial x$).

Periodic Fenton wave

To study the capability of the HPC method as well as the multi-mesh approach in the pure wave-propagation problem, a periodic problem has been implemented, avoiding in this way influences from wave generator and reflections from the downstream absorption zone. As a reference problem, the Fenton analytical solution for non-linear waves has been adopted [12] [31]. For the solution of the elliptic problem, the periodicity requires that the same values of the velocity potential on the two vertical boundaries of the domain are assigned, while Neumann and Dirichlet boundary conditions are assigned on the bottom and on the free-surface, respectively. The semi-Lagrangian formulation for kinematic and dynamic conditions on the free-surface is stepped forward in time with RK4 integration scheme. Waves with several steepness values have been tested, for each one the temporal behaviour of the code has been estimated through the control of different quantities as the mass, kinetic and potential energies, L_2 norm error for velocity potential on the free-surface

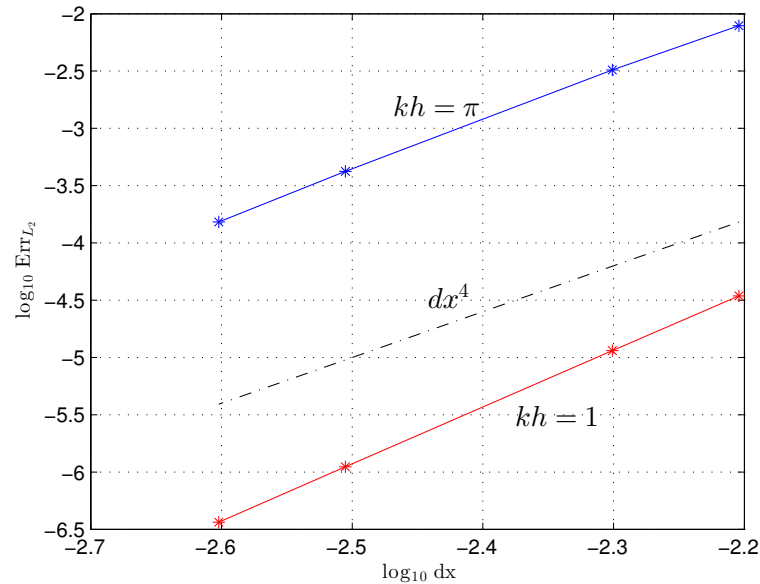


Figure 4.4. Boundary value problem for a linear wave solved in a rectangular domain. Convergence analysis of the error in norm L_2 in logarithmic scale. The continuous lines show the error behaviour for two waves with different kh . The dot-dashed line represents the theoretical trend dx^4 .

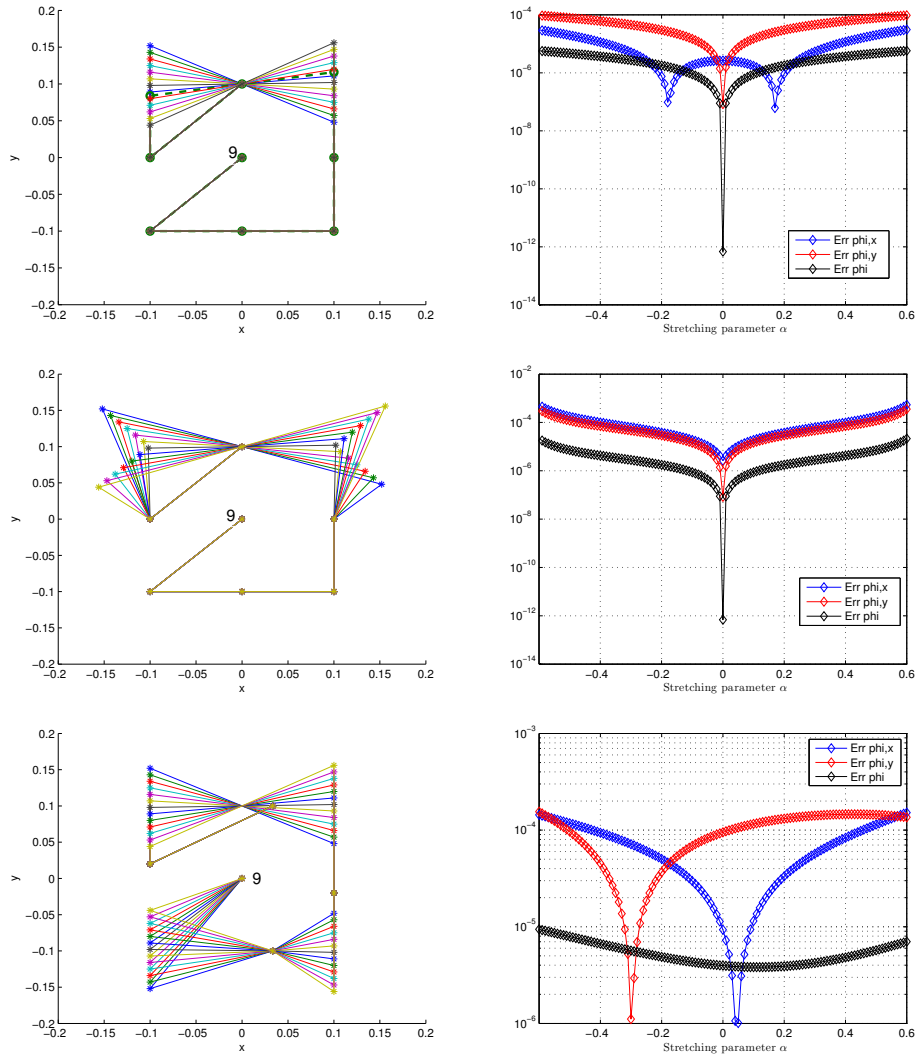


Figure 4.5. Boundary value problem for a linear wave solved within a stencil. L_2 error behaviour for velocity potential and derivatives as function of stretching parameter α (right column). Stencil spatial configuration with different parameter α (left column).

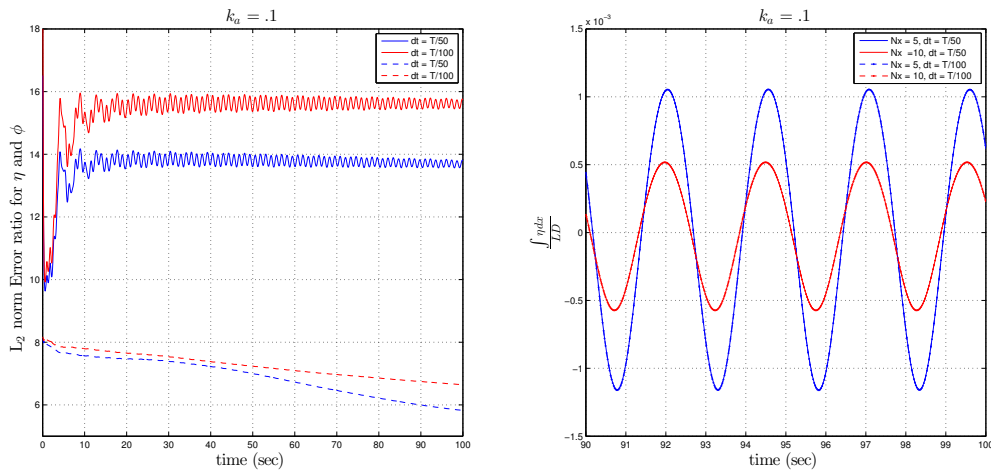


Figure 4.6. Initial boundary value problem for a periodic Fenton wave. Left plot: ratio between the L_2 norm error for velocity potential (dashed line) and free surface elevation (continuous line) for two different discretizations with different time steps. Right plot: temporal evolution for the mass of the system.

and wave elevation, and mean-max-min values for the free-surface.

To verify the convergence properties of the numerical method both for the time integration and spatial (HPC) schemes, the temporal evolution of the ratio between L_2 norm errors associated to two different computational grids with ratio 1:2, has been evaluated for velocity potential and free-surface elevation.

In the left plots of figure (4.6 - 4.7) the results for two different time steps are shown. The continuous line represents the free-surface and the dashed line the velocity potential. For a small wave steepness $k_a = 0.1$, the error for the free-surface elevation shows the expected behaviour. The error ratio tends to 16, which is the theoretical behaviour considering the 4th order accuracy of the schemes used for the time and space discretizations. The step from 14 to 16 moving from $dt = T/50$ to $dt = T/100$ shows that the error due to numerical integration prevails. A complete different behaviour is obtained for the velocity potential. The error decreases with the time step; for the coarser grid the error growth is slower than for the finer one (L_2 ratio decreases). In the right plot of figure (4.6 - 4.7) the temporal evolution of the mass system is shown. This is estimated as $\int_{free-surface} \eta(x) dx / L/D$, and only the values for the last 10 seconds of the simulation are reported. For all the cases an oscillatory behaviour is observed with the same period of the Fenton wave. No differences are observed for different time steps while moving from the coarser to the finer grid the values halve. For a higher steepness ($k_a = 0.3$) the behaviour of the mass is the same, its value decreases with the number of points used for the discretization and it is constant with the time step. The error ratio for the free surface is quite constant in time for the two times steps, its value is higher for the smallest dt but is quite far from the expected value of 16. Similarly as the for the case of $k_a=0.1$, the ratio for the velocity potential decreases with time and it is quite far from the expected value of 16.

Wave propagation - Wave maker and Sloshing

The last test case shown here is the propagation of a wave packet [10], which produces a very steep wave with a resulting plunging breaker. In this case both the effects of the wave-maker as well as the numerical beach at the end of the domain are included. The presence of a plunging breaker is useful to stress as much as possible the proposed method for the free-surface treatment.

The length of the wave tank is 25 m with a 5.5 m beach at the end and the depth is 0.6 m. The non-dimensional excursion and velocity of the piston wavemaker are defined as follows:

$$\bar{x}(\bar{t}) = \sum_i \bar{X}_i \sin(\bar{\omega}_i \bar{t} + \bar{\theta}_i)$$

$$\bar{u}(\bar{t}) = \sum_i \bar{U}_i \cos(\bar{\omega}_i \bar{t} + \bar{\theta}_i)$$

where $\bar{t} = \sqrt{g/h}$, $\bar{\omega} = \sqrt{h/g}$, $(\bar{x}, \bar{y}, \bar{\eta}) = (x, y, \eta)/h$ and $g = 1$. The fully Lagrangian formulation for the free-surface boundary conditions has been used with a re-interpolation of the Lagrangian markers every 10 time steps to avoid their clustering. A piecewise Hermite interpolation of 3th order is used [?]. To suppress wave reflections from the end of the tank a numerical beach has been implemented as in [14], where the damping coefficient is defined by a cubic function:

$$v(x^*) = \begin{cases} 0 & x^* < 0 \\ v_{max}(-2\zeta^3 + 3\zeta^2) & 0 \leq x^* < l_{beach} \end{cases}$$

Several wave probes were used to measure the wave elevation along the tank, the following figures show the comparison between the experimental and the numerical results computed with a BEM code [21] and with the proposed method.

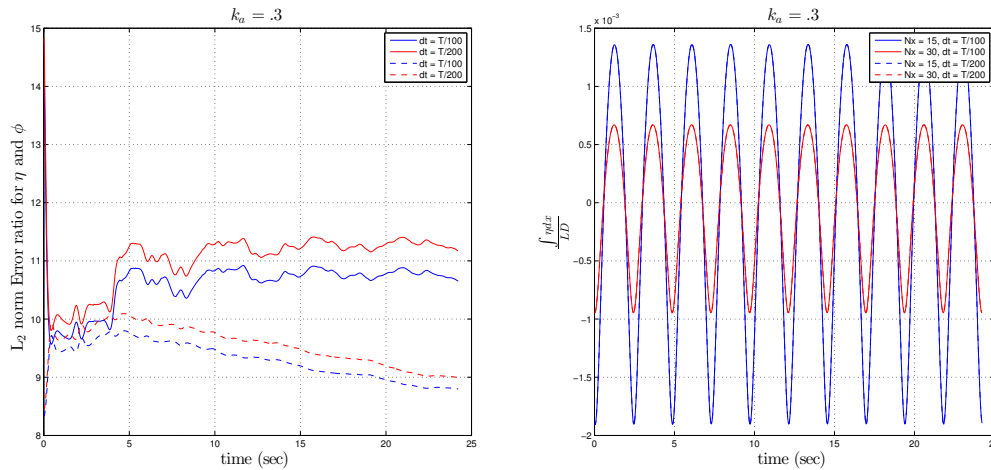


Figure 4.7. Initial boundary value problem for a periodic Fenton wave. Left plot: ratio between the L_2 norm error for velocity potential (dashed line) and free surface elevation (continuous line) for two different discretizations with different time steps. Right plot: temporal evolution for the mass of the system.

The parameter used for the discretization of the problem are:

$$N_x = 100; N_y = 40; N_s = 4N_x N_n = 9, dt = 0.01.$$

The wave geometry at the beginning of the plunging breaker formation is shown in figure (4.9). The blue dots are the computational nodes of the background mesh while the magenta stars are those of the free-surface mesh. The red vectors show the velocities of the Lagrangian markers on the free surface. Since the proposed method requires an adequate overlapping between the stencil of the two meshes, a strong stretching has been imposed to both of them. In particular, the small geometric characteristic of the plunging breaker, forces to increase the discretization on the tangential direction for the free-surface mesh, as well as, to reduce the thickness to avoid the exit of nodes from the physical domain. This, inevitably, leads to the stretching of the background mesh also. For the case in figure (4.9) the nodes have been organized following a cubic law, aiming to have their maximum density in proximity of the plunging breaker area. The wave configuration shown is the last instant of the simulation before the code breaks down.

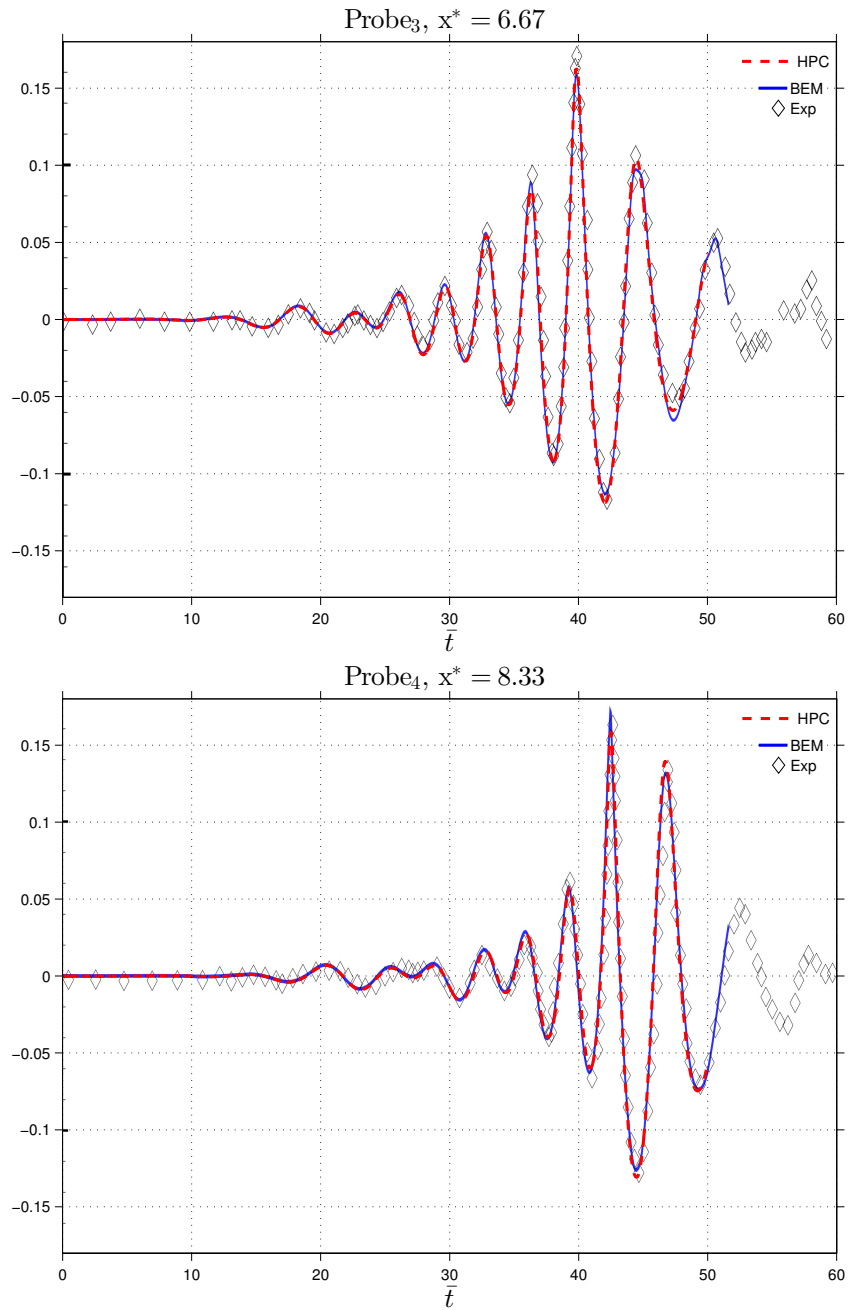


Figure 4.8. Wave-maker problem. Wave elevation comparisons for different wave probes between experiment (black marker), BEM (blue line) and HPC (dashed red line).

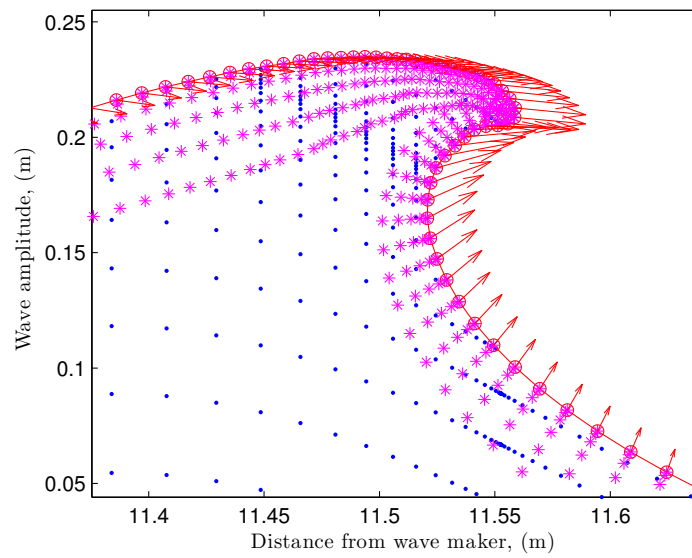


Figure 4.9. Wave-maker problem. Magnification of the plunging breaker formation area. The free-surface grid (magenta) and the background grid (blue) configurations are shown. The vectors represent the free-surface nodes velocities.

4.2 Fully hydroelastic model

In this section, the coupling of the numerical schemes discussed beforehand is presented, achieving in this way the fully hydroelastic numerical model. Here the model valid only for the case regarding the flip-through impact is presented where only the coupling between one-phase sloshing and structural sub-problems is considered.

In 3.16 the pressure p is expressed through the dynamic Bernoulli equation, giving:

$$M_B \ddot{w} + EI w^{IV} = -\rho \left(\frac{1}{2} |\nabla \phi|^2 + \frac{\partial \phi}{\partial t} - \mathbf{g} \cdot \mathbf{P} \right) \quad (4.13)$$

with \mathbf{g} gravity acceleration and \mathbf{P} the position of the fluid particles on the structure. This requires to know the value of the temporal derivative of the velocity potential, and since also this one satisfies Laplace equation an additional boundary value problem (b.v.p) must be solved.

In [15] the hydroelastic interaction has been evaluated by imposing two conditions: 1) the impermeability condition: $\frac{\partial \phi}{\partial n} = \frac{\partial w}{\partial t}$ and 2) the normal acceleration of the fluid particles which lie along the beam must be equal to the beam acceleration: $\mathbf{n} \cdot \frac{D\mathbf{u}}{Dt} = \frac{\partial^2 w}{\partial t^2}$. The first one is used as boundary condition for the b.v.p. for the velocity potential, while the second one gives an additional boundary condition for the b.v.p associated with its temporal derivative $\Delta(\partial \phi / \partial t) = 0$. From the last condition, assuming the linear beam theory, a non-homogeneous Robin condition is obtained:

$$\frac{\partial}{\partial n} \left(\frac{\partial \phi}{\partial t} \right) + \frac{\rho}{m} \frac{\partial \phi}{\partial t} = a_1(y) + a_2(y) \quad (4.14)$$

where ρ is the water density, m is the structural mass per unit length and width and a_1 and a_2 are known functions defined as:

$$a_1 = \frac{\partial w}{\partial t} \frac{\partial^2 \phi}{\partial \tau^2} - \frac{\partial \phi}{\partial \tau} \frac{\partial^2 w}{\partial y \partial t} \quad (4.15)$$

$$a_2 = -\frac{1}{m} \left(EI \frac{\partial^4 w}{\partial y^4} + \rho \frac{1}{2} |\nabla \phi|^2 - \rho \mathbf{g} \cdot \mathbf{P} \right) \quad (4.16)$$

A different approach is to estimate directly the pressure by solving the Poisson problem for p , which can be easily derived by taking the divergence of Euler's equations. For this aim the HPC method has been generalized for the solution of non homogeneous elliptic problem [4] (see Appendix A for more details). Also this approach it is characterized by a non-homogeneous Robin boundary condition due to the two conditions for the hydroelastic coupling

$$\Delta P = -2\rho (\phi_{xx} \phi_{yy} - \phi_{xy} \phi_{yx}) \quad (4.17)$$

$$\frac{\partial P}{\partial n} + \frac{\rho}{M_B} P = \frac{EI}{M_B} \frac{\partial^4 w}{\partial y^4} + \mathbf{g} \cdot \mathbf{n} \quad (4.18)$$

here n_1 represents the normal to the beam.

The interaction between fluid and structure is activated only when the characteristic time scales of hydrodynamic pressure are close to the structural ones. When the beam is

wetted by a slow rise up wave a quasi-steady approach can be used and the structure can be considered as rigid.

For each sub-step of RK4 scheme, first the velocity potential is calculated and the free-surface boundary conditions are updated, successively the b.v.p for $\partial\phi/\partial t$ is solved using the Robin boundary condition on the wetted part of the beam, a Neumann boundary condition along the rigid walls and the dynamic boundary condition as Dirichlet boundary condition for the free-surface. Once all the R.H.S terms of eq. (4.13) are known the structural modal coefficient $w_n(t)$ are calculated. To test the proposed hydroelastic method, the case of a beam in a fully wet condition under only the hydrostatic pressure, has been implemented. The middle point beam deflection in steady state condition has been compared with the results of analytical model considering both the dynamic and static cases (see fig. (4.10)). The blue line represents the dynamic evolution via the Euler beam analytical model, the green is the same of the blue using a ramp on the gravitational acceleration, avoiding in this way the oscillatory behaviour. The black line is the static solution while the magenta is the result from the fully-hydroelastic model. The comparison of the solution at steady state shows a good agreement between the different models.

4.2.1 semiAnalytic Flip-Through

In the following, the sloshing stage numerical simulation is used to initialize the semi analytical hydroelastic model for the flip-through impact. In particular, because in the model the impact is represented by a sort of water entry problem, information about the impacting wave velocity and position of the impact are required and for that, are extracted from the numerical simulation. Before to discuss the model and results, it is important to define the limitations of the proposed model for the reproduction of a flip-through impact effects. For this kind of impact, the main contribution to the hydrodynamic pressure exerted on the wall is the sudden high vertical acceleration (parallel to the structure) of the fluid at wall. In the proposed model, because it is borrowed from water entry problem, the main contribution is due to the fast deceleration (orthogonal to the structure) of the beam when hits the fluid. This assumption means that the complex kinematic and dynamic effects which characterize the flip-through are modelled in not proper way and not probably all of them are included in the modelling. This lead to say that this kind of model, at the moment, is not the most suitable for a flip-through impact. Different it is the situation when a gas cavity is present during the impact where the kinematic and dynamic effects are more similar to the ones of a water entry problem. The formulation of the analytical model follows the steps covered in case of impact with entrainment of a gas cavity, but differently from that, here the cavity length is set equal to zero. An additional step added for the flip-through model with respect to the cavity is the time dependence of the water depth, $h = h(t)$. Such temporal dependency must be considered, not as a real temporal evolution but more as a sequence of steady state conditions, i.e. the hypotheses of flat free surface is still considered at each time step.

The resulting system of equations is

$$M_{mn}\ddot{w}_n(t) + C_{mn}\dot{w}_n(t) + K_{mn}w_n(t) = -M_{add_{mn}}(t)\ddot{w}_n(t) - C_{add_{mn}}(t)\dot{w}_n(t) - F_{g1_m}(t)\dot{V}(t) - F_{g2_m}(t)V(t) \quad (4.19)$$

where M_{mn} , C_{mn} and K_{mn} , in the left hand side, are the mass, damping and stiffness matrices respectively obtained for the modal decomposition of the beam deflection, while, in the right hand side, $F_{g1}(t)$ and $F_{g2}(t)$ are generalized force coefficients and $M_{add_{mn}}(t)$ and $C_{add_{mn}}(t)$

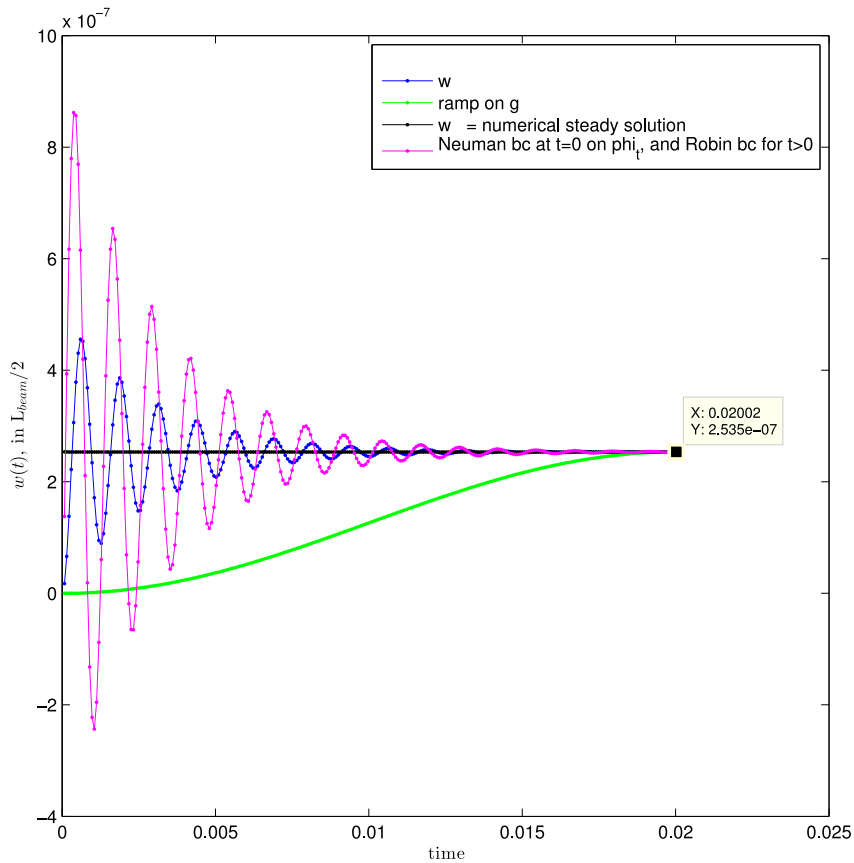


Figure 4.10. Comparison of deflection for a beam under hydrostatic pressure. The blue line represents the dynamic solution using the Euler beam model. For the green one always the Euler beam model has been used but a ramp function on gravitational acceleration g to avoid the impulsive start of the problem. The black line represents the solution for the static problem. The magenta line represents the solution for the fully-hydroelastic problem.

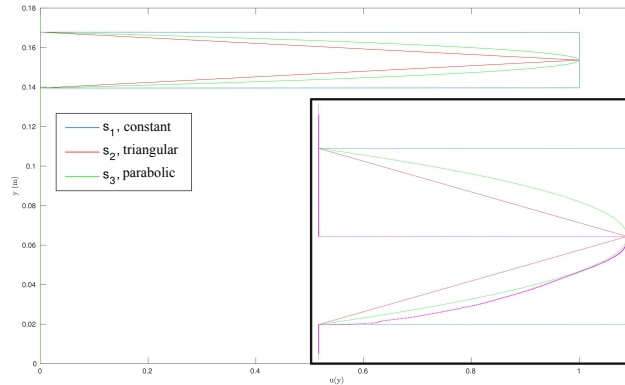


Figure 4.11. Vertical distributions of the impact horizontal velocity in the three considered cases. The values are made dimensionless with the maximum horizontal velocity. The beam is located between 0.125 m to 0.215 m. In the bottom left black box an enlarged view of the velocity profiles is reported.

are the added mass and added damping matrices. Take in account the time dependence of the water depth gives the additional terms $C_{add,mn}(t)$ and $F_{g2}(t)$. It is to be noted as the first one is a damping term which increases the effects of the structural one. The second one contributes to an additional forcing term. From the comparison of the two forcing term, proportional respectively to $h(t)\dot{V}(t)$ and to $\dot{h}(t)V(t)$, the first one results the most influential. To obtain the input parameters from the kinematic and dynamic configurations of the impacting wave, the numerical simulation has been stopped at the end of the advancement stage, just before the focusing. From the kinematic configuration the position of the impact and the length of the impact area have been identified. The elevation of the wave crest has been selected as vertical position for the impact and its area has been set as twice the wave height. From the dynamic configuration, the horizontal velocity component of the advancing wave from the trough until the crest is used to define the different impact velocity profile (fig. (4.11)). Three vertical shapes considered for the velocity are: s_1 a constant value based on the maximum value of horizontal velocity (blue), s_2 triangular, where the maximum is reached at the wave crest, s_3 parabolic, always with the maximum at wave crest. In the black box an enlargement view of the profiles is shown, it is also added the horizontal component of velocity obtained with the numerical simulation, marked by magenta dots. It's worth to note how the better approximation of numerical result is given by the parabolic profile. Must be say that, while the horizontal velocity will remain more or less the same until the impact, the wave front height will decrease moving toward the focusing instant and hence, the hydrodynamic load will be more concentrated in space than the modelling one. In fig. (4.12) the comparison between the strain gauges is presented. The different colours represent the structural responses associated to the analysed forcing terms in accord with the description reported for fig. (4.11). The black dashed line is the value recorded during experiments. Looking at the first peak, the triangular profile s_2 has a better agreement with

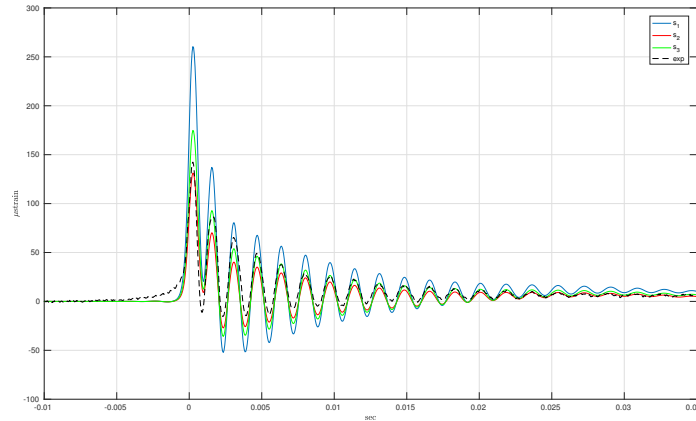


Figure 4.12. Comparison of the strain gauges evaluated in the middle of the structure. The colours identify the different vertical velocity profile. (blue - constant, red - triangular, green - parabolic, dashed black line experiment)

the experiment, while the constant s_1 and parabolic s_3 profiles show an overestimation of the beam deflection. The result of the constant profile gives overestimation also in the successive temporal instants, while for the triangular and the parabolic, the beam amplitude oscillations are comparable with the experiment. The main error can be ascribed to an input load not well reproduced. Looking at the instantaneous oscillation frequency, the agreement with experiment is satisfactory, highlighting a good choice for the water depth temporal evolution. In fig. (4.13), the temporal evolution for water depth and impact acceleration are reported. On the left axis, the curve represents the water depth. For the first part, from a fully dry condition up to the point of impact ($t=0$), a parabolic law has been used. Then the trend is assumed linear with a slope which decrease after the fully wet condition. On the right axis, the impact acceleration is reported. The acceleration profile has been designed following the temporal behaviour of the impact pressure for the case of impact against a rigid wall (see fig. (2.8)).

$$\dot{V}(t) = \begin{cases} \frac{V_{max}e^{-t/t_a}}{(1+e^{(-t/t_a)})^2 t_a} & t \leq 0 \\ \frac{V^* e^{-t/t_s}}{(1+e^{(-t/t_s)})^2 t_s} + \frac{C}{(1-t)^2} - D(2t-1) & t > 0 \end{cases} \quad (4.20)$$

where V_{max} is the wave crest velocity calculated from numerical simulation and equal to -2.3 m/s , t_a is a characteristic time scale which define the rise time of the first peak. In the second equation, t_s is a time scale which define the decrease of acceleration, in fact the peak is not symmetric with respect to its maximum value. It has been set equal at $3.5t_a$, while the parameter V^* and C are obtained imposing the continuity of velocity and acceleration at $t=0$. The parameter D keep into account the almost flat part of the acceleration after the peak. It as been set equal $V_{max}/4/t_a/30$, where $V_{max}/4/t_a$ is the maximum value of the acceleration. The value of 30 has been chosen by the analysis of the experimental pressure during the impact on rigid wall, considering the pressure ratio between the maximum value and the almost flat segment, for the pressure transducer closest to the impact region. Even if the comparison between the beam deflection shows some differences, anyway with a proper setting of the model parameters, it is possible to obtain results which can useful to get some

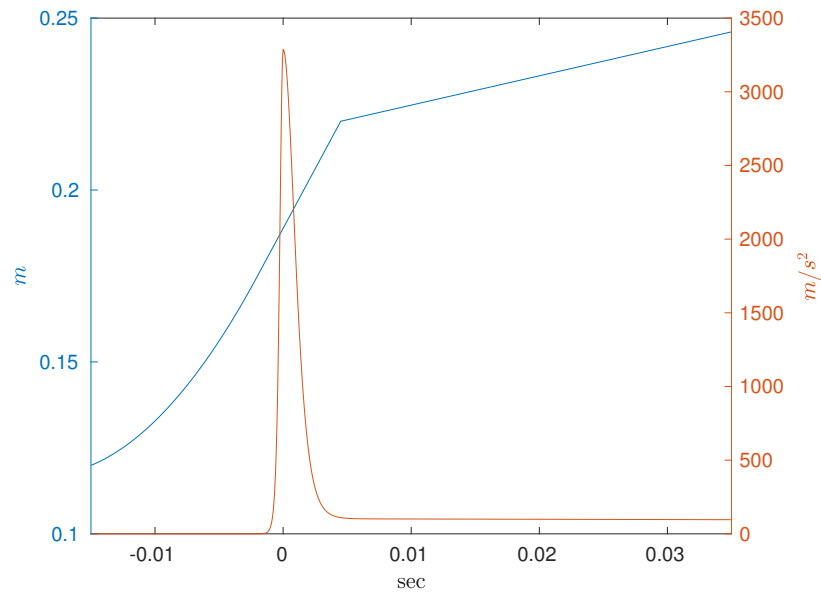


Figure 4.13. Left axis: temporal evolution for the water depth. Right axis: temporal evolution for impact acceleration.

informations about the structural response, i.e. magnitude of structural stress, dynamic behaviour of the structure (frequency and damping). But if we look at the hydrodynamic pressure in a location far from the structure the limitation of the model appears more evident. In fig. (4.14) the comparison of the hydrodynamic pressure, for a probe located about $0.1 m$ below the lower bottom of the structure, is reported. As for fig. (4.12) the different colour refer to the three velocity profile tested and the dashed black line to experimental results. It is easily to observe as the hydrodynamic pressure is overestimated for all the cases, both in the first peak and also for all the successive oscillations. Also the damping has a completely different behaviour. It is also possible to observe that the first peak occurs before than in the experiment. This large differences are consequences of the impact modelling. The spatial profile for velocity potential, obtained via a vortex distribution along the vertical wall, loses of accuracy, with respect the physical event, moving away from the impact area.

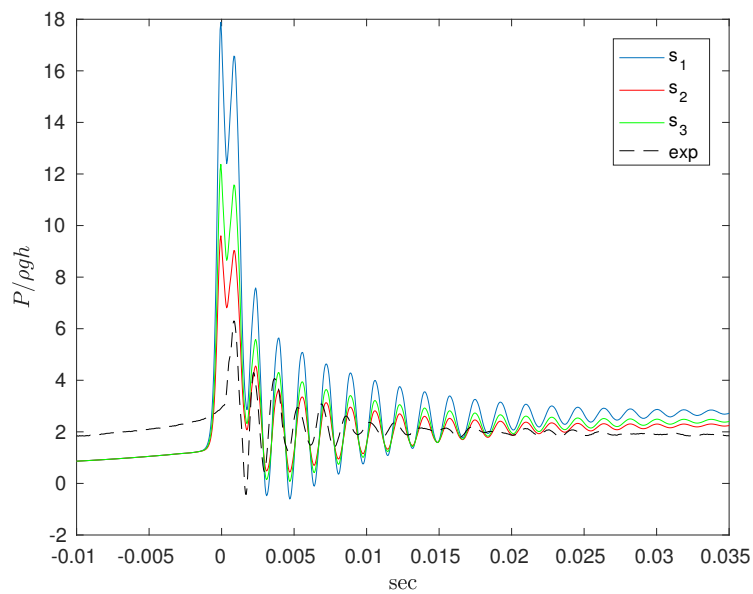


Figure 4.14. Comparison of hydrodynamic pressure for a probe located at 0.025 m from the tank bottom. Blue line s_1 constant spatial velocity profile, red line s_2 triangular spatial velocity profile, green line s_3 parabolic spatial velocity profile and dashed black line experimental results.

Chapter 5

Conclusions

The investigation of the hydroelastic phenomena during wave impact events on the vertical side wall of a two dimensional sloshing tank has been the main objective of this work. The experimental activity, as well as semi-analytical and numerical modeling, have been the tools used in order to understand the main physical features which drive the phenomenon.

An *ad-hoc* experimental set-up has been designed to reproduce repeatable wave impact events against a deformable aluminium plate installed on a vertical wall of the tank. Concurrently with the geometrical characteristics of the tank, the excitation signal used for the tank motion helps to achieve a good repeatability of the events. The effects of two different wave impact typologies have been investigated: the flip-through and the impact with a single gas-cavity entrainment. The choice of these two typologies of wave impacts has been driven by their characteristic time scales which can be quite close to the structural ones and hence able to trigger hydroelastic phenomena. For the structural stress estimation, differently from the usual approach, which consists of the measurement of hydrodynamic pressure, here the structure deflection has been measured with the use of strain gauges.

In the time evolution of the flip-through impact three different stages have been identified: in the *advancement stage* the structure is stressed by the slow rise up of the wave through along the wall and the load applied is proportional to ρgh , with h the filling depth. Next, moving to the *focusing* and *flip-through* stages, due to the strong vertical acceleration and sudden turning of the flow the *fully hydroelastic* stage is triggered. The rise time of the hydrodynamic pressure is comparable with the highest natural periods of the wetted deformable structure and then the corresponding natural modes of vibration are excited. During this stage, whose duration can be quantified in about 5/6 ms, the hydrodynamic pressure is strongly influenced by the motion of the structure and it is characterized by an oscillatory behaviour with the same frequency of the structure. The structural wetted natural frequencies decrease in time as consequence of the added-mass effect growth due to the increase of the structural wetted length. In the last stage, called *free-vibration*, the behaviour of a free-oscillating system characterizes the temporal evolution of the structure. By comparing the maximum value of hydrodynamic pressure between impact on rigid and elastic wall, it is possible to assert that the structural reaction increases the maximum value of the hydrodynamic pressure. A hybrid hydroelastic model has been developed for the reproduction of the wave impact only. The hydrodynamic pressure has been considered as superposition of a pressure field measured during the experiments on rigid wall and a vibrational pressure solutions of the hydroelastic problem for a vibrating beam around a

rest state. Using the images recorded with a fast-cam to evaluate the instantaneous wetted length of the structure and a structural damping which changes with the wetted length, obtained experimentally with impulsive test hammer in calm water, the model gives results in quite good agreement with the experiments especially in terms of oscillation frequency and damping. The model shows an underestimation in the *fully hydroelastic* stage regarding the stress amplitude and a good agreement in the subsequent one, highlighting that the hydroelastic interaction is greater than that predicted by a weakly-coupled model.

The impact with the entrainment of a single gas-cavity shows some differences with respect to the flip-through case. The system behaves more like a forced oscillating system where the gas cavity is the forcing: the gas-cavity is compressed at the wall by the surrounding water at the instant of the impact, due to the compressibility effects, it starts oscillating with its natural frequency and this behaviour is reflected on the structural stress. Anyway, for the small and medium size cavity the rise time of the pressure is such to excite the structural natural modes and this is evident in the stress signal just after the first peak. Such oscillations appear clearly for ullage pressure lower than 200 mbar. The effects of hydroelastic interaction can be observed in comparison with the results of experiments against rigid wall. For the cited cases, small and medium size cavity, the interaction with the deformable structure entails a decrease of the cavity natural frequencies and of the pressure signals damping coefficient. The differences between rigid and elastic case, hence the hydroelastic effects, decrease with the ullage pressure because of the increase of the distance between the two characteristic time scales. Starting from the works in [11], [2] a semi-analytical model which takes into account the non-linear dynamics of the gas cavity and of the hydroelastic problem has been developed. The non-linear frequencies of the oscillating gas cavity have an important role especially in case of low ullage pressure and may assume values close to the structural natural frequencies. The analysis of the hydroelastic natural frequencies shows, as observed in the experimental case, a reduction of the first natural frequency and damping, for the gas cavity, with respect to the case of uncoupled problem, even if the reduction is lower than in the experiments. Though the presented analytical model shows a quite good agreement with the experiment results, the simplifying hypotheses adopted are still too limiting. For a better description of the problem the flow kinematic, the free-surface evolution and a proper modelling of damping and thermal effects inside the cavity have to be taken in account. In the last part of the work, the tools for the numerical treatment of the hydroelastic problem have been implemented. A relatively new, highly accurate and efficient, field method for potential-flow problems, the HPC, has been adopted for the fluid-dynamic sub-problem and fully coupled with an Euler beam equation for the structure sub-problem. In the numerical context, important novel contributions of this research have been the proposal of multi-grid approach to handle very steep waves propagation and the extension of the HPC method to the solution a Poisson problem. The latter is given in detail in Appendix A and opens to a genuinely new strategy for the numerical solution of viscous-flow problems involving the Poisson equation for the pressure.

5.1 Suggestions for future activities

Possible suggestions for a future activities are:

- Experimental activities to investigate the thermal effects as source of damping for the

gas cavity impact problem.

- Experimental investigation on possible cavitation phenomena always in the gas cavity problem at low Cavitation Number.

Appendix A

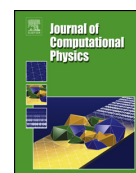
Generalized HPC method for the Poisson equation



Contents lists available at ScienceDirect

Journal of Computational Physics

www.elsevier.com/locate/jcp



Generalized HPC method for the Poisson equation

A. Bardazzi^{a,b}, C. Lugni^{a,c,*}, M. Antuono^a, G. Graziani^b, O.M. Faltinsen^c^a CNR-INSEAN, National Research Council-Marine Technology Institute, Via di Vallerano 139, 00128 Roma, Italy^b University of Rome 'Sapienza', Dept Aeronautical & Mechanical Engn., Via Eudossiana 1, 00184 Rome, Italy^c Centre for Autonomous Marine Operations and Systems (AMOS), Department of Marine Technology, NTNU, Trondheim, Norway

ARTICLE INFO

Article history:

Received 16 January 2015

Received in revised form 14 June 2015

Accepted 4 July 2015

Available online 20 July 2015

Keywords:

Harmonic polynomial cell

Elliptic boundary value problem

Poisson solver

Convergence analysis

ABSTRACT

An efficient and innovative numerical algorithm based on the use of Harmonic Polynomials on each Cell of the computational domain (HPC method) has been recently proposed by Shao and Faltinsen (2014) [1], to solve Boundary Value Problem governed by the Laplace equation. Here, we extend the HPC method for the solution of non-homogeneous elliptic boundary value problems. The homogeneous solution, i.e. the Laplace equation, is represented through a polynomial function with harmonic polynomials while the particular solution of the Poisson equation is provided by a bi-quadratic function. This scheme has been called *generalized HPC method*. The present algorithm, accurate up to the 4th order, proved to be efficient, i.e. easy to be implemented and with a low computational effort, for the solution of two-dimensional elliptic boundary value problems. Furthermore, it provides an *analytical* representation of the solution within each computational stencil, which allows its coupling with existing numerical algorithms within an efficient domain-decomposition strategy or within an adaptive mesh refinement algorithm.

© 2015 Elsevier Inc. All rights reserved.

1. Introduction

Elliptic Partial Differential Equations, associated with boundary value problems (time independent) rather than with evolution problems, are quite common in many fields of physics such as: heat flow, electrostatic and gravitational potential, potential flow, static elasticity and quantum mechanics. The generic elliptic operator L can be expressed as:

$$Lu = - \sum_i^n \sum_j^n a_{ij}(x) \frac{\partial^2 u}{\partial x_i \partial x_j} + \sum_i^n b_i(x) \frac{\partial u}{\partial x_i} + c(x)u = f(x) \quad (1)$$

where the coefficients a_{ij} are the elements of a positive-definite matrix [2].

If the Navier–Stokes equation for an incompressible fluid is numerically time integrated by Chorin's projection method [3], there a Poisson equation for the pressure appears. The Poisson equation, which comes from (1) with $a_{ij} = \delta_{ij}$, $b_i = c = 0$, is used in many applications in fluid dynamics, as for the pressure calculation in incompressible flow or for the velocity calculation in a 2D incompressible and viscous fluid, where a Poisson equation relates the stream function and the vorticity field. From the numerical point of view, the solution is achieved in two steps consisting in the discretization of the

* Corresponding author at: CNR-INSEAN, National Research Council-Marine Technology Institute, Via di Vallerano 139, 00128 Roma, Italy; AMOS-NTNU, NO-7491 Trondheim, Norway.

E-mail addresses: bardazzi.andrea@gmail.com (A. Bardazzi), claudio.lugni@cnr.it (C. Lugni), matteo.antuono@cnr.it (M. Antuono), g.graziani@uniroma1.it (G. Graziani), Odd.Faltinsen@ntnu.no (O.M. Faltinsen).

<http://dx.doi.org/10.1016/j.jcp.2015.07.026>

0021-9991/© 2015 Elsevier Inc. All rights reserved.

Table 1
Computational burden of direct and indirect methods for the solution of algebraic system (from [6]).

Algorithm	Oper.	Memory
Dense LU	N^3	N^2
Band LU	N^2	$N^{3/2}$
Sparse LU	$N^{3/2}$	$N \log(N)$
Jacobi	N^2	N
SOR	$N^{3/2}$	N
Conj. Grd	$N^{3/2}$	N
GMRES	N	N
Multigrid	N	N

continuous system (first step), and in the solution of the discretized system (second step). Because of the fine discretization necessary to properly describe the smallest scales involved in the physical phenomenon, the computational effort for the solution of the Poisson equation can be an issue. The number N of points, indeed, influences the computational cost of the algorithm, both in terms of required computational time and memory (see Table 1). This becomes even more critical when the elliptic equation is part of an evolution problem, i.e. if the pressure distribution must be calculated at each time step, which requires an efficient solution of the elliptic boundary value problem.

Several approaches are used for the discretization of the elliptic BVP. The most common are finite difference methods (FDM), finite volume methods (FVM) and the Finite Element Methods (FEM) [3,4]. FDM makes a finite difference approximation of the derivatives; FVM first reformulates the problem via its integral form and then approximates the integral equation on each control volume. With respect to FDM, FVM provides a solution of the weak form of a differential problem, which includes also the treatment of the discontinuous solutions. The most used implementation of such methods yields 2nd order accurate schemes, because of the difficulties in building high-order approximation schemes. Although a fine discretization of the computational domain is still required to capture the smallest scales of the phenomenon, a high-order solver allows for using a lower number of computational points with respect to a low-order solver, in order to ensure a similar accuracy.

The finite element method, which is capable of handling general domains, is quite difficult to use for the solution of elliptic BVP. It is based on the use of shape functions on each element of the computational domain. Galerkin method is then used to determine the coefficients of the shape function, requiring the integrals to be calculated on each element.

All the mentioned methods lead to a linear algebraic system $AU = X$; depending on the feature of the coefficient matrix A , a proper technique can be used to solve the system (see Table 1).

The direct methods (e.g. Gauss Elimination, LU decomposition), which give an exact solution of the system, are suited in case of small algebraic systems [5].

The indirect or iterative methods (e.g. Jacobi, Gauss–Seidel, Thomas algorithm, SOR, ADI, GMRES) are based on a sequence of approximations that converge to the exact solution (see [5]) and are indicated for large algebraic system. Furthermore, they can be easily parallelized.

Recently, a new numerical algorithm has been proposed by Shao and Faltinsen [1,7], to solve Boundary Value Problem governed by the Laplace equation. The method, based on the use of Harmonic Polynomials on each Cell of the computational domain (HPC method), is 4th order accurate in space and it has been successfully applied to solve several problems of concern in marine hydrodynamics [1].

The present paper proposes an extension of the HPC method to the solution of elliptic boundary value problems. The method is based on the use of a polynomial function with harmonic polynomials representing the homogeneous solution and a bi-quadratic function representing a particular solution of the Poisson equation. Hereinafter this is called *generalized HPC method*. The algorithm, accurate up to the 4th order, is here proved to be efficient for the solution of two-dimensional elliptic boundary value problem. The generalization to the three dimensional case, though straightforward, is an ongoing activity.

It is worth to point out that the method, although here applied to prototype elliptic problems, can be useful for the solution of the pressure field in incompressible flows governed by the Navier–Stokes equations, within a projection method [3].

The main advantage of the method with respect to the classical field methods (e.g. FDM, FVM, FEM) consists in the high accuracy with a relatively low computational effort, which means easy implementation and efficient evaluation of the numerical solution. Moreover, it provides an *analytical* representation of the solution within each stencil, making straightforward its coupling with existing numerical algorithms within an efficient domain-decomposition strategy.

Because of these features, it is conceivable to use the present method in an efficient way within an adaptive mesh refinement strategy. In particular, the pressure field (governed by the Poisson equation) can be first evaluated, with a 4th order accuracy, on a Cartesian coarse grid using the present solver. Then, the pressure may be interpolated (using the continuous representation of the solution within each stencil) on a refined mesh which is fitted to the flow field, where the velocity field can be achieved through a classical field method.

However, the final goal is the use of the generalized HPC to solve fluid dynamic problems, where the Navier–Stokes equations are solved by a projection method [3].

The above mentioned research topics are ongoing activities of the present research group.

2. Mathematical formulation

Let us consider the Poisson problem in the fluid domain Ω with either Dirichlet or Neumann conditions prescribed over different and exclusive portions of the domain boundaries $\partial\Omega_D$ and $\partial\Omega_N$ respectively:

$$\begin{cases} \Delta u(\mathbf{x}) = \sigma(\mathbf{x}), & \text{in } \Omega \\ u(\mathbf{x}) = g_D(\mathbf{x}), & \text{on } \partial\Omega_D \\ \frac{\partial u(\mathbf{x})}{\partial n} = g_N(\mathbf{x}), & \text{on } \partial\Omega_N \end{cases} \quad (2)$$

where the forcing $\sigma(\mathbf{x})$ is assumed to be known. The solution $u(\mathbf{x})$ is expressed as the sum of two functions:

$$u(\mathbf{x}) = \tilde{u}(\mathbf{x}) + \bar{u}(\mathbf{x}) \quad (3)$$

where $\tilde{u}(\mathbf{x})$ is a particular solution of the Poisson equation

$$\Delta \tilde{u}(\mathbf{x}) = \sigma(\mathbf{x}) \quad (4)$$

and $\bar{u}(\mathbf{x})$ is a harmonic function which satisfies the homogeneous BVP

$$\begin{cases} \Delta \bar{u}(\mathbf{x}) = 0, & \text{in } \Omega \\ \bar{u}(\mathbf{x}) = g_D(\mathbf{x}) - \tilde{u}(\mathbf{x}), & \text{on } \partial\Omega_D \\ \frac{\partial \bar{u}(\mathbf{x})}{\partial n} = g_N(\mathbf{x}) - \frac{\partial \tilde{u}(\mathbf{x})}{\partial n}, & \text{on } \partial\Omega_N \end{cases} \quad (5)$$

Note that the above decomposition (3), as well as the following solution scheme, can be easily extended to problems where Robin condition holds in a part of the domain boundary.

According to the HPC methodology [1], the harmonic function $\bar{u}(x, y)$ is approximated through a series of harmonic polynomials. These form a complete harmonic functional basis in the star-shaped domains relative to the origin [8–10].

For the 2-dimensional case, they come from the linear combination of the real and imaginary part of the complex harmonic polynomials $z^n = (x + iy)^n$, i.e. for $n \leq 4$:

$$\begin{aligned} \bar{u}(x, y) &= a_1 + a_2x + a_3y + a_4(x^2 - y^2) + a_5(2xy) + \\ &\quad + a_6(x^3 - 3xy^2) + a_7(3x^2y - y^3) + a_8(x^4 - 6x^2y^2 + y^4) = \\ &= a_i \bar{f}_i(x, y), \quad \text{with } i = 1, \dots, 8, \end{aligned} \quad (6)$$

where the repeated index implies summation. In the 3-dimensional case, the harmonic polynomials arise from the spherical harmonic functions, i.e. the solution for the 3D Laplace equation in spherical coordinates.

The forcing term $\sigma(x, y)$ is approximated through a bi-quadratic interpolation. In the 2D case, this reads:

$$\begin{aligned} \sigma(x, y) &\approx (\alpha_0 + \alpha_1x + \alpha_2x^2)(\beta_0 + \beta_1y + \beta_2y^2) = \\ &= c_1 + c_2x + c_3y + c_4x^2 + c_5xy + c_6y^2 + c_7x^2y + c_8xy^2 + c_9x^2y^2 = \\ &= c_j h_j(x, y), \quad \text{with } j = 1, \dots, 9. \end{aligned} \quad (7)$$

A particular solution of the Poisson equation (4), suitably approximated through $\Delta \tilde{u}(x, y) \approx c_j h_j(x, y)$, is:

$$\begin{aligned} \tilde{u}(x, y) &\approx c_1 \frac{x^2 + y^2}{4} + c_2 \frac{xy^2}{2} + c_3 \frac{x^2y}{2} + c_4 \frac{x^4}{12} + c_5 \frac{x^3y + xy^3}{12} + \\ &\quad + c_6 \frac{y^4}{12} + c_7 \frac{x^4y}{12} + c_8 \frac{xy^4}{12} + c_9 \frac{x^4(-x^2 + 15y^2) + y^4(-y^2 + 15x^2)}{360} = \\ &= c_j g_j(x, y), \quad \text{with } j = 1, \dots, 9. \end{aligned} \quad (8)$$

As a consequence, the solution of the problem (2) is:

$$\begin{cases} u(x, y) = a_i \bar{f}_i(x, y) + c_j g_j(x, y), & \text{with } i = 1, \dots, 8, j = 1, \dots, 9. \\ \sigma(x, y) = c_j h_j(x, y), & \text{with } j = 1, \dots, 9. \end{cases} \quad (9)$$

The system (9), which enables the interpolation of the solution, must be collocated on each cell of the computational domain in order to achieve the linear system associated with the BVP and to find the unknown coefficients a_i .

Note that the approximation of the forcing term through a bi-quadratic interpolation is just one of the possible strategies that may be used. Indeed, different approaches for representing $\sigma(x, y)$ can be adopted, each one originating a different class of methods for the solution of the non-homogeneous elliptic BVP.

A fundamental issue concerns the use of analytical functions to represent the solution. In the generalized HPC algorithm, the solution is analytic because of the polynomial functions used for the solution of the homogeneous problem and the

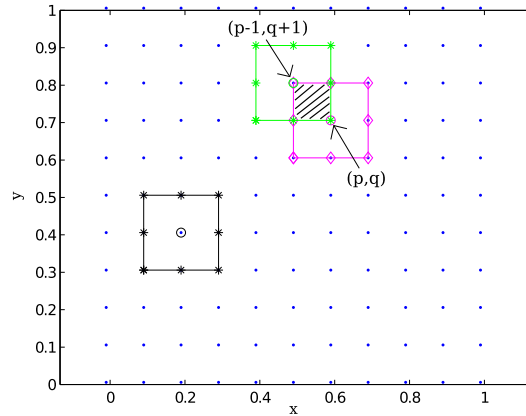


Fig. 1. Discretization of a square domain $\Omega = (0, 1) \times (0, 1)$. The small dots are the computational points, while the bold symbols represent the border of a generic stencil. The dashed area is the overlapped region of two stencils.

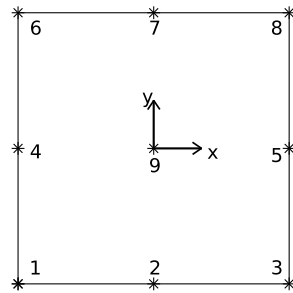


Fig. 2. Detail of the stencil associated to node 9 (black circle in Fig. 1).

interpolation functions adopted for the particular solution of the non-homogeneous problem. This implies that the HPC solver cannot capture singular solutions of the Laplace equation (e.g. in a domain with a sharp corner [11], or at the intersection between the free surface and the tank wall when it is non-vertical at the waterline [12] and the free-surface condition is linear). A strategy consists in matching an inner non-analytical solution for the singularity and an outer solution through the HPC solver. A similar approach could be used when the singularity occurs in the forcing term. In this case the matching between inner and outer domain only concerns the interpolation of the forcing term.

3. Numerical formulation

Let the 2D fluid domain Ω be composed by a finite number of computational points (Fig. 1). A “direct numerical dependence” domain (or stencil) is associated with each point in Ω . Specifically, the stencil is composed by the eight closest nodes (Fig. 2).

Each point (p, q) of the grid is, at the same time, the center node of the stencil (p, q) and a boundary node of the closest stencils (e.g. $(p - 1, q + 1)$, $(p - 1, q)$ and so on, see Fig. 1); that is, an overlapping grid system is used.

The collocation of the equation system (9) on the stencil (p, q) enables evaluating the coefficients a_i , c_j as a function of the unknown solution u_m and of the known forcing term σ_k . In particular, by collocating the forcing term (second equation of (9)) on the nine nodes (x_k, y_k) of the stencil ($k = 1, \dots, 9$ see Fig. 2), provides the coefficients c_j :

$$\sigma_k = h_{kj} c_j \Rightarrow c_j = h_{jk}^{-1} \sigma_k, \quad j, k = 1, \dots, 9. \tag{10}$$

Similarly, the first equation of (9) collocated on the eight boundary nodes (x_m, y_m) of the stencil ($m = 1, \dots, 8$ see Fig. 2) gives an explicit equation for the unknown coefficients a_i :

$$u_m = \bar{f}_{mi} a_i + g_{mj} c_j \Rightarrow a_i = [\bar{f}^{-1}]_{im} (u_m - g_{mj} c_j) \quad i, m = 1, \dots, 8; \quad j = 1, \dots, 9 \tag{11}$$

By substituting eqs. (10) and (11) in (9), the solution of the Poisson BVP can be written as:

$$u(x, y) = \bar{f}_i(x, y)[\bar{f}^{-1}]_{im}(u_m - g_{mj}[h^{-1}]_{jk}\sigma_k) + g_j(x, y)[h^{-1}]_{jk}\sigma_k, \\ i, m = 1, \dots, 8; \quad j, k = 1, \dots, 9. \quad (12)$$

Equation (12) enables evaluating the solution as a continuous function inside each stencil. In any case, the uniqueness of the solution is ensured only at the grid points. In fact, from eq. (12) the representation of the solution $u(x, y)$ at a generic point of the continuous field that does not belong to the grid differs by considering two different stencils overlapped in (x, y) (see the dashed area in Fig. 1).

The derivatives of the solution can be then easily obtained as:

$$\frac{\partial u(x, y)}{\partial x} = \frac{\partial \bar{f}_i(x, y)}{\partial x}[\bar{f}^{-1}]_{im}(u_m - g_{mj}[h^{-1}]_{jk}\sigma_k) + \frac{\partial g_j(x, y)}{\partial x}[h^{-1}]_{jk}\sigma_k, \quad (13a)$$

$$\frac{\partial u(x, y)}{\partial y} = \frac{\partial \bar{f}_i(x, y)}{\partial y}[\bar{f}^{-1}]_{im}(u_m - g_{mj}[h^{-1}]_{jk}\sigma_k) + \frac{\partial g_j(x, y)}{\partial y}[h^{-1}]_{jk}\sigma_k, \quad (13b)$$

with $i, m = 1, \dots, 8$, and $j, k = 1, \dots, 9$.

Equations (12) or (13) are necessary to build the global linear equation system. At the point of the domain where the solution is unknown, equation (12) is evaluated in the center of the stencil; at the point of the boundary, depending on the assigned Dirichlet or Neumann boundary condition, eqs. (12) or (13), respectively, are evaluated at the boundary of the stencil. In both cases, the linear algebraic equation that is obtained from the "collocation" on each stencil is

$$b = F^T \underline{u} - G^T \underline{\sigma} \quad (14)$$

where $F, \underline{u}, G, \underline{\sigma}$ are nine components vectors, and b contains the boundary data.

The collocation on each point of the domain, gives the following global system:

$$B = \mathbb{F}U - \mathbb{G}\Sigma \quad (15)$$

$$U = \mathbb{F}^{-1}(B + \mathbb{G}\Sigma) \quad (16)$$

Once the solution is known on the computational nodes, it is possible to interpolate the continuous solution on a generic point of the physical domain:

$$u(x, y) = \mathbb{F}(x, y)U + \mathbb{G}(x, y)\Sigma \quad (17)$$

which derives from eq. 12 with the single elements of the matrices given by

$$\mathbb{F}_{nm} = \bar{f}_i(x_n, y_n)[\bar{f}^{-1}]_{im}, \quad (18)$$

$$\mathbb{G}_{nm} = (g_j(x_n, y_n) - \bar{f}_i(x_n, y_n)[\bar{f}^{-1}]_{ik}g_{kj})[h^{-1}]_{jm} \quad (19)$$

The method can be easily extended to the solution of the Helmholtz equation

$$-\Delta u(x, y) - \lambda^2 u(x, y) = \gamma(x, y) \quad (20)$$

For the homogeneous case (i.e. $\gamma(x, y) = 0$), $\sigma(x, y) = \lambda^2 u(x, y)$, i.e. $\Sigma = \lambda^2 U$ in equation (15), and we can write:

$$B = (\mathbb{F} - \lambda^2 \mathbb{G})U \Rightarrow U = (\mathbb{F} - \lambda^2 \mathbb{G})^{-1} B. \quad (21)$$

For the forced case, $\sigma(x, y) = \lambda^2 u(x, y) + \gamma(x, y)$, that is $\Sigma = \lambda^2 U + \Gamma$, and we obtain:

$$B = (\mathbb{F} - \lambda^2 \mathbb{G})U - \mathbb{G}\Gamma \Rightarrow U = (\mathbb{F} - \lambda^2 \mathbb{G})^{-1}(B + \mathbb{G}\Gamma). \quad (22)$$

It is worth to note that the matrix of the global linear system (16) or (21), i.e. \mathbb{F} for the Poisson BVP and $\mathbb{F} - \lambda^2 \mathbb{G}$ for the Helmholtz BVP, is a sparse matrix with at most 9 non-zero elements in each row. Then, a suitable and efficient algorithm can be applied which ensures a computational effort proportional to the number of grid points. In the proposed solver, the UMFPACK suite, using a column pre-ordering [13] algorithm, proved its efficiency, giving a computational time which increases slightly super-linearly as is to be expected for the direct solution of a 2D Laplacian [14].

4. Test cases

In order to show the accuracy and efficiency of the numerical solver proposed, 2D elliptic boundary value problems for which an analytical solution is available are considered in the following. Most of them are strictly related to physical problem, such as: Green–Taylor vortex, Lamb–Oseen vortex, Wave Front. Just one, i.e. the boundary line singularity, is not immediately related to a physical problem, but it has been considered to stress the method when a strong singularity occurs on the forcing term. Finally, two cases for the homogeneous and forced Helmholtz equation, i.e. MacCamy–Fuchs and Schrödinger equation respectively, are discussed. In all the cases, Dirichlet BVP is solved. However, for the Lamb–Oseen vortex, the corresponding Neumann BVP is also proposed.

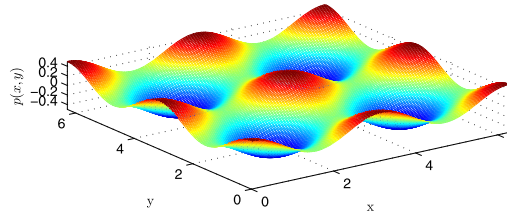


Fig. 3. Green–Taylor vortex field: solution of the pressure field at $t = 10^{-4}$ s, and $\nu = 1 \text{ m}^2/\text{s}$.

The accuracy of the method is quantified in terms of the L_2 and L_∞ error, defined as

$$Err_{L_2} = \frac{\|u^{num} - u^{an}\|_2}{\|u^{an}\|_2}$$

$$Err_{L_\infty} = \frac{\|u^{num} - u^{an}\|_\infty}{\|u^{an}\|_\infty}$$

respectively. In both definitions u^{num} and u^{an} are the numerical and analytical solutions, respectively. The theoretical accuracy of the method depends on the order of the harmonic polynomial functions used in the interpolation formula (6) and on the order of the interpolation function used to approximate the forcing term $\sigma(x, y)$ in (7). Because for both of them a fourth-order accuracy of the interpolation functions is used, it is expected that the error should decrease as a fourth power of the grid size dx . A reference value 4 of the chosen error norm is used in the following convergence studies. In case of nonuniform grid or when a polar grid is used, a measure of the grid size is estimated as

$$ds = \sqrt{\frac{XY}{N_x N_y}}, \tag{23}$$

with X and Y representing length and width of the computational domain (in case of a polar grid $X = R$ and $Y = R\Theta$), while N_x and N_y is the number of points along X and Y , respectively.

4.1. Green–Taylor vortex

The Green–Taylor Vortex is an unsteady flow of a periodic decaying vortex system, governed by the Navier–Stokes equation, for which an analytical solution of the velocity field is:

$$u(x, y, t) = \sin(x) \cos(y) e^{-2\nu t}, \quad v(x, y, t) = -\cos(x) \sin(y) e^{-2\nu t}$$

where ν indicates the kinematic viscosity of the fluid and with the pressure field (see Fig. 3 at $t = 10^{-4}$) given by:

$$p(x, y, t) = \frac{\rho}{4} (\cos(2x) + \cos(2y)) (e^{-2\nu t})^2$$

with ρ the fluid density. In particular, in the fluid domain $\Omega = [0, 2\pi] \times [0, 2\pi]$, the pressure field $p(x, y) = p(x, y, t_p)$ at a prescribed time instant $t = t_p$ satisfies the Poisson problem

$$\Delta p(x, y) = -2\rho (v_x(x, y) u_y(x, y) - u_x(x, y) v_y(x, y)) \tag{24}$$

with proper conditions at the domain boundaries. Because the aim of the proposed numerical method is the solution of the Poisson equation, the BVP ((24) + Boundary Conditions) has been first solved by assuming the RHS of equation (24) to be known at the prescribed time $t_p = 10^{-4}$. In order to assess the features of the method for different boundary conditions, two different sets of boundary conditions have been imposed to the squared domain Ω :

(a) Dirichlet BC

$$p(0, y) = p(2\pi, y) = \frac{\rho}{4} (1 + \cos(2y)) (e^{-2\nu t_p})^2$$

$$p(x, 0) = p(x, 2\pi) = \frac{\rho}{4} (1 + \cos(2x)) (e^{-2\nu t_p})^2$$

(b) Neumann BC

$$\frac{\partial p}{\partial x}(0, y) = \frac{\partial p}{\partial x}(2\pi, y) = \frac{\rho}{4} \cos(2y) (e^{-2\nu t_p})^2$$

$$\frac{\partial p}{\partial y}(x, 0) = \frac{\partial p}{\partial y}(x, 2\pi) = \frac{\rho}{4} \cos(2x) (e^{-2\nu t_p})^2$$

Table 2

Convergence study for the Green–Taylor vortex case: grid parameters and order of convergence according to Err_{L_2} and Err_{L_∞} norms.

grid #	N_x	N_y	Order of convergence			
			Dirichlet BVP		Neumann BVP	
			Err_{L_2}	Err_{L_∞}	Err_{L_2}	Err_{L_∞}
1st	51	51	4.0386	4.0593	6.0274	5.5302
2nd	101	101	4.0213	4.0313	5.8450	5.5385
3rd	151	151	4.0149	4.0235	5.0866	5.2163
4th	201	201	4.0091	4.0145	3.4301	3.5532
5th	401	401	4.0034	4.0065	3.6530	3.7769
6th	801	801				
Mean value			4.0175	4.0270	4.8084	4.7230
Global value			4.0179	4.0276	4.7041	4.6152

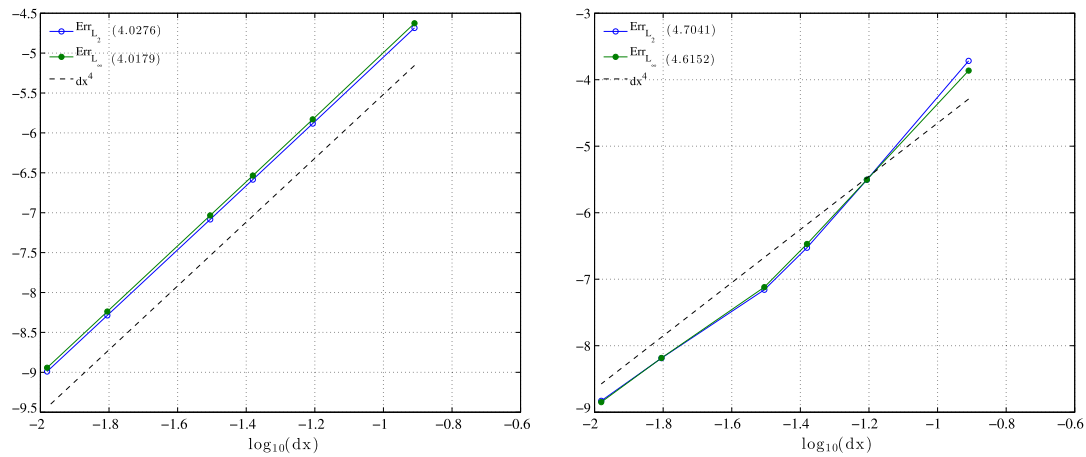


Fig. 4. Convergence of the pressure field at $t = 10^{-4}$ s, and $\nu = 1 \text{ s}^{-1}$, for the Dirichlet (left) and Neumann (right) BVP.

As a consequence, Poisson equation (24) has been solved numerically with Dirichlet (a) or Neumann (b) conditions at the boundary of the domain. A convergence study has been performed by considering six grids, whose number of points is reported in Table 2, with the associated local order of convergence for both the case (a) (Dirichlet BVP) and (b) (Neumann BVP) and for both the norm- L_2 and $-L_\infty$ error related to each couple of grids. Last two rows show the mean value and the best fitting (i.e. global value) of the local order of convergence, respectively. The log–log plot of the error L_2 and L_∞ is shown in the left (i.e. Dirichlet BVP) and right (Neumann BVP) panel of Fig. 4, together with the theoretical trend associated with fourth order accuracy of the used scheme (dashed line). A convergence rate close to 4 for the Dirichlet BVP and slightly higher for the Neumann one, confirms the theoretical value of the present algorithm.

Fig. 5 shows the log–log diagram of the CPU time as function of the number $N = N_x N_y$ of grid points, both for the Dirichlet (left panel) and Neumann (right panel) BVP. The computational time necessary for the inversion of the matrix (blue line) and for determining the global solution (green line) is reported together with the theoretical trends $N^{3/2}$ and N . It is evident how the generalized HPC method shows a CPU time which increases with the number of the grid points closer to the N -trend than to the $N^{3/2}$, assessing the efficiency of the proposed approach.

4.2. Lamb–Oseen vortex

The Lamb–Oseen Vortex [15] displays a solution of the vorticity equation in 2D, i.e. the vortex-stretching term is zero, and, due to the axisymmetry of the solution, the nonlinear advective term vanishes as well. Hence, the governing equation is:

$$\frac{\partial \omega(x, y, t)}{\partial t} = \nu \Delta \omega(x, y, t) \quad (25)$$

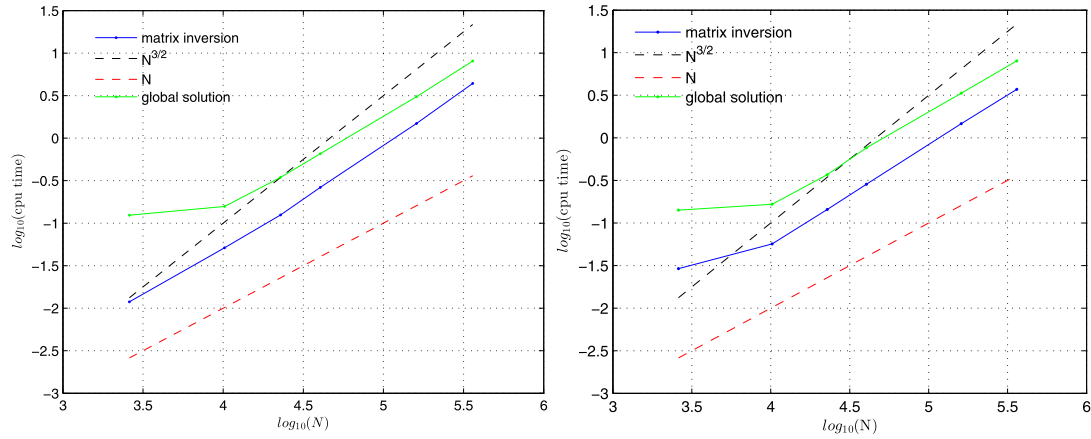


Fig. 5. Convergence analysis of the CPU time for the Dirichlet (left) and Neumann (right) BVP. (For interpretation of the references to color in this figure, the reader is referred to the web version of this article.)

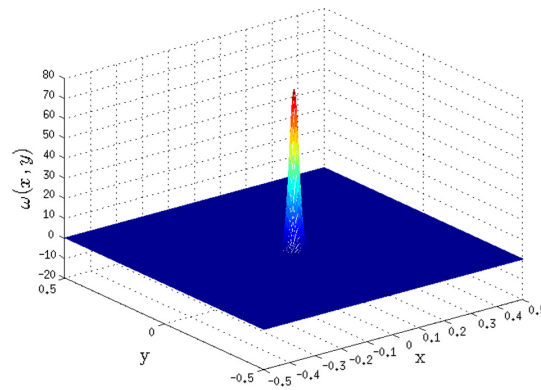


Fig. 6. Lamb–Oseen vortex: solution $\omega(x, t)$ at $t = 10^{-4}$ s for $\nu = 1 \text{ m}^2/\text{s}$.

with $\vec{\omega} = \nabla \times \vec{v} = (0, 0, \omega)$ which represents the vorticity vector. The effect of the Laplacian operator consists in diffusing the vorticity in the field at a rate proportional to the viscosity ν . Let

$$\omega(x, y, t = 0) = \Gamma_0 \delta(x) \delta(y) \tag{26}$$

be the initial condition, that is we consider a point vortex with initial circulation Γ_0 (where $\delta(f)$ is the Dirac function), the exact solution is the Lamb–Oseen vortex:

$$\omega(x, y, t) = \frac{\Gamma_0}{4\nu\pi t} e^{-r^2/4\nu t},$$

where the vorticity field is a purely radial function depending only on $r = \sqrt{x^2 + y^2}$. The solution of the velocity field leads to a purely tangential velocity field v_τ ,

$$v_\tau = \frac{\Gamma_0}{2\pi r} (1 - e^{-r^2/4\nu t}),$$

i.e. the radial velocity is zero. The following Poisson BVP has been solved numerically:

$$\Delta \omega(x, y, t) = \frac{\partial \omega(x, y, t = t_p)}{\partial t}$$

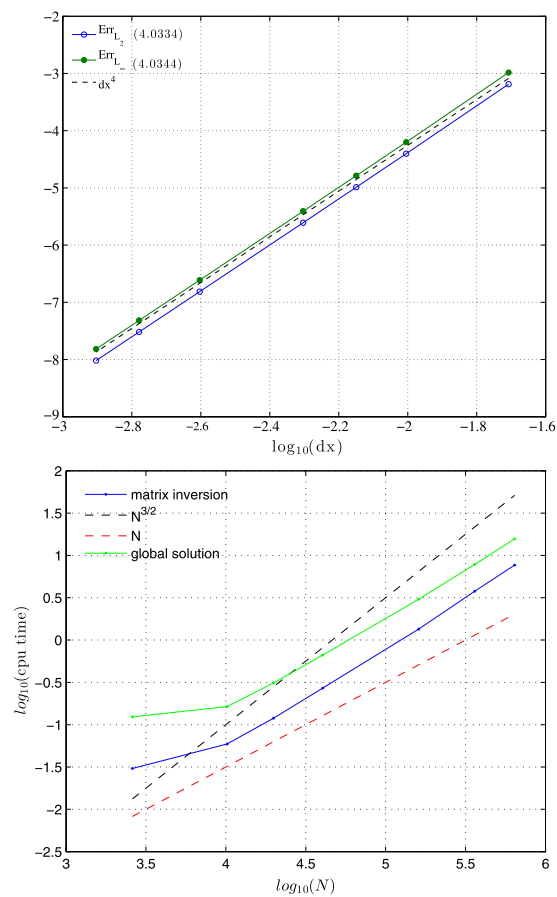
with Dirichlet conditions at the boundary of the domain, by assuming the term $\partial \omega(x, y, t) / \partial t$ to be known at the prescribed time $t_p = 10^{-4}$ s. A regular Cartesian grid on a square domain has been considered. The analytical solution calculated at $t = 10^{-4}$ s is reported in Fig. 6.

A convergence study has been performed by considering seven grids, whose number of points is reported in Table 3, together with the associated order of convergence for both the norm- L_2 and $-L_\infty$ error. The log–log plot of the errors L_2

Table 3

Convergence study for the Lamb–Oseen vortex case: grid parameters and order of convergence.

grid #	N_x	N_y	Order of convergence	
			Err_{L_2}	Err_{max}
1st	51	51	4.0926	4.0966
2nd	101	101	4.0437	4.0449
3rd	141	141	4.0285	4.0291
4th	201	201	4.0165	4.0168
5th	401	401	4.0089	4.0089
6th	601	601	4.0061	4.0064
7th	801	801		
Mean value			4.0332	4.0343
Global value			4.0334	4.0344

**Fig. 7.** Lamb–Oseen vortex: convergence of the solution (top) and of the CPU Time (bottom) at $t = 10^{-4}$ s for $\nu = 1 \text{ m}^2/\text{s}$.

and L_∞ is shown in the top panel of Fig. 7, together with the theoretical trend associated with dx^4 (dashed line). The bottom panel of Fig. 7 shows the convergence of the computational cost of the proposed method.

A convergence rate of the solution close to 4 and a convergence rate of the CPU time proportional to the number of the grid points confirms the efficiency of the algorithm.

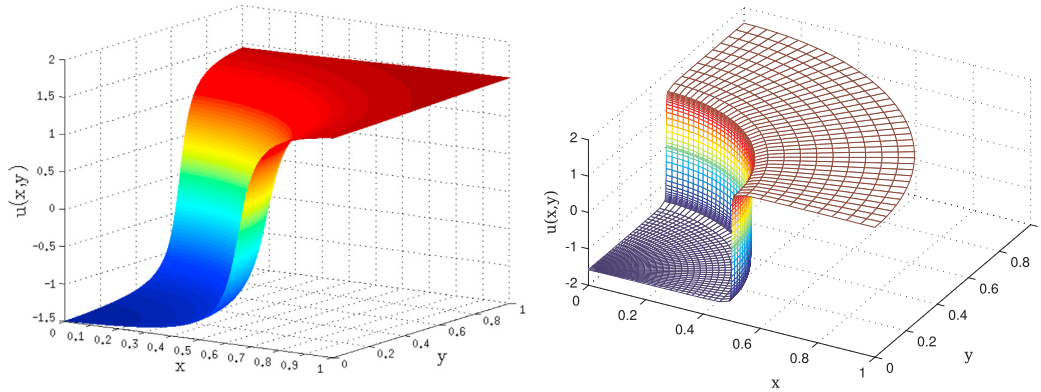


Fig. 8. Analytical solution for the wave front with $(x_c, y_c) = (-0.05, -0.05)$, $r_0 = 0.7$. Left: $\alpha = 20$ (mild wave front). Right: $\alpha = 10^3$ (steep wave front).

Table 4
Convergence study for the mild wave front case: grid parameters, local and global order of convergence.

grid #	N_x	N_y	Order of convergence	
			Err_{L_2}	Err_{L_∞}
1st	51	51	4.1136	4.1732
2nd	101	101	4.0467	4.0664
3rd	151	141	4.0278	4.0208
4th	201	201	4.0148	4.0166
5th	401	401	4.0073	4.0104
6th	601	601	4.0046	4.0060
7th	801	801		
Mean value			4.0358	4.0489
Global value			4.0366	4.0502

4.3. Wave front

The previous cases represent two classical analytical solutions of the Navier–Stokes equation well reproduced numerically by using a uniform Cartesian grid. In order to test a refinement algorithm for the solution of the Poisson problem, a steep wave front in the interior of the fluid domain is considered in the following. A circular wave front, whose analytical form is:

$$u(x, y) = \arctan(\alpha(r - r_0)), \quad \text{with } r = \sqrt{(x - x_c)^2 + (y - y_c)^2}$$

is the solution of the Poisson problem

$$\Delta u(x, y) = \sigma(x, y; \alpha) \tag{27}$$

for $u(x, y)$ with Dirichlet boundary conditions. In eq. (27), the forcing term $\sigma(x, y; \alpha)$ is prescribed once α is assigned [16]. Parameter α gives the steepness of the circular wave front, (x_c, y_c) is the center of the wave front and r_0 is the distance between the wave front and its center.

For the case considered in Fig. 8 the center of the wave front is outside the domain. The solutions are characterized by a mild (i.e. $\alpha = 20$, see left panel of Fig. 8) and steep (i.e. $\alpha = 10^3$, see right panel of Fig. 8) wave front. The mild problem is solved on a regular Cartesian grid. The convergence study (see left panel of Fig. 9) has been done by using seven grids, whose number of nodes along x (N_x) and y (N_y) direction are reported in Table 4, together with the local order of convergence relative to the norm- L_2 and $-L_\infty$ error. Last two rows report the mean and the global value (which is the best fitting coefficient of the log–log error curve) of the L_2 and L_∞ error. The corresponding CPU time necessary for the inversion of the matrix and the determination of the global solution is shown in the right panel of Fig. 9.

The steep wave front case (whose analytical solution is shown in the right panel of Fig. 8) is numerically solved by using a stretched polar grid whose radial spacing is constant in the region with a flat solution while it changes as a linear function (see right panel of Fig. 11) across the “jump”. The forcing term $\sigma(x, y; \alpha = 10^3)$, according to [16], is shown in the left panel of Fig. 11. In particular the grid has been built as:

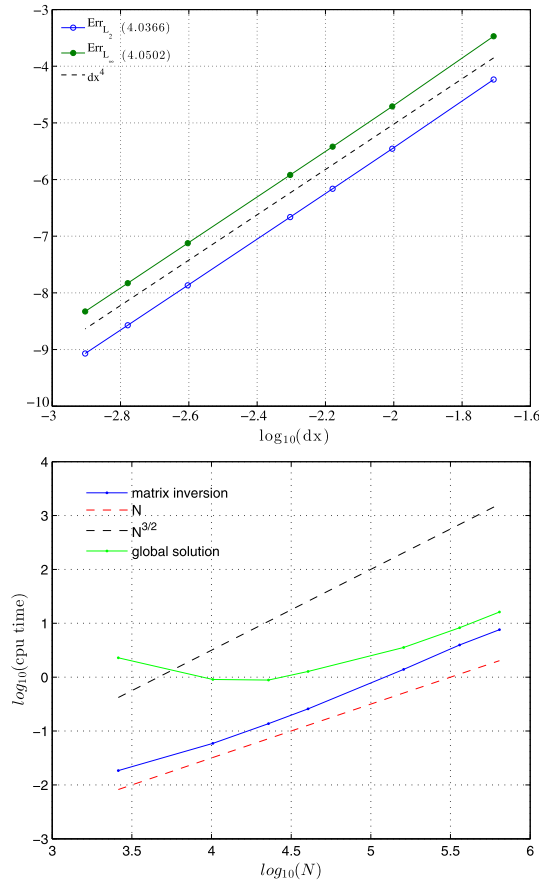


Fig. 9. Convergence analysis for the mild wave front case $\alpha = 20$ with $(x_c, y_c) = (-0.05, -0.05)$, $r_0 = 0.7$. Top: error L_2 and L_∞ . Bottom: CPU time.

$$r(n) = \begin{cases} dr_{min}n, & n = 1, \dots, N_1 \text{ and } r < r_0 - \epsilon \\ e_1n^2 + e_2n + e_3, & n = 1, \dots, N_\epsilon/2 + 1 \text{ and } r_0 - \epsilon \leq r \leq r_0 \\ e_4n^2 + e_5n + e_6, & n = 1, \dots, N_\epsilon/2 \text{ and } r_0 \leq r \leq r_0 + \epsilon \\ (r_0 + \epsilon) + dr_{max}n, & n = 1, \dots, N_2 \text{ and } r > r_0 + \epsilon \end{cases}$$

with the coefficients e_i ($i = 1, \dots, 6$) which are determined by imposing the derivative of the function and the value of the distance r in prescribed points of the domain. Here, ϵ represents a small distance (approximately equal to 10^{-12}) around the wave front. According to the previous definitions, $N_r = N_1 + N_\epsilon + N_2 + 1$, while N_θ represents the nodes number in the azimuthal direction. The grid parameters for the convergence study shown in the left panel of Fig. 10 have been fixed according to Table 5, where the local order of convergence for the norm L_2 and L_∞ error is also given as a function of the grid spacing ds defined in eq. (23). The corresponding computational time necessary for the inversion of the sparse matrix and for the evaluation of the solution is reported in the right panel of Fig. 10, that confirms a trend of the CPU time variable between N and $N^{3/2}$.

4.4. Boundary line singularity

In order to test the capability of the proposed numerical model to deal with a singular behavior of the forcing term, the boundary line singularity [16] is faced. This is the solution of the following Poisson problem:

$$\Delta u(x, y) = -(\pi/2)^2 \cos(\pi/2y) + \alpha(\alpha - 1)x^{\alpha-2}$$

with Dirichlet boundary conditions. The solution

$$u(x, y) = \cos(\pi/2y) + x^\alpha.$$

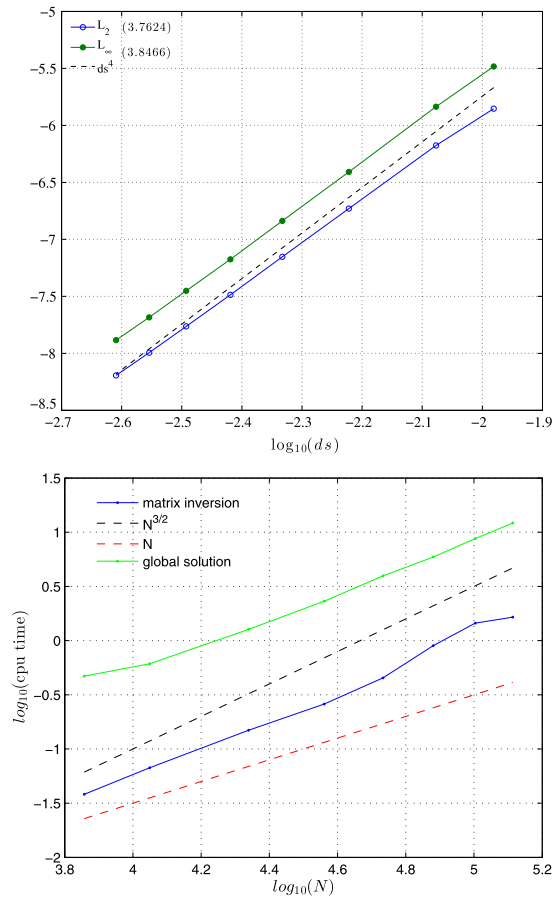


Fig. 10. Convergence analysis for the steep wave front case $\alpha = 10^3$ with $(x_c, y_c) = (-0.05, -0.05)$, $r_0 = 0.7$. Top: error L_2 and L_∞ . Bottom: CPU time.

Table 5

Convergence study for the steep wave front case: grid parameters, local and global order of convergence.

grid #	dr_{min}	dr_{max}	N_1	N_ϵ	N_2	N_r	N_θ	Order of convergence	
								Err_{L_2}	Err_{L_∞}
1st	0.0977	0.100	6	78	5	90	80	3.3671	3.6763
2nd	0.0782	0.080	7	98	6	112	100	3.8169	3.9475
3rd	0.0559	0.057	9	138	8	156	140	3.8222	3.8747
4th	0.0434	0.044	12	178	11	202	180	3.8602	3.9088
5th	0.0355	0.036	14	218	13	246	220	3.7657	3.7615
6th	0.0301	0.031	17	258	16	292	260	3.7452	3.7797
7th	0.0261	0.027	19	298	18	336	300	3.6278	3.6281
8th	0.0230	0.024	22	338	21	382	340		
Mean value								3.7150	3.7967
Global value								3.7624	3.8466

is shown in Fig. 12 (for $\alpha = 1.1$). The parameter α determines the strength of the singularity line which characterizes the forcing term: $\alpha < 2$ implies a strong singularity and the solution lies in $H^{\alpha+1/2-\epsilon}$, $\forall \epsilon > 0$, with H^m the Sobolev space of functions whose derivatives of order m are square integrable [16].

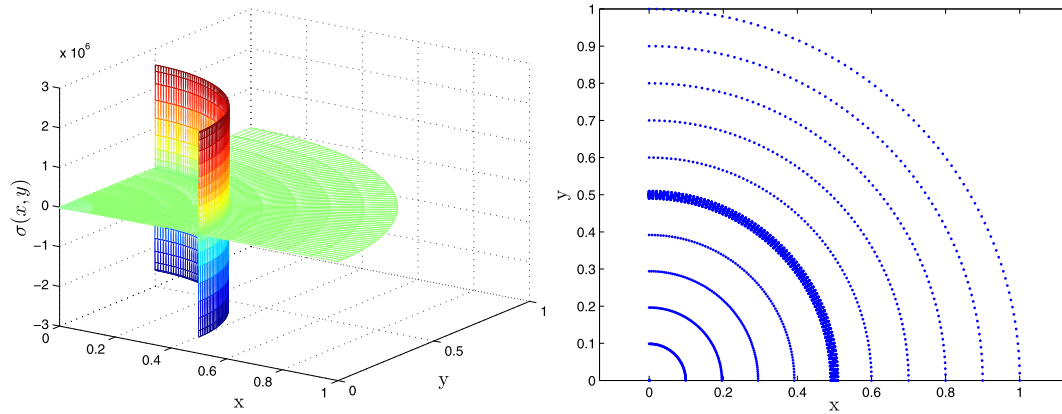


Fig. 11. Forcing $\sigma(x, y)$ and stretched polar mesh used for the steep wave front.

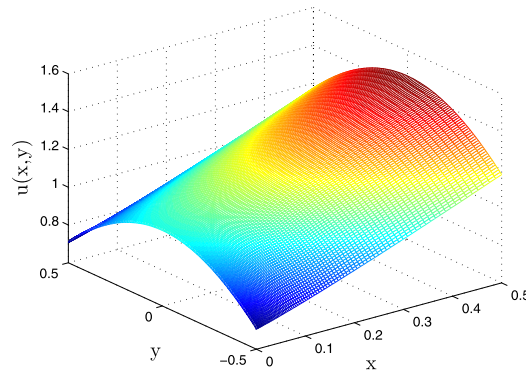


Fig. 12. Computed solution of the boundary line singularity equation with $\alpha = 1.1$.

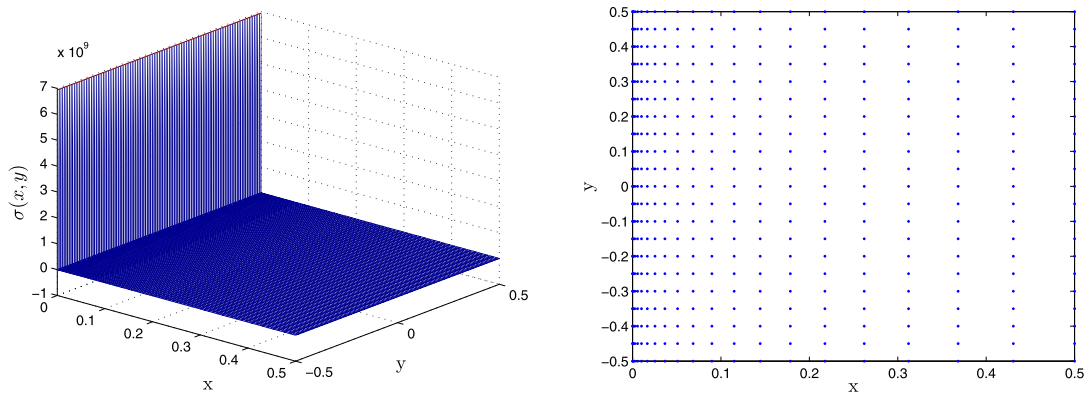


Fig. 13. Forcing function (left) and stretched Cartesian mesh (right) used for the boundary line singularity case.

The problem, with $\alpha = 1.1$, is solved in $\Omega = (\epsilon, 0.5) \times (-0.5, 0.5)$ (with $\epsilon = 10^{-12}$) by using a Cartesian grid which is stretched along the x direction, i.e. across the singularity (see right panel of Fig. 13). In contrast, the spacing along the y -direction is kept constant. Left panel of Fig. 13 shows the forcing term.

More in details, the coordinate x of each grid node varies as a cubic function:

$$e_1 n^3 + e_2 n^2 + e_3 n + e_4, n = 1, \dots, N_x \quad (28)$$

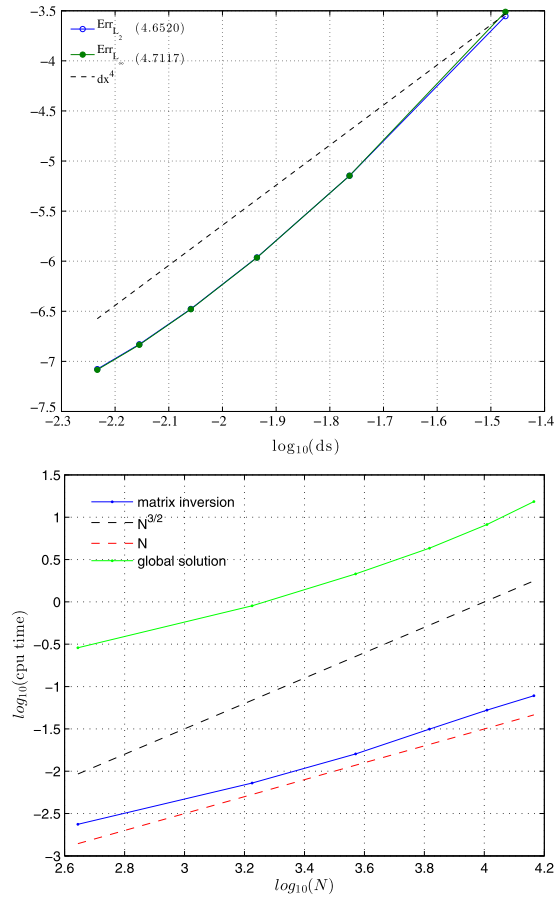


Fig. 14. Convergence analysis for the boundary line singularity case ($\alpha = 1.1$). Top: error L_2 and L_∞ . Bottom: CPU time.

Table 6
Convergence study for the boundary line singularity case: grid parameters, local and global order of convergence.

grid #	N_x	N_y	Order of convergence	
			Err_{L_2}	Err_{L_∞}
1st	21	21	5.4830	5.6294
2nd	41	41	4.7288	4.7419
3rd	61	61	4.1703	4.1834
4th	81	81	3.6812	3.7010
5th	101	101	3.1634	3.1835
6th	121	121		
Mean value			4.2454	4.2878
Global value			4.6520	4.7117

where the e_i ($i = 1, \dots, 4$) coefficients have been determined by imposing the value of the coordinate x and the relative derivative in prescribed points of the domain. A convergence study has been performed in Fig. 14 by considering six grids, whose number of nodes and the local and global order of convergence relative to the norm L_2 and L_∞ error are reported in Table 6. Top panel of Fig. 14 shows the convergence analysis through the log–log plot of the error L_2 and L_∞ together with the theoretical trend associated with dx^4 (dashed line). A 4th order convergence rate can be appreciated also in this case. However, a decreasing local order of convergence is observed by increasing the number of nodes; it is related with

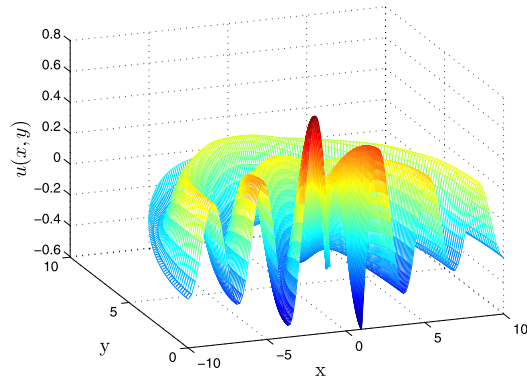


Fig. 15. Computed solution of the MacCamy–Fuchs equation.

Table 7

Convergence study for the MacCamy–Fuchs problem: grid parameters, local and global order of convergence.

grid #	N_r	N_θ	Order of convergence	
			Err_{L_2}	Err_{L_∞}
1st	100	100	3.6595	3.6466
2nd	200	200	3.9806	3.9780
3rd	300	300	4.0061	4.0106
4th	400	400	4.0088	4.0128
5th	500	500		
Mean value			3.9137	3.9120
Global value			3.8563	3.8515

the singularity of the forcing term. Also the CPU time, shown in the bottom panel of Fig. 14, confirms the efficiency of the model proposed.

4.5. Helmholtz equation

4.5.1. Homogeneous case: MacCamy–Fuchs equation

In hydrodynamics, the homogeneous Helmholtz equation

$$\Delta u(x, y) + k^2 u(x, y) = 0$$

describes the steady-state scattering problem of a plane wave system with wavenumber k advancing from the negative axis, which is incident to a circular cylinder of radius a with infinite draught [17]. The solution, representing the scattered wave in a polar domain (r, θ) (see Fig. 15) is:

$$u(r, \theta) = J_0(kr) - \frac{J_0'(ka)}{H_0^{(2)'}(ka)} H_0^{(2)}(kr) + 2 \sum_{m=1}^{\infty} i^m [J_m(kr) - \frac{J_m'(ka)}{H_m^{(2)'}(ka)} H_m^{(2)}(kr)] \cos(m\theta) - e^{ikx}$$

where $H_m^{(2)}(\cdot)$ is the Hankel function of the second type and $J_m(\cdot)$ is the Bessel function of the first kind. The solution assumes the time dependence $e^{i\omega t}$.

The problem has been solved numerically on a polar domain (r, θ) with outer radius $R = 10$, cylinder radius $a = 1$ and by considering an incident wave with wavenumber $k = 2$.

The convergence analysis has been performed on five grids, whose number of points are indicated in Table 7, together with the local order of convergence relative to the error in norm L_2 and L_∞ . Mean and global value of error are also reported in the last two rows of the table. Top panel of Fig. 16 shows the convergence analysis for the errors L_2 and L_∞ , together with the theoretical trend associated with dx^4 (dashed line), confirming the 4th order convergence of the generalized HPC. Bottom panel in the same figure shows the CPU time necessary for the inversion of the sparse matrix and for the evaluation of the solution and confirms the required efficiency of the proposed model.

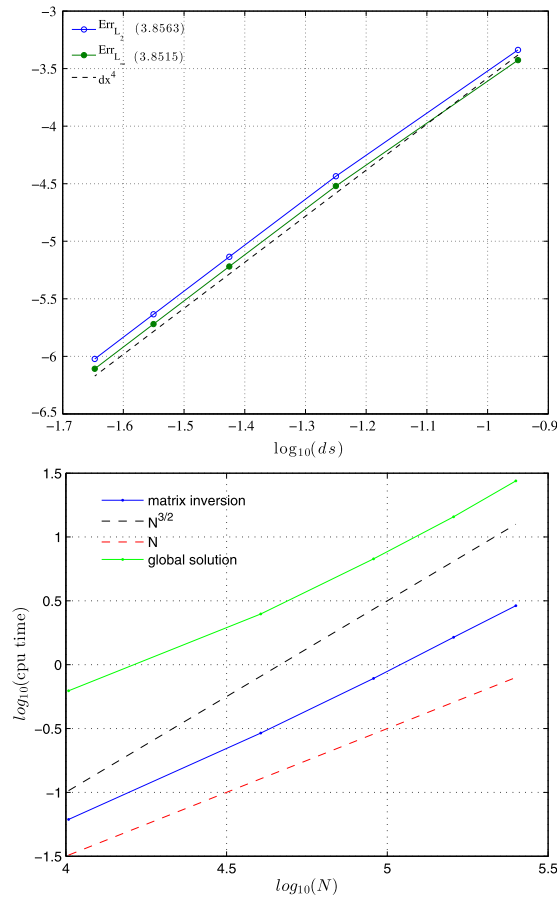


Fig. 16. Convergence analysis for the MacCamy and Fuchs problem. Top: errors L_2 and L_∞ . Bottom: CPU time.

4.5.2. Forced Helmholtz problem: Schrödinger equation

The forced Helmholtz problem is inspired by the wave function that satisfies the Schrödinger equation model of two interacting atoms:

$$\Delta u(x, y) + \frac{1}{(\alpha + r)^4} u(x, y) = -\sigma(x, y)$$

with

$$\sigma(x, y) = \frac{(-r^2 + \alpha^2) \cos(\frac{1}{\alpha+r})}{r(\alpha + r)^4} + \frac{2 \sin(\frac{1}{\alpha+r})}{(\alpha + r)^4}$$

which represents the forcing term (see Fig. 17). The solution:

$$u(x, y) = \sin\left(\frac{1}{\alpha + r}\right), \quad \text{with} \quad r = \sqrt{x^2 + y^2}$$

is highly oscillatory near the origin and it represents a wave with wavelength decreasing from infinity to zero when approaching the origin. The parameter α is related to the number of oscillations N in the whole domain, through the relation $\alpha = 1/(N\pi)$. Because of the behavior of the solution (see Fig. 18), the problem has been solved near the origin on a polar domain $\Omega = (\Delta r \times \Delta\theta) = [0, 1] \times [0, \pi/4]$.

The convergence analysis has been done on five grids with a quadratic stretching along the radial direction (see a zoomed view of the coarsest grid in Fig. 19). Table 8 reports the number of points along the radial and azimuthal directions for each

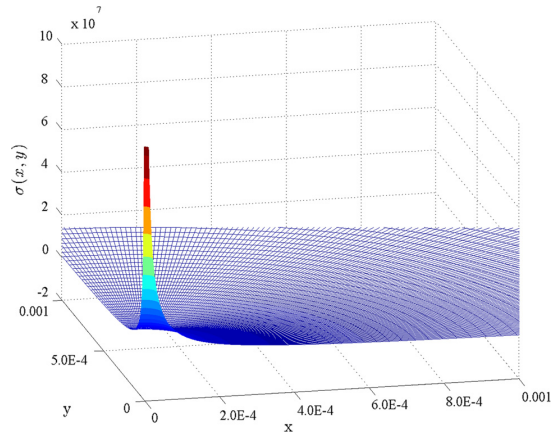


Fig. 17. Forcing term of the Schrödinger equation.

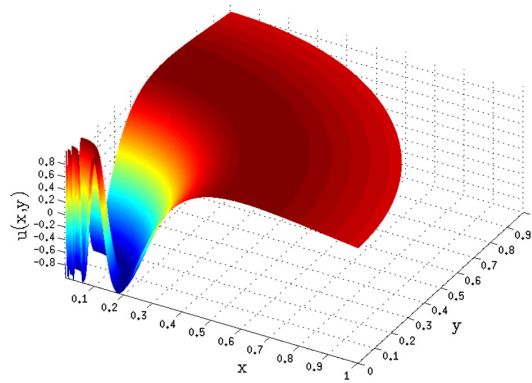


Fig. 18. Solution of the Schrödinger equation.

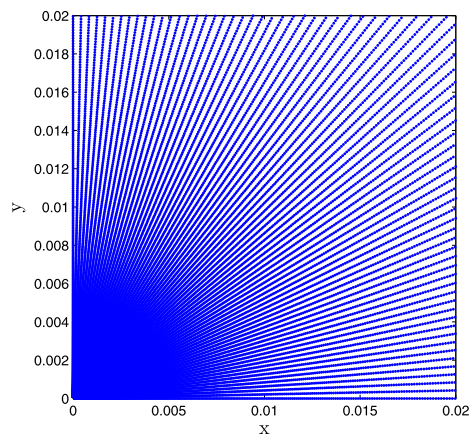


Fig. 19. Zoom of the mesh #1 used for the Schrödinger equation.

Table 8
Convergence study for the Schrödinger equation: grid parameters, local and global order of convergence.

grid #	N_r	N_θ	Order of convergence	
			Err_{L_2}	Err_{L_∞}
1st	700	71	4.0035	4.0202
2nd	900	91	4.0615	4.0174
3rd	1100	111	4.0813	4.2582
4th	1300	131	4.1095	4.0179
5th	1500	151		
Mean value			4.0639	4.0784
Global value			4.0563	4.0791

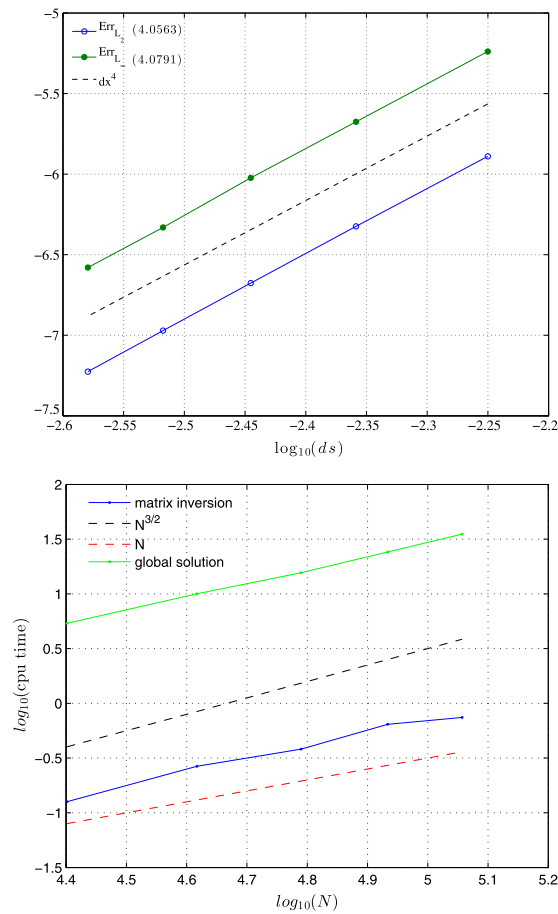


Fig. 20. Schrödinger equation: convergence rate for the error (top) and for the CPU time (bottom).

grid, as well as the local and global order of convergence for the L_2 and L_∞ error. According to the equation (23), the order of convergence has been expressed as a function of the grid size ds . Top panel of Fig. 20 shows that the local and global error goes as the theoretical trend ds^4 , confirming the accuracy of the method. Similarly to the previous cases, also the CPU time varies proportional with the number of that unknowns (see bottom panel of Fig. 20).

5. Conclusions

The present paper proposes an original and 4th order accurate numerical method, the *generalized HPC method*, for the solution of the Boundary Value Problem for the Poisson equation. It is based on the decomposition of the global problem as the superposition of the homogeneous BVP, i.e. that for the Laplace equation, and a particular solution of the corresponding inhomogeneous problem on an unbounded domain. In the former, the solution is approximated through the harmonic polynomial functions [1]. In the latter, in order to keep the same order of accuracy as the solution, the forcing term has been approximated through a bi-quadratic interpolation. The method has been validated for several test cases for which an analytical solution is available, confirming the 4th order accuracy even in the case where a singular solution is expected, or a singular behavior of the forcing term is achieved. The method is promising to be used within incompressible Navier–Stokes solver where a high accuracy with small computational time in the solution of the Poisson equation is still a challenge. In particular, the main advantages of the proposed algorithm consist in the high accuracy and high efficiency both in terms of computational effort and easy to be implemented. These features, together with the availability of a closed form of the solution within each stencil, make feasible coupling the generalized HPC method with other numerical algorithms within a domain-decomposition strategy or within an adaptive mesh refinement technique. The ongoing research development of the present research group is addressed just in this direction, as well as on the extension of the method to the 3D case.

Acknowledgements

This research activity has been partially supported by Centre for Autonomous Marine Operations and Systems (AMOS), NTNU, Trondheim (project number 223254). It has been also partially supported by the Flagship Project RITMARE – The Italian Research for the Sea – coordinated by the Italian National Research Council and funded by the Italian Ministry of Education, University and Research within the National Research Program 2011–2013.

References

- [1] Y.-L. Shao, O.M. Faltinsen, A harmonic polynomial cell (HPC) method for 3D Laplace equation with application in marine hydrodynamics, *J. Comput. Phys.* 274 (2014) 312–332, <http://dx.doi.org/10.1016/j.jcp.2014.06.021>.
- [2] L.C. Evans, *Partial Differential Equations*, *Grad. Stud. Math.*, vol. 19, American Mathematical Society, 1998.
- [3] A.J. Chorin, Numerical solution of the Navier–Stokes equations, *Math. Comput.* 22 (1968) 745–762, <http://dx.doi.org/10.1090/s0025-5718-1968-0242392-2>.
- [4] R. Vanselow, Relations between FEM and FVM applied to the Poisson equation, *Computing* 57 (1996) 93–104, <http://dx.doi.org/10.1007/BF02276874>.
- [5] J.H. Ferziger, M. Peric, *Computational Methods for Fluid Dynamics*, 3rd edition, Springer, 2002.
- [6] J. Demmel, Sources of parallelism and locality in simulation, CS267: Lecture 13, Feb 27, 1996, <http://www.cs.berkeley.edu/~demmel/cs267/lecture17/lecture17.html>.
- [7] Y.-L. Shao, O.M. Faltinsen, Towards efficient fully-nonlinear potential-flow solvers in marine hydrodynamics, in: *ASME 2012-31st International Conference on Ocean, Offshore and Arctic Engineering*, ASME, 2012, pp. 369–380.
- [8] R. Hiptmair, A. Muiola, I. Perugia, C. Schwab, Approximation by harmonic polynomials in star-shaped domains and exponential convergence of Trefftz hp-DGFEM, *Tech. Rep.* 2012-38, Seminar fuer Angewandte Mathematik, Eidgenoessische Technische Hochschule, CH-8092 Zuerich, Switzerland, 2012.
- [9] I.N. Vekua, On completeness of a system of harmonic polynomials in space, *Dokl. Akad. Nauk SSSR* 90 (1953) 495–498.
- [10] I.N. Vekua, *New Methods for Solving Elliptic Equations*, Interscience Publishers John Wiley & Sons, Inc., New York, USA, 1967.
- [11] H. Liang, O.M. Faltinsen, Y.-L. Shao, Application of a 2D harmonic polynomial cell (HPC) method to singular flows and lifting problems, *Applied Ocean Research* under Review.
- [12] O. Faltinsen, A. Timokha, Analytically approximate natural sloshing modes and frequencies in two-dimensional tanks, *Eur. J. Mech. B, Fluids* 47 (2014) 176–187, <http://dx.doi.org/10.1016/j.euromechflu.2014.01.005>, <http://www.sciencedirect.com/science/article/pii/S0997754614000077>.
- [13] T.A. Davis, Algorithm 832: UMFPACK V4.3—an unsymmetric-pattern multifrontal method, *ACM Trans. Math. Software* 30 (2004) 196–199, <http://dx.doi.org/10.1145/992200.992206>.
- [14] H. Bingham, H. Zhang, On the accuracy of finite difference solutions for nonlinear water waves, *J. Eng. Math.* 58 (2007) 211–228.
- [15] G.K. Batchelor, Axial flow in trailing line vortices, *J. Fluid Mech.* 20 (1964) 645–658, <http://dx.doi.org/10.1017/S0022112064001446>.
- [16] W.F. Mitchell, A collection of 2D elliptic problems for testing adaptive algorithms, *Tech. Rep.*, Mathematical and Computational Sciences Division, National Institute of Standards and Technology, Gaithersburg, MD 20899-8910, USA, February 2010.
- [17] R.C. MacCamy, R.A. Fuchs, Wave forces on piles: a diffraction theory, *Tech. Rep. memorandum*, No. 69, US Army, Corps of Engineers, Beach Erosion Board, Washington DC, USA, December 1954.

Bibliography

- [1] ABRAHAMSEN, B. C. *Sloshing induced tank-roof impact with entrapped air pocket*. Ph.D. thesis, Norwegian University of Science and Technology (NTNU) (2011).
- [2] ABRAHAMSEN, B. C. AND FALTINSEN, O. M. The natural frequency of the pressure oscillations inside a water-wave entrapped air pocket on a rigid wall. *Journal of Fluids and Structures*, **35** (2012), 200.
- [3] BAGNOLD, R. A. Interim report on wave-pressure research. Tech. rep. (1939).
- [4] BARDAZZI, A., LUGNI, C., ANTUONO, M., GRAZIANI, G., AND FALTINSEN, O. M. Generalized hpc method for the poisson equation. *Journal of Computational Physics*, **299** (2015), 630.
- [5] BOUSCASSE, B., ANTUONO, M., COLAGROSSI, A., AND LUGNI, C. Numerical and experimental investigation of nonlinear shallow water sloshing. *International Journal of Nonlinear Sciences and Numerical Simulation*, **14** (2013), 123.
- [6] CHAN, E. S. AND MELVILLE, W. K. Deep-water plunging wave pressures on a vertical plane wall. **417** (1988), 95.
- [7] CHAPOT, M. K. Cs1 - new containment system for lng carriers. In *Gastech Conference* (2002).
- [8] DAVIS, T. A. Algorithm 832: Umfpack v4.3—an unsymmetric-pattern multifrontal method. *ACM Transactions on Mathematical Software (TOMS)*, **30** (2004), 196. doi:10.1145/992200.992206.
- [9] DOLD, J. W. An efficient surface-integral algorithm applied to unsteady gravity waves. *Journal of Computational Physics*, **103** (1992), 90.
- [10] DOMMERMUTH, D. G., YUE, D. K. P., LIN, W. M., RAPP, R. J., CHAN, E. S., AND MELVILLE, W. K. Deep-water plunging breakers: a comparison between potential theory and experiments. *Journal of Fluid Mechanics*, **189** (1988), 423. Available from: http://journals.cambridge.org/article_S0022112088001089, doi:10.1017/S0022112088001089.
- [11] FALTINSEN, O. M. AND TIMOKHA, A. N. *Sloshing*. Cambridge University (2010).
- [12] FENTON, J. D. *Numerical methods for nonlinear waves*, chap. 5, pp. 241–324. World scientific (2011). Available from: http://www.worldscientific.com/doi/abs/10.1142/9789812797544_0005, arXiv:http://www.worldscientific.com/doi/abs/10.1142/9789812797544_0005.

- com/doi/pdf/10.1142/9789812797544_0005, doi:10.1142/9789812797544_0005.
- [13] GRACZYK, M. *Experimental investigation of sloshing loading and load effects in membrane LNG tanks subjected to random excitation*. Ph.D. thesis, Norwegian University of Science and Technology (NTNU) (2008).
- [14] GRECO, M. *A Two-dimensional Study of Green-Water Loading*. Ph.D. thesis, Norwegian University of Science and Technology (NTNU) (2001).
- [15] GRECO, M., LANDRINI, M., AND FALTINSEN, O. Impact flows and loads on ship-deck structures. *Journal of Fluids and Structures*, **19** (2004), 251 . Available from: <http://www.sciencedirect.com/science/article/pii/S0889974604000088>, doi: <http://dx.doi.org/10.1016/j.jfluidstructs.2003.12.009>.
- [16] HULL, P. AND MÜLLER, G. An investigation of breaker heights, shapes and pressures. *Ocean Engineering*, **29** (2002), 59 . Available from: <http://www.sciencedirect.com/science/article/pii/S0029801800000755>, doi:[http://dx.doi.org/10.1016/S0029-8018\(00\)00075-5](http://dx.doi.org/10.1016/S0029-8018(00)00075-5).
- [17] KIM, H.-C. AND LEE, D.-Y. Core design issues of large lng carrier. In *Gastech Conference* (2005).
- [18] LEE, H., KIM, J. W., AND HWANG, C. Dynamic strength analysis for membrane type lng containment system due to sloshing impact load. In *RINA*, pp. 39–47 (2004).
- [19] LEE, J. M., PAIK, J. K., KIM, M. H., KIM, W. S., NOH, B. J., , AND CHOE, I. H. Dynamic strength characteristics of membrane type lng cargo containment system. In *RINA*, pp. 189–200 (2006).
- [20] LINDEMARK, T., AUSTEFJORD, H. N., SELE, H. O., URM, H. S., LEE, K. J., AND HA, T. M. Csa-2 analysis of a 216k lngc membrane carrier. In *RINA*, pp. 121–132 (2006).
- [21] LUGNI, C. *Un' indagine sull'interazione fra onde di superficie libera e strutture galleggianti*. Ph.D. thesis, Università degli studi di Roma “Sapienza” (0000).
- [22] LUGNI, C., BARDAZZI, A., FALTINSEN, O. M., AND GRAZIANI, G. Hydroelastic slamming response in the evolution of a flip-through event during shallow-liquid sloshing. *Physics of Fluids*, **26** (2014), 032108.
- [23] LUGNI, C., BROCCINI, M., AND FALTINSEN, O. M. Wave impact loads: The role of the flip-through. *Physics of Fluids*, **18** (2006), 122101. doi:10.1063/1.2399077.
- [24] LUGNI, C., MIOZZI, M., BROCCINI, M., AND FALTINSEN, O. M. Evolution of the air cavity during a depressurized wave impact. i. the kinematic flow field. *Physics of Fluids*, **22** (2010), 056101+. Available from: <http://dx.doi.org/10.1063/1.3407664>, doi:10.1063/1.3407664.
- [25] LUGNI, M., BROCCINI, M., AND FALTINSEN, O. M. Evolution of the air cavity during a depressurized wave impact. ii. the dynamic field. *Physics of Fluids*, **22** (2010), 056102+. Available from: <http://dx.doi.org/10.1063/1.3409491>, doi:10.1063/1.3409491.

- [26] MARINO, E., LUGNI, C., AND BORRI, C. A novel numerical strategy for the simulation of irregular nonlinear waves and their effects on the dynamic response of offshore wind turbines. *Computer Methods in Applied Mechanics and Engineering*, **255** (2013), 275.
- [27] NEWMAN, J. N. *Marine hydrodynamics*. MIT Press Cambridge, Mass (1977). ISBN 0262140268.
- [28] OLSEN, H. AND JOHNSEN, K. Nonlinear sloshing in rectangular tanks. a pilot study on the applicability of analytical models. Tech. Rep. 74-72-S, Vol. II, DNV - Det Norske Veritas (1975).
- [29] PASTOOR, W., ØSTVOLD, T. K., BYKLUM, E., AND VALSGÅRD, S. Sloshing load and response in lng carriers for new designs, new operations and new trades. In *Gastech* (2005).
- [30] PEREGRINE, D. H. Water-wave impact on walls. *Annual Review of Fluid Mechanics*, **35** (2003), 23. doi:10.1146/annurev.fluid.35.101101.161153.
- [31] RIENECKER, M. M. AND FENTON, J. D. A fourier approximation method for steady water waves. *Journal of Fluid Mechanics*, **104** (1981), 119. Available from: http://journals.cambridge.org/article_S0022112081002851, doi: 10.1017/S0022112081002851.
- [32] SHAO, Y.-L. AND FALTINSEN, O. M. Towards efficient fully-nonlinear potential-flow solvers in marine hydrodynamics. In *ASME 2012-31st International Conference on Ocean, Offshore and Arctic Engineering*, pp. 369–380. ASME (2012).
- [33] SHAO, Y.-L. AND FALTINSEN, O. M. Towards efficient fully-nonlinear potential-flow solvers in marine hydrodynamics. In *Proceedings of the 31st International Conference on Ocean, Offshore and Arctic Engineering (OMAE), Rio de Janeiro, Brazil*, pp. 369–380 (2012).
- [34] TOPLISS, M. E., COOKER, M. J., AND PEREGRINE, D. H. Pressure oscillations during wave impact on vertical walls. vol. 2, pp. 1639–1650. Publ by ASCE, New York, NY, United States (1992).
- [35] VERHAGEN, J. AND VAN WIJNGAARDEN, L. Non-linear oscillations of fluid in a container. *Journal of Fluid Mechanics*, **22** (1965), 737.
- [36] ZHAO, R., ROGNEBAKKE, O., AND ZHENG, X. Wave and impact loads in design of large and conventional lng ships. In *RINA*, pp. 75–85 (2004).